UNIVERSITÉ DE NICE-SOPHIA ANTIPOLIS - UFR SCIENCES

École Doctorale Sciences et Technologies de l'Information et de la Communication

T H È S E

pour obtenir le titre de

Docteur en Sciences

de l'UNIVERSITÉ de Nice-Sophia Antipolis

Spécialité: Image et Vision

présentée et soutenue par

Mauricio Antonio REYES AGUIRRE

Respiratory Motion Compensation in Emission Tomography

Thèse dirigée par

Grégoire MALANDAIN, Jacques DARCOURT

et préparée à l'INRIA Sophia Antipolis, projet Epidaure

soutenue le 6 Decembre 2005

Jury:	Rapporteurs:	Pr. Isabelle Bloch
		Pr. Irène Buvat
	Examinateurs:	Pr. Laure Blanc-Feraud
		Pr. Thierry Vieville

Originaldokument gespeichert auf dem Institutionellen Repositorium der Universität Bern (BORIS) unter http://boris.unibe.ch/61072/

Dieses Werk ist unter einer Creative Commons Namensnennung 3.0 Schweiz lizenziert.
Um die Lizenz anzusehen, gehen Sie bitte zu
http://creativecommons.org/licenses/by/3.0/ch/

Sie dürfen:

Teilen — das Material in jedwedem Format oder Medium vervielfältigen und weiterverbreiten
Bearbeiten — das Material remixen, verändern und darauf aufbauen und zwar für beliebige Zwecke, sogar kommerziell.

Der Lizenzgeber kann diese Freiheiten nicht widerrufen, solange Sie sich an die Lizenzbedingungen halten.

Unter folgenden Bedingungen:

Namensnennung — Sie müssen angemessene Urheber- und Rechteangaben machen, einen Link zur Lizenz beifügen und angeben, ob Änderungen vorgenommen wurden. Diese Angaben dürfen in jeder angemessenen Art und Weise gemacht werden, allerdings nicht so, dass der Eindruck entsteht, der Lizenzgeber unterstütze gerade Sie oder Ihre Nutzung besonders.

Keine weiteren Einschränkungen — Sie dürfen keine zusätzlichen Klauseln oder technische Verfahren einsetzen, die anderen rechtlich irgendetwas untersagen, was die Lizenz erlaubt.

Sie müssen sich nicht an diese Lizenz halten hinsichtlich solcher Teile des Materials, die gemeinfrei sind, oder soweit Ihre Nutzungshandlungen durch Ausnahmen und Schranken des Urheberrechts gedeckt sind.

Es werden keine Garantien gegeben und auch keine Gewähr geleistet. Die Lizenz verschafft Ihnen möglicherweise nicht alle Erlaubnisse, die Sie für die jeweilige Nutzung brauchen. Es können beispielsweise andere Rechte wie Persönlichkeits- und Datenschutzrechte zu beachten sein, die Ihre Nutzung des Materials entsprechend beschränken.

Eine ausführliche Fassung des Lizenzvertrags befindet sich unter
http://creativecommons.org/licenses/by/3.0/ch/legalcode.de

Acknowledgments

I'd like to thank Nicholas Ayache for giving me the possibility to do my PhD thesis in the Epidaure research team, where I had the chance to encounter people of a high human and professional qualities. I wish the very best to Epidaure and its continuation; the project Asclepios.

Many thanks to my PhD supervisor, Grégoire Malandain, for his valuable support and constant motivation. Without his help, this document wouldn't exist. To him, my best wishes of success.

I'm truly thankful to Dr. Jacques Darcourt, his tremendous support and help was more than important at the difficult moments. Thanks for all your collaboration and help. Special thanks goes to Dr. Malick Koulibaly, "grand merci" Malick for all your support and help.

Thanks to all members of my jury, Irène Buvat and Isabelle Bloch, for reading my manuscript and contributing with their valuable comments, Laure Blanc-Feraud for accepting the duty of jury's president and Thierry Vieville for being always there if I needed something, specially during the first hard months here in France. His support is greatly acknowledged for all foreign students here at the Inria institute.

I'd like to acknowledge all my current colleagues and those who already left the Epidaure project but I had the opportunity to meet. Thanks to all of you for your kindness and help during these three years, and I wish you all success and prosperity in your future projects. Special thanks goes to Rasmus Paulsen for his friendship and great advices. The very best for you Rasmus.

To all my salsa friends, thanks for your friendship and constant support and kindness during these years. For all of you a hearty thanks.

To my family, Carlos, Angelica and Pamela, the most important persons in my life, without their support I wouldn't be able to finish what three years ago I started.

Contents

List of Figures

List of Tables

Part I

Background

Chapter 1

Introduction

Nowadays, medical imaging has become an important and an indispensable diagnostic tool. The wide variety of available medical imaging modalities, presents the user with a range of possibilities allowing him/her to retrieve and complement information yielded by different modalities. For example X-ray, Computerized Tomography (CT), Magnetic Resonance Imaging (MRI) are examples of imaging modalities delivering information about the anatomy of the inner human body, while functional Magnetic Resonance imaging (fMRI), Positron Emission Tomography (PET) and Single Photon Emission Tomography (SPECT) are typical examples of imaging modalities focused on visualizing the functioning or metabolism of organs and structures.

Why so many modalities? Basically, while certain modalities share some information, others produce a specific type of information. For instance, CT and MRI brings anatomical information. In CT, bony structures will clearly appear while poor contrast exists between the different soft tissues. On the contrary, MRI may differentiates between soft tissues, but exhibits a low signal for bony structures. Medical imaging modalities like PET and SPECT are based on metabolic or functional processes of the human body. They are useful for the early diagnosis, staging and treatment of a variety of abnormalities, such as coronary artery disease, renal abnormalities, liver disease, infections,

stress fractures, blood clots in the lungs, thyroid disease, cancer, etc. The fight against cancer is a clear example of the impact that nuclear medicine has brought to society.

In PET and SPECT imaging, a radioactive compound is commonly injected into the patient's body in order to highlight the functioning or metabolism of a certain organ. Unfortunately, due to the nature of the underlying physics process, long acquisition times are required to capture enough data (order of tens of minutes), in comparison to faster imaging modalities like CT or others (order of minutes or seconds). The time needed to capture data, causes additional problems related to patient motion. Indeed, patient motion affects the data acquisition producing blurred images. This can be easily solved by asking the patient to remain still during the examination or by constraining its motions. Nonetheless, the problem arises with involuntary motions proper of the human physiology, like respiration or heart beating. Indeed, respiratory motion affects thorax images, producing blurred images of lungs. For fast imaging modalities, the respiratory motion issue can be easily solved by asking the patient to hold breath during the short time (some seconds) the acquisition takes place. Obviously, the same procedure cannot be repeated in Emission Tomography (ET), thus more complex solutions must be incorporated to solve or compensate the effects of respiratory motion. This situation is of great relevance on early lung cancer detection, where it has been shown that respiratory motion leads to misinterpretations and imprecise diagnosis. Solutions to this problem have been proposed, yielding improvements on spatial activity distribution of lesions, but which have the disadvantages of requiring additional instrumentation, discarding part of the acquired data, etc.

In this thesis, a new motion correction method for ET is proposed. We incorporate a motion model within the reconstruction procedure, allowing to use all projection data for one single reconstruction. Obviously, it would be ideal to have the true patient's respiratory motion for this task. Unfortunately, this is rarely possible in practice since

it requires special imaging devices (e.g. a 4D scanner). Some other devices could also give some information about the patient's respiratory motion (e.g. the Real-Time Position Management (RPM) system of Varian), but they are also rare in clinical routine, and have to be coupled to an imaging system.

Here, we address the most unfavorable case, i.e. when no information about the patient's respiratory motion is available. We will thus use a motion template (either computed from data of a single subject or a population of patients), and deform it so that it adapts itself to the patient's anatomy under study. This approach is far from being realistic and remains an approximation to respiratory motion compensation. However, under the strong initial considerations, we believe that such approach can make a contribution in terms of retrospective motion compensation for emission tomography. Moreover, we find it interesting to assess the benefits of such a simplistic approach, since it represents the worse case (when no information about the patient's respiratory motion is available).

1.1 Contributions

A new approach of motion correction for ET is presented. The methodology is described under the statistical image reconstruction framework, with foundations on the MLEM algorithm. In a general respiratory motion correction framework for emission tomography, then novelties of the method are:

Modelling the deformable human body: The modelling of emissions elements as spheres that deform into ellipsoids under the action of respiration is a novelty of the method. This modelling allows to take into account the non-rigid deformations found in the breathing human thorax. Besides, under these conditions such modelling outperforms computations using classical cubic voxel modelling. The latter is of great importance when 3-D image reconstruction is performed

and storage of large system matrices is intractable, forcing on-the-fly computations.

Modelling the breathing lungs: The deformations produced inside the lungs due to breathing are modelled through a displacement vector field (or a combination of them) describing the displacements of each voxel in a discretized space. Contrary to previously proposed respiratory motion models, in which a global function rules the entire deformation of the thorax, this voxel-wise modelling allows to take into account the spatial deformation variability found within the breathing lungs without adding extra complexity to the model. Indeed, the excellent integration between this way of modelling breathing and the voxel model, greatly facilitates the deformation study of emission elements. This aspect can be further found between this breathing modelling and the image reconstruction methodology, avoiding possible modifications of the reconstruction algorithm due to the incorporation of this breathing model.

Under the initial design considerations of the method (no external respiratory tracking devices, and no data acquisition modes allowing temporal information retrieval), the novelties of the method are:

Single-subject and population based models: In the absence of a patient-based respiratory model, three approximative models are proposed. A first model, called simplified model, considers the transformation recovered from a single subject between two extremal states of respiration (expiration and inspiration). The second proposal consists in a statistical study of respiratory transformations recovered from a population. Two statistical models are derived, called STAT-1 and STAT-2. While STAT-1 takes into account two extremal states of respiration (expiration and inspiration), STAT-2 is constructed taking into account five states representing a full breathing cycle.

Retrospective motion compensation: Given our assumptions (no information is available on the respiratory motion), it comes out that the proposed method allows the retrospective respiratory motion correction of already acquired data, which is an unique feature with respect to other approaches.

Other contributions found in this thesis work are:

Implementational issues: Acceleration schemes are proposed for the time demanding task of 3-D image reconstruction. The parallelization of the proposed MLEM with motion correction algorithm is detailed.

Attenuation correction under motion correction: Attenuation correction was revisited to take into account motion. New expressions for its computation and use is given and workarounds concerning implementational issues are discussed as well.

1.2 Overview

The thesis is divided in two main parts. The first one begins with an overview of lung cancer, covering some statistics, main causes of getting lung cancer, types of lung cancer, its diagnosis and treatment. Then, in chapter 3, the data acquisition in ET is briefly reviewed. Chapter 4 presents a review of the main image reconstructions algorithms, which have been classified in two principal branches: analytical and algebraical. Under the second category, the Maximum Likelihood Expectation Maximization (MLEM) algorithm is further detailed since it is the base algorithm on which the proposed motion correction methodology was developed. Chapter 5 starts with a discussion of the impact of the respiratory motion in ET, followed by a review of motion correction techniques for ET and their possible application to respiratory motion correction.

The second part presents the proposed method of motion correction in ET and its application to respiratory motion. Chapter 7 presents

the parallel implementation and the acceleration schemes proposed to speed-up execution in 3-D image reconstruction. Results from simulated, phantom and patient data are then presented and discussed in chapter 8.

Finally, chapter 9 presents main conclusions and some possible further directions of research.

1.3 Publications

- Mauricio Reyes Aguirre, Grégoire Malandain, Jacques Darcourt, and Pierre Malick Koulibaly. Respiratory motion correction in emission tomography imaging. In *Fully Three-Dimensional Image Reconstruction Meeting in Radiology and Nuclear Medicine*, Salt Lake City, Utah, USA, July 2005.

- Mauricio Reyes Aguirre, Grégoire Malandain, Nicholas Ayache, Jacques Darcourt, and Pierre M. Koulibaly. Respiratory motion compensation within emission tomographic reconstruction. In *52nd Annual Meeting of the Society of Nuclear Medicine*, Toronto, Canada, June 2005.

- Mauricio Reyes Aguirre, Grégoire Malandain, Pierre Malick Koulibaly, Miguel A. González Ballester, and Jacques Darcourt. Respiratory motion correction in emission tomography image reconstruction. In J. Duncan and G. Gerig, editors, *Proceedings of MICCAI'05, Part II*, volume 3750 of *LNCS*, pages 369–376, Palm Springs, California, 2005. Springer Verlag.

- Grégoire Malandain and Mauricio Reyes Aguirre. La tomographie en mouvement. *Pour la science*, (338):132–137, December 2005.

- Mauricio Reyes Aguirre, Grégoire Malandain, and Jacques Darcourt. Respiratory movement correction in emission tomography. Research report 5279, INRIA, July 2004.

Others

- M. A. González Ballester, M.G. Linguraru, M. Reyes Aguirre, and N. Ayache. On the adequacy of principal factor analysis for the study of shape variability. In J.M. Fitzpatrick and J.M. Reinhardt, editors, *SPIE Medical Imaging '05*, volume 5747, pages 1392–1399. SPIE Publishing, 2005.

Chapter 2

Lung Cancer

¿From all existent types of cancer, lung cancer is currently the most common form of cancer and the most deathly worldwide [1]. It was estimated that in 2002 there were 10.9 million new cases of cancer worldwide, 6.7 million deaths, and 24.6 million persons who had been diagnosed with cancer in the previous five years. Of this, by 2002 lung cancer accounted for 1.35 million new cases (12.4% of world total) and 1.18 million deaths (17.6% of world total) [2].

Smoking is responsible for an estimated 87% of lung cancer deaths. Male heavy smokers (one or more packs of cigarettes daily) have a lung cancer mortality (death rate) 15 to 25 times higher than male nonsmokers. In female heavy smokers, the risk is two to five times greater than nonsmokers. Passive smokers, or second-hand smokers (i.e. people who breathe the smoke of others) also have a higher risk of lung cancer. For example, it has been shown that spouses of smokers have a 30% greater risk of lung cancer than do spouses of non-smokers.

Pollution and exposure to chemicals and others like asbestos or radioactive gases (e.g. Radon) are also a risk factor for lung cancer but in a minor scale compared with smoking. Personal and family history

[1] In terms of incidence however, lung cancer in men is second to prostate cancer and second in women.

[2] Source: International Agency for Research on Cancer.

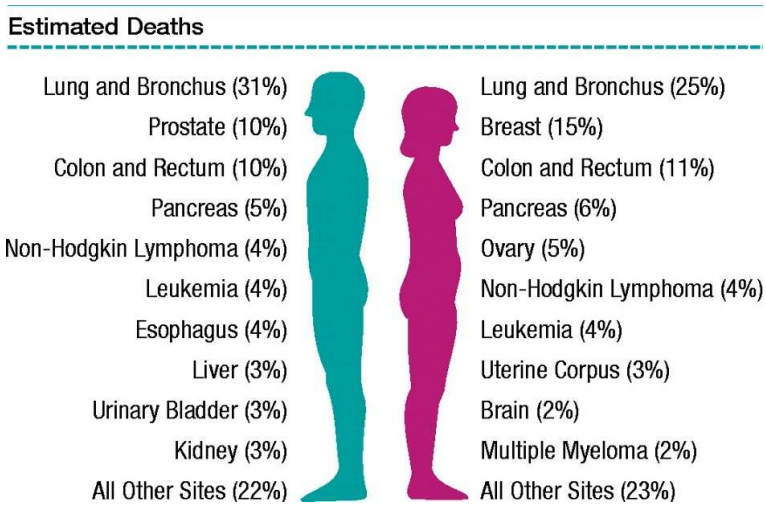

Figure 2.1: Ten leading cancer types for the estimated new cancer cases and deaths, by sex, US, 2003 [55].

influence as well the chances of getting lung cancer.

Common symptoms of lung cancer include :

- ontinuous cough which gets worse over time,
- constant chest pain,
- coughing up blood,
- shortness of breath,
- repeated problems with pneumonia or bronchitis,
- swelling of the neck and face,
- loss of appetite or weight loss,
- Fatigue.

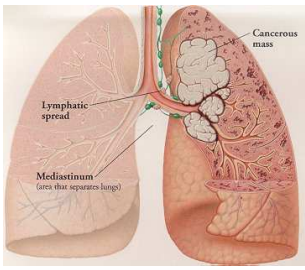

Figure 2.2: Illustration of small cell lung cancer.

2.1 Diagnosis

The diagnostic of lung cancer commonly consists in an evaluation of the symptoms, patient's medical history, smoking history, family history of cancer and exposure to environmental and occupational substances. If lung cancer is suspected, a microscopic examination of tissues obtained from a biopsy is commonly performed. If the diagnosis is cancer, its staging is obtained by imaging the patient's body. The possible modalities and/or examinations include: CT scan, Radionuclide scanning, Mediastinoscopy/Mediastinotomy.

2.2 Types of Lung Cancer

Lung cancer can be classified in two main groups, Small Cell Lung Cancer (SCLC) and Non-Small Cell Lung Cancer (NSCLC)

Small cell lung cancer: They represent between 20% and 25% of all lung cancer cases. Small cell lung cancer is characterized by a rapid growth rate and by being prone to form metastases at an early stage (typically before diagnostic). Eighty percent of small cell lung cancer is located centrally and 20% is in the periphery of the lung. Histologic verification (microscopic study of the tissue structure) by a pathologist of small cell lung cancer is mandatory because treatment is significantly different from NSCLC.

Non-small cell lung cancer: This group is commonly divided

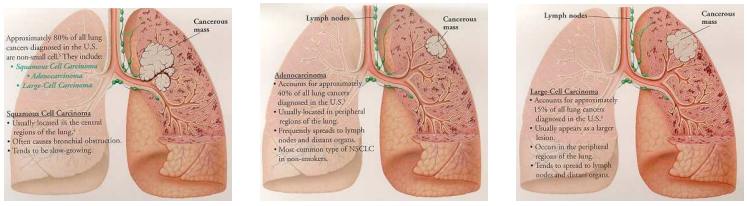

(a) Squamous cell carcinoma (b) Adenocarcinoma (c) Large cell carcinoma

Figure 2.3: Types of non-small cell lung cancer.

into three subgroups according to the type of affected cell. They are *squamous cell carcinoma*, *adenocarcinoma* and *large cell carcinoma*.

Squamous cell carcinoma is the commonest type of lung cancer accounting for over 30% of lung cancers. It develops in the cells which line the airways, without spreading (see Fig. 2.3(a)). Treatment is surgery whenever possible and the survival is of 5 year over 50% when no evidence of lymph node spread.

Adenocarcinoma (see Fig. 2.3(b)) develops from the cells which produce mucus in the lining of the airways and spreading is more likely to occur than with squamous cell carcinoma, which consequently decreases the chances of surgical removal. Five year survival rate is less than 10%.

Large cell carcinoma (see Fig. 2.3(c)) gets its name from the large, rounded cells that are seen when they are examined under the microscope. They are found in the smaller bronchi. Treatment is surgery but this is not always possible since the tumor commonly spreads early. Five year survival of patient is less then 10%.

2.3 Treatment

Surgery, chemotherapy and radiotherapy are the treatments currently used in lung cancer. The selection of the appropriate treatment (or combination of them) is based mainly in the patients' health, the type

and size of tumor and the level it has spread beyond the lungs.

For small cell lung cancer, chemotherapy (i.e. use of anti-cancer drugs to destroy cancer cells by stopping them from growing or multiplying) is the main treatment. In advanced cases, it can be used with radiotherapy (known as chemoradiation) to alleviate symptoms like pain. On the other hand, surgery is not commonly used due to the rapid spread of SCLC tumors. The aggressiveness of SCLC motivated the use of brain irradiation to deal with possible brain metastasis.

At early stages of non-small cell lung cancer, surgery can be used in conjunction with chemotherapy, which is commonly applied after surgery to prevent posterior apparitions of tumors. In cases where the patient's health does not allow surgery, radiotherapy is preferred.

If the tumor has spread to tissues close to the lung, the treatment can consist in radiotherapy, chemoradiation or just surgery. In the other hand, when the tumor has spread to other parts of the body, radiotherapy is preferred to shrink the cancer and reduce symptoms.

In brief, for NSCLC, the issue is wether or not the patient can be treated surgically. He or she will benefit from this only if the tumor is limited to certain mediastinal lymph nodes. This is why staging is important.

Chapter 3

Physical bases

3.1 Introduction

Unlike CT, MRI and other techniques that use an external source of energy to visualize different structures (measuring absorption coefficients (CT), proton density and relaxation times (MRI), etc.), in emission tomography an internal source of radiation is used instead. This source of radiation, called radio-isotope, [1] is attached to an organic molecule that serves as tracer, it is chosen accordingly to the the organ and biochemical or metabolic process to be visualized. The combination radio-isotope and tracer is commonly called radiotracer and is commonly injected into the patient's blood stream [2].

The radiotracer is uptaken by the target tissues at a degree that is proportional to the biochemical or metabolic underlying process. So, the more activity a biochemical or metabolic process has, the higher uptake of the radiotracer will occur. For example, tumoral cells present higher glucose consumption than healthy cells, so by choosing a glucose-based tracer it is possible to have a high uptake of the radiotracer on malignant cells, allowing differentiation of malignant from healthy tissues. Once the radiopharmaceutical enters the patient's blood stream,

[1] Natural or artificially created isotope of a chemical element having an unstable nucleus.
[2] Other modes of administration are via oral and inhalation.

some time is necessary before it is taken up by the target tissues. After that period of time, the patient is positioned in the detection system to begin the data acquisition. The goal of this step is to gather the gamma rays coming out of organ being studied.

Now, how these gamma rays are produced? Here, a first difference between ET modalities appears, with Single Photon Emission Computerized Tomography (SPECT) and Positron Emission Tomography (PET) being the main modalities. Fig. 3.1 shows a diagram of a PET system (left), a single head SPECT system (gamma-camera) (center) and an hybrid version called Coincidence Detection Emission Tomography (CDET) (right), which consists in two detector heads linked by a coincidence detection circuit used in conjunction with positron emitters. Let's notice that although typical SPECT systems use one detector head, more detectors heads can be added in order to increase count statistics (number of detected photons), and so to improve the reconstructed image and or to shorten the acquisition time. This is the example of two or three headed SPECT systems found in many centers.

3.2 Radio-Isotopes

As already stated, the radio-isotopes are the source of energy used in diagnostic to highlight biochemical processes, blood flow, to assess bone growth, estimate effects of surgery, etc. For PET, common radio-isotopes are ^{11}C, ^{15}O, and ^{18}F. Depending the biochemical or metabolic process to study, a tracer is chosen. In cancer studies for example, a common radio pharmaceutical labelled with ^{18}F is the [^{18}F]fluorodeoxyglucose (FDG). The convenience of using FDG for cancer detection is due to the fact that cancer cells consume more glucose than healthy cells, which is a good indicator of cell metabolism.

For SPECT, the most common radio-isotopes is ^{99}mTc. ^{99}mTc is employed in mostly 85% of all nuclear medicine procedures and its

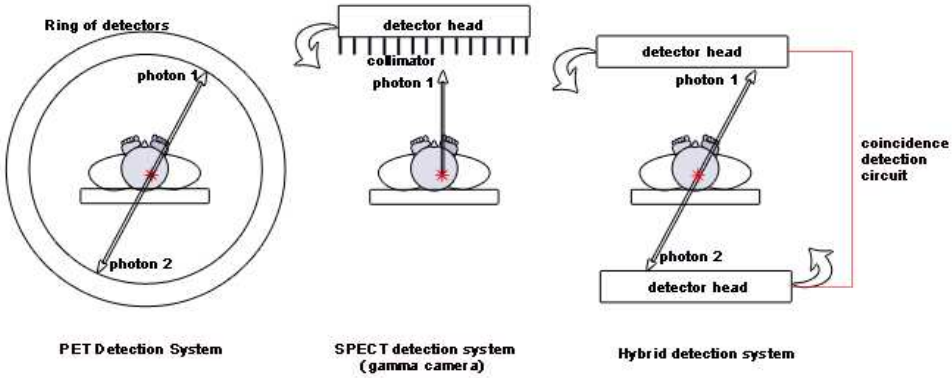

Figure 3.1: Most common configurations of emission tomography scanners. From left to right, PET detection system, one headed SPECT system and CDET detection system.

success is mainly due to:

- It has a half life of six hours, which is long enough to perform the studies yet short enough to avoid large radiation doses delivered to the patient.
- This is a pure gamma ray emitter (no high energy or beta particles).
- The gamma rays are of adequate energy levels to escape easily the human body, facilitating the data acquisition. Thus, minimizing radiation doses to the patient, and to be absorbed efficiently by the detectors.

To finalize the discussion about radio-isotopes, a final word concerning their half-life can be said. From a practical point of view, the half-life of a radio-isotope is an important issue, since on this selection, logistics and clinical procedures may differ. For instance, the half-life of FDG is of 110 minutes, which implies the existence of a

	Radioisotope	Half-life energy	Photon energy
PET	^{11}C	20.4 min	511 keV
	^{15}O	1.72 min	511 keV
	^{18}F	109.0 min	511 keV
SPECT	^{99}mTc	6 h	140 keV
	^{123}I	13 h	159 keV

Table 3.1: Common radioisotopes used in PET and SPECT. Half-lives and photon energy are presented.

cyclotron nearby the clinical center. Thus, making more expensive its use. Nonetheless, the use of FDG is increasing rapidly, due to its efficacy as metabolic indicator.

The next sections present each modality separately. This presentation and descriptions are mostly inspired and based on the work of Marine Soret, more detailed information can be found on her thesis work [108].

3.3 PET Imaging

3.3.1 PET Photon Detection

In PET imaging the unstable nucleus of the radio-isotope reaches stability by emitting positrons, which after travelling some millimeters (phenomenon called *positron range*) lose enough energy to reach a nearly steady state. At this point, the positron annihilates with a nearby electron producing two 511 keV gamma photons which are emitted in nearly opposite directions.

In the literature the term Line-Of-Response (LOR) is typically used to describe the line formed between the position of the two photons being detected. The term detector tube, or detector unit [104] is also used but with less frequency.

In PET imaging, the detection device is made of several adjacent rings of detectors. 2-D and 3-D acquisition mode are currently available. For 2-D acquisitions, septa are placed between rings. The distance between septa is chosen in order to allow detection of photons between adjacent detector rings. In 3-D mode, no septa is placed, so coincidence detection between non-adjacent detector rings is allowed.

3.3.2 Performance in PET imaging

PET cameras can use various scintillator crystals. The most commonly used nowadays are BGO, CSO, and LSO.

The main factors characterizing the performance of a PET system are

- **Spatial resolution:** It mainly depends of the detector characteristics (crystal, detector block, etc.). The spatial resolution of current PET scanners is in the range of 4-6 mm.

- **Energy resolution:** It is related to the capacity of the crystals to detect the energy levels of incoming photons. Depending on the scintillator it varies between 15% and 25%.

- **Sensitivity:** It refers to the number of events detected with respect to the number of events produced. It depends on the size and type of scintillator crystals and the diameter of the ring.

- **Dead time:** It refers to the time needed by the detection system to be ready to detect new incoming photons. It is of the order of nanoseconds.

- **Scattered photons rate:** Photons being scattered by interaction with matter are detected at an erroneous location. The rate of scattered photons depends mostly on patient characteristics, acquisition modes and energy resolution.

3.3.3 Degrading factors in PET imaging

Random Coincidence

In coincidence detection, if for two annihilations events one photon of each pair gets absorbed or goes undetected due to scattering and the others are detected within the coincidence timing window, then an Accidental Coincidence (AC) will be produced (called Random detections). Similarly to Compton scattering, accidental coincidences contributes to background noise.

Random Coincidence Correction

Accidental coincidence correction is performed by estimating the number of accidental coincidences by LOR to then subtract this number to the original projections. Two methods exist to perform such estimation.

A first method consists in performing a delayed coincidence detection. Then, since the coincidence detections in the delayed window have the same mean as the AC events in the non delayed detection, a subtraction is performed in real time between the delayed and the non-delayed sinogram data.

The second method consists in estimating the rate of AC events from the total number of single detected photons. Let S_{d_1} and S_{d_2} be the rate of single photons detections for detectors d_1 and d_2 respectively. And let be τ the coincidence timing window. It can be shown that for the detector d_1, on average, $2\tau S_{d_2}$ single photon detections occur for detector d_2 during the coincidence timing window τ. Thus, the rate of AC events between detector d_1 and d_2 is found to be

$$S_{d_1 d_2} = 2\tau S_{d_1} S_{d_2}.$$

Attenuation

As photons go through the body and interact with matter by photoelectric interaction, which produces that some of them can go undetected. This phenomenon is termed as *attenuation* and it is typically modelled according to Beer's law, which states that the probability of detecting a photon that has traversed a path of length l throughout a medium with a linear attenuation coefficient μ is:

$$P\{detected\} = e^{-\mu l}. \tag{3.1}$$

Eq. (3.1) establishes that the detection probability is lower for photons coming from the center of the system than for photons coming from the outside regions of the body. Besides, for photons traversing materials with high attenuation coefficient values, it is more likely that these photons will not reach the detector and thus they will go undetected, contrary to those traversing materials with lower attenuation coefficients (e.g. air).

In other terms, if a number N_i of photons traverse a given material M of thickness l with an attenuation coefficient μ_m, the number of photons N_i leaving the material is given by:

$$N_i = N_o e^{-\mu_m l}. \tag{3.2}$$

If we consider now that the material M is composed by two layers of thickness l_1 and l_2 ($l = l_1 + l_2$) and attenuation coefficients μ_1 and μ_2 respectively, the number of photons N_i leaving the material will be:

$$N_i = N_o e^{-\mu_1 l_1} e^{-\mu_2 l_2} = N_o e^{-(\mu_1 l_1 + \mu_2 l_2)}. \tag{3.3}$$

For a non-uniform attenuating medium, an attenuation map $\mu(x)$ is considered. Eq. (3.2) can be generalized to:

$$N_i = N_o e^{-\int_l \mu(x) dx}. \tag{3.4}$$

In PET imaging due to the photon physics, attenuation correction is independent of the position where annihilitation takes place along a LOR.

The global effect of attenuation is that some regions on the reconstructed image will have lower uptake values than in the non attenuated case.

Attenuation correction

To perform attenuation correction, it is necessary to obtain a map of attenuation correction factors (ACF). For this, an x-ray CT or external transmission sources can be used. Then, attenuation correction can be performed in two ways. A first method consists in correcting the projection data by multiplying an ACF, corresponding to the rate between the transmission projection data without the object and the projection data with the object, and the emission projection data.

A second method consists in incorporating the ACF map within the step of image reconstruction in the form of a weighting scheme. From the ACF map, weights are computed for each projection bin, and used as multiplicative terms on the bins.

Scattering

The photon in its way out of the body collisions with an atom, resulting in the ejection of an electron and a scattered photon of lower energy. This is known as Compton scattering (also known as incoherent scattering) that is different from Thompson or Rayleigh scattering (also known as coherent scattering), in which the scattered photon does not lose part of its energy. In ET, Compton scattering effects are more important than those caused by Thompson scattering, and are considered for further corrections.

Compton scattering results in photons being mistakenly detected, which affects the resolution of the reconstructed images [66]. Besides,

even though correction methodologies exist, Compton scattering contributes to background noise, which reduces the image contrast.

Scattering correction

Compton scatter causes a change of direction in the ejected photon's trajectory and a decrease in its energy. Commonly, scatter correction has been performed relying on energy selection. Unfortunately, the window limits at high energies are not easy to set due to the limited energy resolution of the detector system, which causes overlapping between scatter and non-scatter energy bands. Several approaches exist to estimate the number of scattered photons

- A simple and fast approach consists in estimating scattered photons in different energy windows with respect to the photopic energy. These scattered data are then subtracted from the data acquired with the photopic energy window.
- From image segmentation of the attenuation map of the object, all emissions events originated outside the contour of the object (given by the segmentation) are supposed to be scattered events, with a Gaussian distribution. This distribution is used to estimate the scattered events inside the object. This methodology is only valid in the case the activity is homogeneous in the object.
- Similar to the previous method, estimation of the scattered photons outside the object is also performed. The scattered distribution inside the object is now estimated from the attenuation map and Monte-Carlo simulations.

Other factors degrading the image in PET are:

- In PET, the distance travelled by positrons before they annihilate with an electron affects resolution as well. This distance depends on the positron energy and density of the tissue. This way, lower positron energy radioisotopes are preferred.

- Although positrons lose nearly all of their momentum before annihilation, the positron and electron have some residual momentum when they annihilate. This produces a loss of resolution because the annihilation point no longer falls within the detected LOR. This, summed to the positron range phenomenon, limits physically the spatial resolution to an estimated range of 2-3 mm [74] for the the clinical scanners.

3.4 SPECT Imaging

3.4.1 SPECT Photon Detection

For SPECT imaging the process is simpler, no annihilation process occurs, the radio-isotope reaches stability by emitting a single photon with an energy between 50 keV and 600 keV, which is captured by the rotating detector system. However, since in SPECT imaging only one photon is detected, no information is available to determine the direction of the incoming photon. To overcome this problem, SPECT detectors constraint the range of angles at which the incoming photons are accepted. This is performed by adding a collimator to the head detector so the direction of detected photons is constrained to known values. Conversely, the double photon detection of PET allows to determine the direction of the incoming detected photons, so no collimator is needed. Thus, this increases the total number of detected photons in comparison to the reduced total count of SPECT. This results in higher sensitivity and resolution of PET compared to SPECT systems.

A typical detector is composed by a set of scintillation crystals (typically Thallium-activated Sodium Iodide [NaI(Tl)] (or a single crystal, i.e. Anger camera) coupled optically to photomultipliers tubes (PMT). When a photon arrives, it interacts with the scintillation crystal(s) producing photons. The photons are amplified by the PMT's and transformed into an electrical signal, which is electronically processed to add

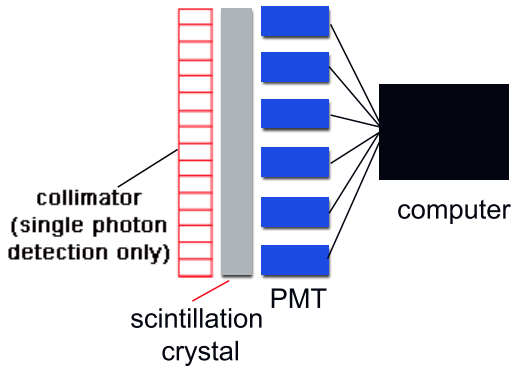

Figure 3.2: Main components of a detector system.

a new annihilation event to the corresponding detection counts. Figure 3.2 summarizes the main components present in a detector.

3.4.2 Performance in SPECT Imaging

The factors influencing the performance of a SPECT system are:

- **Spatial resolution:** It depends on the collimator, crystals, photomultipliers and electronics. Current SPECT systems have a resolution without collimator varying between 3 and 4 mm and of 10 and 12 mm with collimator.

- **Energy resolution:** Current devices have an energy resolution varying between 10% and 15% of the photopic energy.

- **Geometrical linearity:** It refers to the precision capacities of the crystals to determine the impact position of incoming photons.

- **Sensitivity**

3.4.3 Degrading factors in SPECT imaging

Distance-dependent detector response

For single photon detection, collimators are necessary to constraint the direction of incoming photons. Nevertheless, such constraint has a limited precision range. Indeed, the collimator holes have a relatively large hole diameter to obtain a reasonable efficiency, which results in photons with non-parallel directions being detected as such. This effect increases towards the center of the image and it can be modelled as a Gaussian whose FWHM increases linearly with the source-to-detector distance. The global effect of the distance-dependent detector response is a non-stationary blurring of reconstructed images.

A number of methods have been proposed for detector-response compensation (DRC). They mainly include restoration filtering [34, 45] and iterative DRC schemes.

With restoration filtering, a one-time deconvolution is performed on the sinogram data before reconstruction. It consists in studying the relationship between the contribution of points at different source-to-detector distance to specified frequency regions in the discrete Fourier transform of the sinogram, this is known as the frequency distance principle (FDP) [34]. Some advantages of restoration filtering are its low computational load, its capacity to achieve an approximately stationary, isotropic tomographic point response [34], and its improved quantitative accuracy over low-pass filters [92]. Some of the disadvantages of restoration filtering are its limited resolution recovery due to noise amplification; the FDR does not account itself for attenuation, and FDR is a poor approximation at low frequencies [62].

In iterative schemes, a distance-dependent response model is incorporated in an iterative algorithm. Although these methods are computationally more intensive than restoration filtering, it has been shown that iterative schemes give better results [62]. Among these methods, the Gaussian diffusion methodology has shown to outperform other

methods. It implements the detector response incrementally with narrower convolution kernels, enabling with this, acceleration of the iterative process and images with improved detector-response compensation [35, 62].

Septal penetration

This phenomenon occurs when high energy photons traverse the barrier imposed by the collimator, producing incorrect detections. It must be said that this phenomenon occurs only for radioisotopes producing high energy photons like ^{131}I and ^{123}I. Another similar phenomenon is the septal scattering which consists in detected photons scattered by the collimator.

Attenuation correction

For SPECT imaging, the task of attenuation correction is more complex than in PET imaging (mainly due to the fact that attenuation correction in PET is independent of the position where the annihilation takes place) [5]. The simplest method of attenuation correction in SPECT is the one proposed by Chang [19]. It consists in reconstructing a preliminary image by means of a filtered backprojection algorithm. Then, each pixel of this image is divided by an attenuation coefficient computed as the average value of attenuation coefficients affecting the given pixel over each projection angle. An iterative approach exists also but it is limited to non-complex activity and attenuation distributions. Furthermore, the number of iterations is limited by noise amplification issues [108].

Scatter correction

To correct for scattering in SPECT imaging, the principle of observing the energy of scattered photons is also applied.

A first method consists for example in 140 keV ^{99} mTc imaging to apply an energy window of width 20% around the photopic energy of the radioelement (126-154 keV).

Other methods perform an estimation of scattered photons in the 20% energy window from different energy windows. The estimated scattered contribution is then subtracted from the data. The method proposed by Jaszczak [54] follows this principle, it can be described with the following relationship

$$p_p = p_{20\%} - kp_d. \tag{3.5}$$

Where $p_{20\%}$ corresponds to the projection data in the 20% energy window, p_d is the projection set corresponding to an energy window with a high probability of scatter, k is a scale factor and p_p the scattered corrected projections.

A third method called Triple Energy Window (TEW) uses two energy windows to estimate the scattered distribution. The scattered corrected data is then computed as

$$p_p = p_{20\%} - k(p_1/w_1 + p_2/w_2)w_{20\%}/2. \tag{3.6}$$

Where, p_1 and p_2 are the projection data for each of the supplementary energy windows, w_1, w_2 the width of these energy windows and $w_{20\%}$ the width of the 20% energy window.

More sophisticated approaches (see [14] for a comparative study of scatter corrections) take into account the fact that scattering is depth-dependent and related to the electron density of the matter the photons traverse. Model-scattering uses both, the transmission and emission scans in conjunction with the physics of Compton scattering to estimate the scatter distribution [86]. However, these methods do not account for scattering outside the FOV, which is an active focus of research,

especially in fully 3-D PET where it has been shown that between 30% and 50% of the detected photons correspond to scatter data [115, 127].

3.5 CDET Imaging

The Coincidence Detection Emission Tomography (CDET) can be considered as the poor man's PET. It simply consists in two coupled parallel γ-camera that rotate around the patient, and that are able to detect a coincidence of photon detections (one per γ-camera). It should be noticed that, with respect to a PET camera, a lot of events will not be detected.

3.6 Partial Volume Effect

A very brief discussion about the partial volume effect (PVE) is given here.

The PVE problem appears due to the limited resolution of the detector system in both PET and SPECT imaging. The intensity of a punctual radioactive source (whose radioactive distribution would normally also appear as a punctual intensity) will appear spread out around the point. The main effects of the partial volume effect are: it makes difficult the detection of small structures and it produces under estimation of quantitative measures. The importance of this under-estimation is bound to several factors, like size and shape of the structure, structure-to-neighborhood activity ratio, spatial resolution of the detection system, angular sampling [108]. This phenomenon is an important obstacle to quantification. As an example, in 18FDG PET with a spatial resolution of 7mm, there is an underestimation of 85% of the uptake of a spherical lesion of 5cm of diameter.

Methods to deal with the PVE problem have been proposed. They can be classified in two types; those using a deconvolution operation between the measured activity and the detector response function,

and those using additional anatomical information and the detector response function (see [108] for a comprehensive discussion of correction methododologies and results obtained in brain SPECT and PET thorax studies).

3.7 Storing projections

So far we have seen how the gamma rays, coming out of the body, are detected and processed by the detection system. Now, it is of our interest to describe how the gamma rays, which are projections of the tracer distribution, are stored for posterior processing.

The discrete nature of the detection system, results in a limited set of possible detector tubes configurations. The number of incoming photons (i.e. projections) are then stored in one of these configurations. In other words, we are interested in the number of occurrences a pair of photons or single photons reach a given detector tube. This information is stored in what is known as *sinogram*. Figure 3.3 shows an example of a 2-D sinogram image, where vertical represents the angle of detection, and the horizontal axis the position of the event on the detector. Another structure of sinogram is the so-called *list-mode* data format, which is used in PET. In list-mode data each annihilation event is stored separately along with a time tag indicating the detection time.

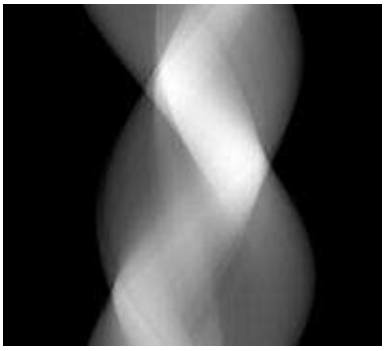

Figure 3.3: Example of a sinogram image. A point source in space will generate a sinusoidal trajectory in the sinogram space.

Chapter 4

Reconstruction Algorithms

The aim of an image reconstruction algorithm is to obtain a visual representation of a physical quantity from a set of indirect measurements [47]. In ET, this physical quantity corresponds to the spatial radiopharmaceutical concentration, and the indirect measurements correspond to photon counts recorded by scintillation detectors. Once the counts are acquired, (i.e., projections) an algorithm is applied to obtain an image of the spatial distribution generated by the radio-isotope. The reconstruction of projections is unfortunately an ill-posed problem [1], which makes its resolution difficult. Current algorithms can be grouped in two main branches: analytical and algebraical algorithms. Due to the vast variety of existent algorithms, this chapter presents a brief review of common image reconstruction algorithms, which is by no means a complete description of them (see [25] for a more detailed classification and description), but just intended to show the main features they present, which can further help to better understand how motion correction has been incorporated into the step of image reconstruction.

[1] In the sense of Hadamard, a problem is well-posed if a solution exist, it is unique and it depends continuously on the data

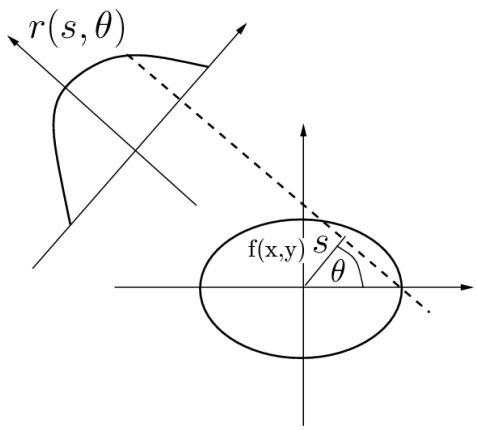

Figure 4.1: The Radon transform.

4.1 Analytical Algorithms

The analytical algorithms are based on an analytical model of the acquisition process, this model is based on the Radon transform [2].

$$r(s,\theta) \triangleq R\{f\} = \int_{-\infty}^{\infty}\int_{-\infty}^{\infty} f(x,y)\delta(x\cos\theta + y\sin\theta - t)dxdy \quad (4.1)$$

Where $r(s,\theta)$ represents the set of line integrals (i.e. projections) passing through the object $f(x,y)$ (see Fig. 4.1). The problem consists in finding $f(x,y)$ from $r(s,\theta)$, which is to inverse the Radon transform.

4.1.1 The backprojection operator

An approach to find $f(x,y)$ is to apply the backprojection operator. Mathematically, the backprojection operator is defined as

$$f_{BP}(x,y) = \int m(x\cos\theta + y\sin\theta, \theta)d\theta. \quad (4.2)$$

[2]We discuss the 2-D case, although the extension to 3-D can be readily generalized.

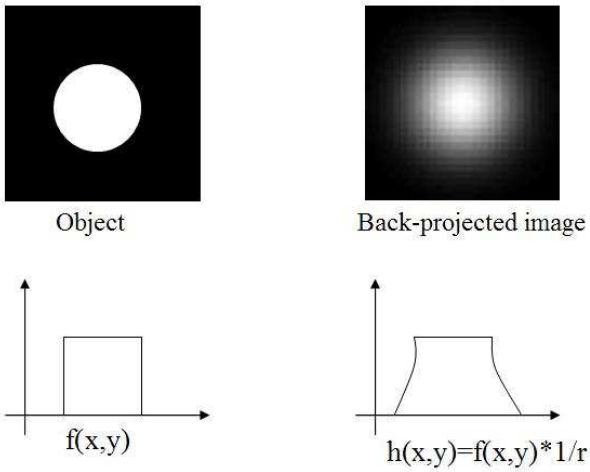

Figure 4.2: Direct backprojection of projections generated by object $f(x, y)$ (left) results in a blurred reconstructed image $h(x, y)$ (right).

Direct application of (4.2) produces images with a blurring component that is commonly modelled as the result of a convolution between the ideal reconstructed image and an inverse radial function, see Fig. 4.2.

A first and evident solution is the application of a deconvolution operator,

$$h = f \diamond \frac{1}{r}$$
$$H = F\frac{1}{\rho} \quad \text{with} \quad H = FT_{2D}(h) \quad \text{and} \quad 1/\rho = FT_{2D}(1/r)$$

where $\diamond$ is the convolution operator.

Then, f can be easily found by application of the inverse Fourier transform

$$f = FT_{2D}^{-1}(\rho H). \tag{4.3}$$

This approach although simple and easy to implement, presents the major problem of noise and signal bands overlapping, which in practice

results in a tradeoff between noise reduction and signal quality. The filtering step amplifies high frequencies of the noise component, but this is part of the radon transform inversion.

In practice the high frequencies amplification can be limited by applying a band-limited filter or variants of the ramp filter (e.g. Hamming, Hann, Parzen, etc.). However, the tradeoff between noise and signal bands is always present.

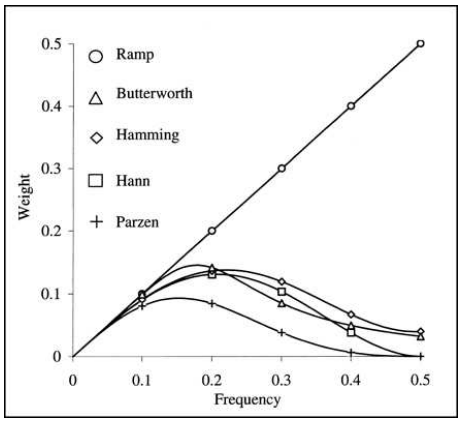

Figure 4.3: Different filters used in FBP. Ramp filter alone increases the high frequencies. Low pass filters associated with the ramp filter limit the noise component.

4.1.2 The approach given by the Central Slice Theorem

An alternative approach is given by the *Central Slice Theorem.* It relates the 2-D Fourier transform of the image with the 1-D Fourier transform of its projections (See appendix A.2 for an example of this).

> *"Unidimensional Fourier transform of the Radon transform with respect to the radial variable equals the bidimensional Fourier transform of the object."*

The Central Slice Theorem states that the 2-D FT of $f(x, y)$ along

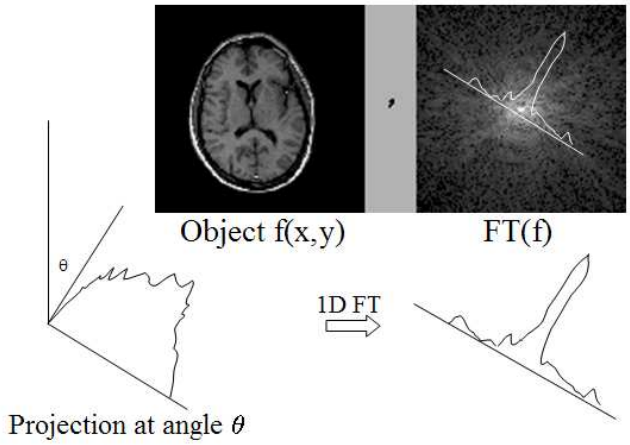

Figure 4.4: The Central Slice Theorem. Given an object $f(x, y)$, its 2-D FT along a line at a given angle equals the 1-D FT of the projection profile of $f(x, y)$ at the same angle.

a line at angle θ, is given by the 1-D FT of $m(t, \theta)$. Fig. 4.4 depicts this.

The Central Slice Theorem allows one to perform the operations directly over the projection data. This way, a 1-D Fourier transform is applied to each projection profile followed by a filtering step. Finally, inverse 1-D FT operations are performed to the filtered profiles followed by a backprojection operation.

This method is known as the *Filtered Backprojection* algorithm (FBP).

However, the image reconstruction in emission tomography is an ill-posed problem [116], which produces noisy images due to the incompleteness of the projection data. As a consequence, images reconstructed with FBP suffer from heavy noise and are prone to streaks artifacts. Furthermore, the filtering step amplifies high frequencies, incrementing the noise level. As it was stated, this effect can be decreased by applying a window function to the filter but with the need

of considering a trade-off between noise level and image resolution.

The FBP method was widely preferred as reconstruction method. However, the apparition of algebraical algorithms has contributed to the replacement of the FBP by these new types of algorithm. Since the number of algorithms encountered nowadays is large, a review of the most typical algorithms is presented in the next section.

4.2 Algebraical Algorithms

Unlike the analytical algorithms, iterative algorithms allow better modelling of the acquisition and emission process. Besides, the modelling is discrete and not continuous as in the analytical case (not considering the implementation). Generally speaking, the idea consists in, given a set of measurements $\mathbf{p}$ and the projection matrix $\mathbf{R}$, which models the acquisition, to find the set of values $\mathbf{f}$ that accomplish the relation $\mathbf{p} = \mathbf{R}\mathbf{f}$. It will be shown later how the matrix $\mathbf{R}$ can be constructed and what other type of information can be added to it.

Use of direct algebraical methods to obtain $\mathbf{f}$ is not possible due to the large size of the matrix $\mathbf{R}$. Besides, noise in $\mathbf{p}$ and the approximation of $\mathbf{R}$ does not allow an exact solution of $\mathbf{f}$ [3]. Furthermore, use of least-squares and pseudo-inverse may yield negative values.

Algebraical methods overcome these problems using an iterative approach [48]. At each iteration, a projection of the guessed image is performed, which is compared, by means of some criteria, with the measured data (i.e., $\mathbf{p}$). The error produced is feedback into the guessed image, and a new iteration is performed. The problem with this type of approach is that as the number of iterations increase the quality of the reconstructed image increases progressively but convergence cannot be obtained since noise increases after many iterations. This is related to the ill-posedness of the problem.

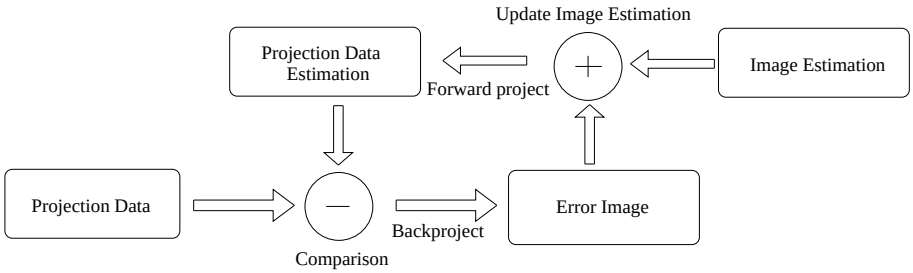

Figure 4.5: The basic idea behind algebraical reconstructions algorithms. Iteratively, a new image estimate is computed and its forward projection is compared with the acquired projection data. The residual error is backprojected into the image space to update the image estimation.

4.2.1 Introduction to the MLEM statistical approach

An algebraic solution for tomographic image reconstruction considers a statistical modelling of the emission process[3]. The problem is reformulated as a discrete one, which facilitates image reconstruction, display and storage in computer systems. The goal is to estimate an unknown vector $\boldsymbol{\lambda} = [\lambda_1, \ldots, \lambda_n]$ from a realization $\boldsymbol{p} = [p_1, \ldots, p_m]$ of the measurement random vector $\mathbf{P}$. With λ_b being the mean value of emissions from the parameterized emission element $b = 1, \ldots, n$ (i.e., pixel or voxel), and p_d being the number of outcomes being detected by the detector tube d [4].

The outcome process is typically modelled by a Poisson distribution with the mean number of detections modelled as follow:

$$\overline{p_d} = E[p_d] = \sum_{b=1}^{n} \lambda_{db} = \sum_{b=1}^{n} \lambda_b R_{db}. \tag{4.4}$$

Where λ_{db} stands for the mean number of emissions from element

[3]It is also valid for the transmission case, although the derivation of statistical-based algorithms for transmission has been shown to be more difficult.

[4]For annihilation coincidence detection the detector tube is defined by the two photons detected in coincidence, whereas for single photon detection, collimation is used to define it.

b being detected by detector tube d, and R_{db} denotes the probability that a certain emission from b is detected by the detector tube d. The projection matrix $\mathbf{R}$ (or called by some authors *system matrix* or *transition matrix*) is quite important since it establishes the link between emissions and detections, that is to say, between measurements and unknowns. To construct it, pure geometrical or statistical-based considerations can be used [73]. Besides, other correction factors can be included either inside the projection matrix or in the form of multiplicative matrix, which can be factored out as a single projection matrix.

To estimate vector $\boldsymbol{\lambda}$, a likelihood-based estimator is commonly used [104]. The Maximum-Likelihood (ML) estimate $\hat{\boldsymbol{\lambda}}_{\boldsymbol{ML}}$, has the following form:

$$\hat{\boldsymbol{\lambda}}_{\boldsymbol{ML}} = \arg\max_{\lambda}[l(\boldsymbol{\lambda})], \tag{4.5}$$

with $l(\boldsymbol{\lambda})$

$$l(\boldsymbol{\lambda}) = P(\boldsymbol{p}|\boldsymbol{\lambda}), \tag{4.6}$$

the likelihood of getting a set of measures $\boldsymbol{p}$ given the image $\boldsymbol{\lambda}$.

Under a Poisson distribution modelling and independent emission measurements, $\hat{\boldsymbol{\lambda}}_{\boldsymbol{ML}}$ can be equivalently found in an easier way, by maximizing the log-likelihood function $L(\boldsymbol{\lambda})$:

$$\hat{\boldsymbol{\lambda}}_{\boldsymbol{ML}} = \arg\max_{\lambda}[L(\boldsymbol{\lambda})], \tag{4.7}$$

with $L(\boldsymbol{\lambda}) = \log(P(\boldsymbol{p}|\boldsymbol{\lambda}))$.

However, since tomographic reconstruction is an ill-posed problem [5], maximization of (4.7) tends to produce noisy images. It means that the log-likelihood estimator by itself is not able to find the "most acceptable" image. there are two ways of solving this difficulty. One way is to stop the iterations after an arbitrarily chosen number of steps (experimentally defined). The other way is the incorporation

[5] There exist many possible solutions of $\boldsymbol{\lambda}$ compatible with the measurements $\boldsymbol{p}$.

of a regularization scheme that modifies the objective function to be maximized and guide the image reconstruction towards likely images. In other words, towards images presenting features accordingly to the assumptions made for the true images.

Mathematically speaking, the new objective function can be written as

$$\hat{\boldsymbol{\lambda}}_{\boldsymbol{PL}} = \arg\max_{\lambda}[L(\boldsymbol{\lambda}) - \beta R(\boldsymbol{\lambda})]. \tag{4.8}$$

Where, $R(\boldsymbol{\lambda})$ denotes the regularization function and β is an hyper-parameter to be adjusted. Appendix A.3 describes the derivation of the MAP-based algorithms, while Appendix A.6 presents a case of implementation of a penalized MLEM.

4.2.2 The Maximum Likelihood Expectation Maximization (MLEM) algorithm

The MLEM algorithm, developed by Shepp and Vardi [104], and Lange and Carson [68], presents a way to solve for

$$\hat{\boldsymbol{\lambda}} = \arg\max_{\lambda} \Phi,$$

with Φ being either the un-penalized or penalized objective function.

The convenience of this algorithm comes from its ability to produce an iterative and monotonic algorithm capable of dealing with the major difficulty encountered in the formulation of the ML estimator under a Poisson model: the maximization of Φ. How this maximization is achieved can be seen under perspective of the optimization transfer principle (Appendix A.4).

Let's consider the un-penalized case, where the objective function is written and manipulated more easily in its log-likelihood form (see Eq.(4.7)).

$$
\begin{aligned}
L(\boldsymbol{\lambda}) &= \log\left(P(\boldsymbol{p}|\boldsymbol{\lambda})\right) = \log\left(\prod_d e^{-\overline{p_d}} \frac{\overline{p_d}^{p_d}}{p_d!}\right) && (4.9)\\
&= \sum_d \left[p_d \log(\overline{p_d}) - \overline{p_d} - \log(p_d!)\right]. && (4.10)
\end{aligned}
$$

By incorporating (4.4) into (4.10) one can find an expression in terms of $\boldsymbol{\lambda}$, as follows:

$$
L(\boldsymbol{\lambda}) = \sum_d \left[p_d \log\left(\sum_b \lambda_b R_{db}\right) - \sum_b \lambda_b R_{db} - \log(p_d!)\right] \qquad (4.11)
$$

Unfortunately, maximization of (4.11) is intractable because of the nested sums. To overcome this problem a first component present in every EM approach is used. Instead of using the incomplete data $\boldsymbol{p}$ (i.e., observed data giving no direct access to the hidden data set $\boldsymbol{\lambda}$), a complete data set (i.e., set of random variables that in general were not observed, but that could have simplified the estimation if they had been observed) is used.

In [104], Shepp and Vardi proposed to use as complete data the number of detections captured by detector tube d and emitted by voxel b (i.e. p_{db}). This selection favors the estimation of the ML estimator. In fact, if Eq. (4.9) is re-written now using the complete data, the log-likelihood is:

$$
\begin{aligned}
L(\boldsymbol{\lambda}) &= \log\left(P(\boldsymbol{p}|\boldsymbol{\lambda})\right) = \log\left(\prod_{d,b} e^{-\lambda_{db}} \frac{\lambda_{db}{}^{p_{db}}}{p_{db}!}\right)\\
&= \sum_{d,b} \left[p_{db} \log(\lambda_{db}) - \lambda_{db} - \log(p_{db}!)\right]. && (4.12)
\end{aligned}
$$

This way, maximization of the log-likelihood in (4.12) is much more easier to perform than in (4.10). Indeed, taking first derivative of (4.12)

$$
\begin{aligned}
\frac{\partial L(\boldsymbol{\lambda})}{\partial \lambda_b} &= \frac{\partial}{\partial \lambda_b}\left(\sum_{d,b} -\lambda_{db} + \log\left(\frac{{\lambda_{db}}^{p_{db}}}{p_{db}!}\right)\right) \\
&= \frac{\partial}{\partial \lambda_b}\left(-\sum_b \lambda_b \sum_d R_{db} + \sum_{d,b} p_{db}\log(\lambda_b R_{db}) + Cst\right) \\
&= \frac{\partial}{\partial \lambda_b}\left(-\sum_b \lambda_b \sum_d R_{db} + \sum_{d,b} p_{db}\log(\lambda_b) + Cst\right)
\end{aligned}
$$

$$
\begin{aligned}
\frac{\partial L(\boldsymbol{\lambda})}{\partial \lambda_b} = 0 \quad &\Leftrightarrow \quad -\sum_d R_{db} + \sum_d \frac{p_{db}}{\lambda_b} = 0 \\
&\Leftrightarrow \quad \hat{\lambda}_b = \frac{\sum_d p_{db}}{\sum_d R_{db}} \qquad (4.13)
\end{aligned}
$$

Here, a second ingredient of the EM algorithm is incorporated. Since we do not have access to the complete data p_{db}, Eq. (4.12) is replaced by its conditional expectation given the measures p_d and the current estimate λ. Let's define this as $Q(\boldsymbol{\lambda}, \boldsymbol{\lambda}^{<K>})$, which has the following form:

$$
Q(\boldsymbol{\lambda}, \boldsymbol{\lambda}^{<K>}) = E[\log(P(p_{db}|\boldsymbol{\lambda}))|p_d, \boldsymbol{\lambda}^{<K>}] \qquad (4.14)
$$

Further, remembering that for independent Poisson variables X,Y with means λ_X, λ_Y, the expectation of X conditioned on the sum $X+Y$ is $E[X|X+Y] = \frac{(X+Y)\lambda_X}{\lambda_X+\lambda_Y}$ [104]. Thus, $Q(\boldsymbol{\lambda}, \boldsymbol{\lambda}^{<K>})$ can be calculated as

$$
E[p_{db}|p_d, \lambda] = \frac{p_d \lambda_{db}}{\sum_{b'} \lambda_{db'}} = \frac{p_d \lambda_b R_{db}}{\sum_{b'} \lambda_{b'} R_{db'}} \qquad (4.15)
$$

Then, substituting equation (4.15) into (4.13) we get

$$
\lambda_b^{<K+1>} = \frac{\lambda_b^{<K>}}{\sum_d R_{db}} \sum_d \frac{p_d R_{db}}{\sum_{b'} \lambda_{b'}^{<K>} R_{db'}} \qquad (4.16)
$$

The pseudo-code for the MLEM algorithm is

Algorithm 4.2.1: EM($MLEM$)

for $K \leftarrow 0$ **to** n-iterations

do $\begin{cases} \overline{p_d} = \sum_d R_{db}\lambda_d^{<K>}, d = 1, \ldots, M. \\ \textbf{for } b \leftarrow 1 \textbf{ to } N \\ \quad \textbf{do} \begin{cases} C_b^{<K>} = \sum_d \frac{p_d R_{db}}{\sum_{b'} \lambda_{b'}^{<K>} R_{db'}} \\ \lambda_b^{<K+1>} = \lambda_b^{<K>} C_b^{<K>} / \sum_d R_{db} \end{cases} \end{cases}$

4.2.3 Properties of the MLEM and stopping criteria

The principal characteristics of the MLEM algorithm are its non-negativity (i.e., it assures non-negative pixel values for all the images generated, provided one starts with a non-null image) and, for every iteration the number of emissions equals the number of detections.

One aspect that still remains open is to figure out when the iterations should be stopped. Several measures exist that can be used to check the quality of the reconstructed image, and can be used as stop criteria. In [72, 63], the authors present the Root Mean Square value (RMS) as a good figure-of-merit

$$RMS_K = \sqrt{\frac{\sum_b (f_b - \lambda_b^{<K>})^2}{\sum_b f_b^2}}. \tag{4.17}$$

With f_b the number of emissions from b. Previous studies of the RMS value show that it begins by decreasing continously until a minimum is reached, and then starts to increase, which indicates that noise in the measured data begins to be added to the reconstructed image [64].

Since the RMS value has only utility in simulations studies, where the density distribution can be known a priori, it can not be applied to real studies.

The likelihood of the objective function can also be used as a statistical stopping criteria:

$$L(\lambda) = \sum_d [p_d \log(\overline{p_d}) - \overline{p_d} - \log(p_d!)] \tag{4.18}$$

Using equation (4.4) in (4.18), the likelihood can be calculated as:

$$L(\lambda) = \sum_d [p_d \log\left(\sum_b \lambda_b R_{db}\right) - \sum_b \lambda_b R_{db} - \log(p_d!)] \tag{4.19}$$

The problem of using equation (4.19) is that, as the iterations continue, the likelihood will increase (monotonicity of the solution), without indicating the point where noise will begin to be added to the reconstructed image.

In [22], the author presents a stopping criteria that consists in separating randomly the projection data in two halves, namely A and B. Then, one proceeds with the reconstruction of the set A, and for each iteration the likelihood of the data set B is calculated using the estimates obtained with A. It is shown that the likelihood will increase up to a certain point. At this point the iterations over A are stopped, changing to the data set B. Once both points of convergence are reached, the two estimates are summed up to obtain the final image estimate of the density distribution. This technique has shown good results on noise rejection but as it has been remarked in [56] that the cross-likelihood is dependent of the number of counts.

In [56], Johnson proposed a variant to the cross-likelihood scheme, in which the projection data set is divided in k subsets. Then, each subset is subtracted from the complete data set. Each subtracted data set is reconstructed and multiplied by $1/(k-1)$ to preserve the counts number in each iteration. For each subtracted data set, the iterations are stopped when the likelihood of the non-included data set is maximized.

Another approach was proposed in [64], where a study of the multiplicative update coefficients of the MLEM algorithm allowed the au-

thors to establish a stopping rule. For each iteration, the update coefficients are stored and histogrammed. The technique is based on the fact that the optimum iteration value (given in a simulation study by the RMS value) is reached always in the same value for the histogrammed coefficients. In a precedent work [65], the authors stated that a value of 0.8 produces images close to the optimal reconstructed image (with ± 5 iterations).

4.2.4 Accelerating Convergence in MLEM

The MLEM algorithm has shown better results than the classical FBP algorithm in quantitative and qualitative terms [3], however its inconvenience is its slow convergence. Different approaches has been created to overcome this problem, like parallelism of the process, improvements in computational memory management, and so on. One technique that improves the speed of convergence and has approached the EM technique to the clinical scenario is the *Ordered Subset Expectation Maximization* algorithm (OSEM) [52]. Instead of working with one set of projections, the algorithm performs several sub-iterations over a smaller subset before beginning with the next one. The results using this technique have shown that the image reconstructed gets closer to the convergence point in less time than the original MLEM algorithm. It results from the fact that for each iteration, a voxel is updated as many times as the number of subsets. Therefore, each voxel is visited more times during one iteration than in the case of using a single set of projections. In other terms, for every subset the image is reconstructed considering the information contained in that subset, then, for the successive subsets new information is added to the reconstructed image. The speed-up of the algorithm is based on the smaller time required to reconstruct an image with less projection data. According to [52], the higher the number of subdivisions the better level of detail it can be obtained. However, they agree that there is a limit of the number of subdivisions. Beyond that limit, the algorithm lacks of sufficient data

to fit the observed data.

Algorithm 4.2.2: OSEM(*Ordered Subsets EM*)

for $K \leftarrow 0$ **to** n-iterations
do for $i \leftarrow 0$ **to** number-of-subsets
do $\begin{cases} \overline{p_d} = \sum_b R_{db}\lambda_d^{<K>}, d = 1, \ldots, M. \forall d \in S_i (S_i \equiv \text{Subset i} \\ \textbf{for } b \leftarrow 1 \textbf{ to } N \\ \quad \textbf{do} \begin{cases} C_b^{<K>} = \sum_{d \in S_i} \frac{p_d R_{db}}{\sum_{b'} \lambda_{b'}^{<K>} R_{db'}} \\ \lambda_b^{<K+1>} = \lambda_b^{<K>} C_b^{<K>} / \sum_{d \in S_i} R_{db} \end{cases} \end{cases}$

Other issue of interest is how to select and how to order the subsets. In [52], the authors remark that the selection of subsets should be done in a balanced way, so that the voxel activity information is also balanced in the subsets. Regarding the order in which the subsets are processed, They suggest that even if the order is arbitrary it is preferable to process subsets which include new information as soon as possible.

Despite the good empirical results presented by OSEM, its major problem has been its lack of proof of convergence and ambiguity in the use of priors [3], also it has been stated that it can lead to limit cycles in the iterative object estimates [50], which posteriorly motivated the creation of the row-action maximum likelihood algorithm (RAMLA) [13], and the subset-dependent relaxation RAMLA (DRAMA) [112].

Recently, an accelerated convergent ordered subset algorithm was presented [50]. It establishes a tradeoff between speed and convergence by using a parameter that updates itself automatically as the iterations proceed. This parameter introduces a linear combination between the fast but non-convergent OSEM algorithm and the slow but convergent COSEM algorithm [73][6]. Basically, at the beginning of the iterations more weighting is given to the OSEM image in order to

[6]Variant of OSEM algorithm for list-mode data.

speed-up the convergence, and then, as the iterations proceed, more weighting is given to the COSEM image to ensure convergence. The major drawback of the algorithm is that the linear combination needs a precalculation of each guess image (i.e. OSEM and COSEM images), which will play against the gained speed-up of the algorithm.

Another approach to accelerate convergence of the algorithm was proposed by Fessler and Hero [27]. The SAGE (Space-Alternating Generalized Expectation Maximization) algorithm consists basically in computing at each iteration new pixel/voxel estimates, which are then used in the current iteration. This differs to the classical MLEM algorithm, in which all the elements of the image need to be visited before new estimates are incorporated in the next iteration. The formulation of the SAGE algorithm was inspired by two concepts. First, application of the optimization transfer principle (see Appendix A.4) (i.e. to provide a surrogate function that makes the maximization of the objective function a tractable problem). Secondly, it has been proved that the convergence rate of an EM algorithm is inversely related to the Fisher information of its complete-data space [27] (see Appendix A.5 for more details).

The SAGE algorithm can be grouped into a family of pixel-based block iterative algorithms. Unlike the OSEM algorithm, where the data is separated in blocks, the pixel-based block iterative techniques separate groups of pixels/voxels. Another technique that falls in this classification is the coordinate ascent technique [28, 100], which has a rapid convergence and its structure favors the incorporation of positivity constraints. In the other hand, its major potential drawback is that of being computationally inefficient if caution is not taken [71].

Another family of image reconstruction are based on gradient-based optimization algorithms, which were introduced in tomographic image reconstruction as an alternative to the EM technique with the main interest of improving convergence (see Appendix A.7).

4.2.5 R-projector and fully-3D reconstruction

For the algebraical methods, the construction of the projection matrix R is important since in this matrix, other correction factors can be included. The construction of the projection matrix has been commonly performed by composing to a base projection matrix, which only takes into account detection probabilities, specific matrices constructed for each type of phenomenon or degradation factor being corrected.

Concerning the image reconstruction, fully 3-D reconstruction can be performed by designing a projection matrix that considers a fully 3-D geometry. Indeed, classical approaches perform data rebinning of 3-D projections into axial planes and then image reconstruction of each plane is performed. The interest of a fully 3-D reconstruction method increases for the task of respiratory, where motions occurs in a 3-D space. As presented in chapter 7 this task is computationally intensive and needs the application of approaches as parallelization of the algorithm.

4.2.6 Discussion

The problem of image reconstruction has been presented. This chapter does not pretend to give the reader a detailed description of the existent algorithms for image reconstruction. But, to present the basics elements of image reconstruction, which can facilitate the reading of the next sections, where some of the motion correction techniques integrates the correction into the step of image reconstruction. Moreover, as it will be discussed in chapter 6, the motion correction proposed in this work is included in the step of image reconstruction as well.

Acceleration techniques have been presented as well. However, for this first stage of experimentation with the proposed motion correction technique, no acceleration was included in order to test the methodology with the original MLEM algorithm. We anticipate however that inclusion of acceleration schemes like ordered subsets is feasible.

From the revision of stopping criteria for the MLEM algorithm, we conclude that such topic is still an open question and needs further development. Therefore, we have preferred an empirical method to stop the iterations based on visual inspection of images.

Chapter 5

Motion Correction in Emission Tomography Imaging

5.1 Introduction

As already stated, the goal of the image reconstruction step is to obtain a visual representation (i.e. image) of a physical quantity from a set of indirect measurements . In ET this physical quantity allows to highlight biochemical process of the body, which can be the result of a disease like cancer. In this case, the reconstructed image is of great importance since it serves to stage the evolution of the cancer and it also provides information about the possible treatments the patient can go through. This way, the success of detection and therapy is strongly bounded to the quality of the reconstructed image.

While in chapter 3, several acquisition process and instrumentation related degradation factors were discussed, this chapter focus on the problem of respiratory motion during the data acquisition step.

The problem of motion during data acquisition is not unique to emission tomography studies. In other imaging modalities the problem

of patient motion (incidental or physiological) during data acquisition also appears. The literature regarding motion correction techniques in imaging modalities like CT and MRI is vast and several examples can be mentioned for CT [94, 98, 39, 80, 10, 51, 58, 124], and for MRI [61, 106, 30, 78, 82]. The physics of the detection system on those modalities has facilitated the incorporation of motion correction in comparison with emission tomography. Indeed, CT, MRI and other related anatomical imaging modalities present better spatial and temporal resolution allowing more exploitation of the available information obtained from those systems.

Furthermore, as it will be mentioned in the next sections, the complexity of the motion correction depends on the organ or region where the motion occurs and the type of motion. This results in motion correction algorithms specifically designed for a given organ and/or motion type. The respiratory motion in emission tomography is our main concern. However, additional material related to motion detection and correction in ET for brain studies is presented for completeness. Further discussion about the applicability of some of these methods to respiratory motion correction is given as well.

In the first part of this chapter, findings on respiratory motion artifacts and its impact to detection, therapy, and planning in lung cancer are presented. Then, most important contributions concerning solutions to this issue are discussed. The final part of the chapter presents the main contribution of this work; a novel motion correction technique based in a motion model plugged in the computation of the projection matrix in the classical MLEM algorithm.

5.2 Impact of respiratory motion in lungs studies

Respiratory motion has been shown to degrade the quality of reconstructed images. This degradation, first hinders the accurate delineation of tumors (i.e. position and volume measurements of the lesion)

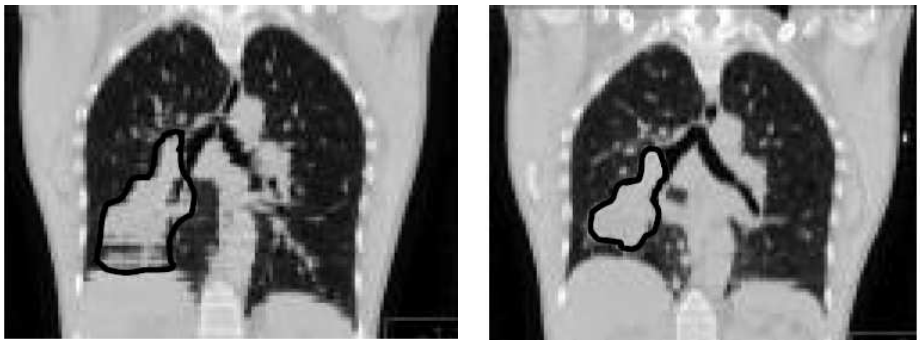

(a) Without motion correction (b) With motion correction

Figure 5.1: Respiratory motion degrades the outlining of lung lesions. Applying a motion correction technique the true volume and shape of the lesion can be recovered. Image source: S.H. Benedict [7].

and so, it degrades the precision to which the zone of the body to be irradiated is delineated (see Fig. 5.1 as an example of motion correction applied in CT imaging). Second, motion during the acquisition process affects the images quantitatively. It has been shown that the standardized uptake value (SUV) [1] can be improved by applying motion correction techniques [11]. With motion, the reduction of the SUV parameter is due to the image blurring on the malignant zone and the overestimation of the lesion's volume, which result in a spread out of the activity concentration [83]. In [11] for instance, the authors found in phantoms experiments an underestimation of the SUV between 30% and 48%. Usually a SUV value greater than 2.5 is considered as an indication of a higher probability for malignancy [75]. Hence, a lung lesion having a SUV close but lower to this value could be a false negative produced by the effects of respiratory motion.

Concerning radiotherapy, respiratory motion affects the estimation of the Planning Target Volume (PTV) (see appendix A.1 for a detailed explanation of this and other related terms). This affects the treatment in three different ways. First, there is an increase of nor-

[1] Ratio between the concentration of injected dose and the patient's weight

mal tissue being irradiated. Second, the effective target dose is limited [26] and third, the interplay between respiratory motion and multileaf collimator motion leads to delivery motion artifacts [7].

In an effort to improve radiotherapy in lung lesions, Seppenwoolde and colleagues [102] studied the 3-D displacements of lung lesions over a set of patients. Their findings highlight several issues to be considered during radiotherapy. For instance, lung lesion displacements are space-dependent. Tumors located at the base of the lungs typically present greater displacements than lesions located at the center or at the apex of the lungs. Besides, greatest motion amplitudes are found in the cranial-caudal direction. Concerning the 3-D trajectory of the displacement, hysteresis was found in half of the patients (i.e., the tumor does not follow the same path at inhalation and expiration phases) and variation of the trajectory between subsequent days of treatment is not likely to occur. Fig. 5.2 shows orthogonal projections of trajectories for twenty-one lesions. It can be noted that lesions not attached to rigid structures and situated at the bottom of the lungs present greatest displacements in the cranial-caudal direction.

Besides diagnosis and therapy, respiratory motion affects image co-registration with other modalities [16]. In [36] and [37] the influence of respiration in the co-registration between PET and CT was studied and appropriate breathing protocols to compensate the effects of respiratory motion were presented. Of seventy five patients, findings of misregistration were found to be space-dependent. Lesions located at the base of the lungs present more significant mismatches than those located at the apex or center of the lungs [37]. Previous results regarding misregistration in thoracic PET emission-transmission were documented by Yu et al. [126]. They found shifts in the X and Y axis with respect to the traverse plane. However, no indications of space dependance is indicated. In [87], Osman and colleagues found that serious mislocalizations in PET/CT may occur when CT is used for either attenuation correction (AC) or image fusion. Over three-hundred

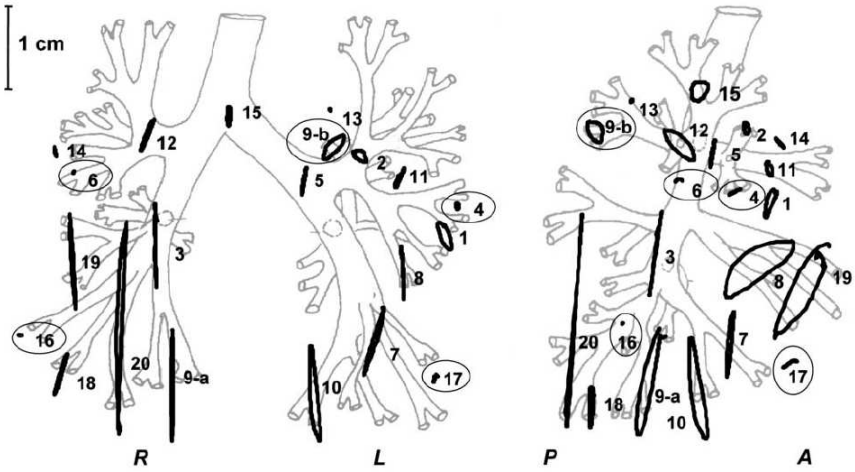

Figure 5.2: Orthogonal projections of trajectories for twenty-one lesions. Right (R), Left (L) , Posterior (P) and Anterior (A) views are presented. Lesions attached to bony structures are circled. Image source: [102].

cases, six cases presented true liver lesions that were mislocalized to the right lung base on PET/CT. In a similar study, Osman and colleagues reported differences between CT-based attenuation correction and germanium-68 (Ge) attenuation correction. Their findings indicate that cold artifacts caused by respiration at the interface of the lungs may be seen in CT-corrected images but not in (68)Ge-corrected images [88].

5.3 Respiratory motion correction techniques

Respiratory motion correction in ET is a difficult task. Some influencing factors are:

- Physiological issues: patient specific breathing patterns, lesion position, lesion type, etc.
- Specific instrumentation and data acquisition protocols: limited

image resolution, acquisition modes (e.g. list mode data), temporal resolution (for list mode data), field of view, etc.

- Image reconstruction issues: system modelling, computed attenuation correction, physics modelling, etc.

Current methods can be classified in four main categories: post-processing, Multiple Acquisition Frame (MAF), sinogram data selection based on detected motion, and sinogram correction.

Next sections describe each category and some results obtained from their application.

5.3.1 Post-processing

Post-processing methods are based on transformations performed either in projection-space or in image-space (often guided by information obtained from anatomical imaging modalities).

Post-processing techniques applied in image space after image reconstruction have been tested, not with the final goal of performing respiratory motion correction but with the objective of improving the image fusion of images acquired with different acquisition protocols (e.g , the fact that in ET the patient breaths during the exam whereas in CT the patient can hold respiration during the shorter acquisition time). This has been signaled as an issue to be solved in order to improve the quality of image fusion [111].

Due to the elastic nature of lungs and the deformation of the thoracic cavity under respiratory motion, non-linear registration techniques have shown to perform better than rigid or affine transformations [79, 17, 18]. On the other hand, non-linear registration techniques do not consider the true effects of motion on the acquired data, that is to say, transformations are found using anatomical and time-averaged biochemical information, whilst physiological changes should be considered as well.

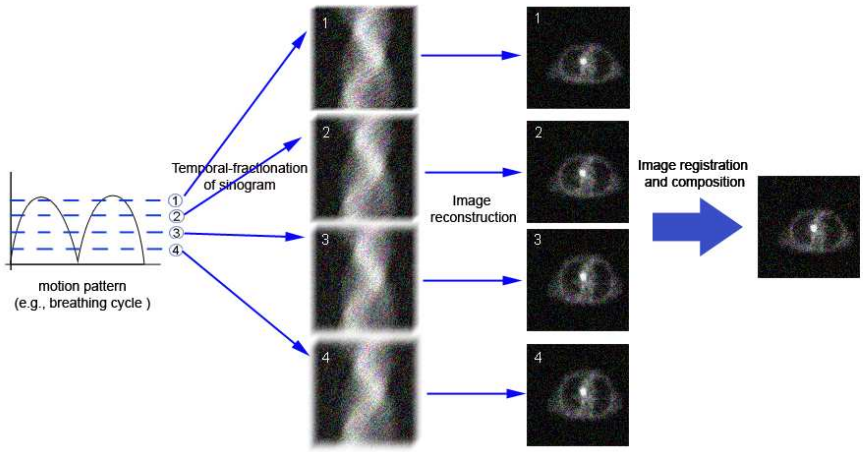

Figure 5.3: Multiple acquisition frame (MAF). The sinogram image is temporally fractionated according to the detected motion. Each fraction of the original sinogram is then reconstructed and the obtained images are registered and fused to form a final motion compensated image.

5.3.2 Multiple Acquisition Frames

The MAF-based methods are more realistic. They consist in regrouping the projections in smaller subsets according to online or offline detected motion (see [6] for an example of this on cardiac motion). Then, the image reconstruction of each subset is performed independently and is followed by realignment of the images to fuse all reconstructions. In online motion detection, an external motion tracking system is used (e.g. [90]), contrary to off-line motion detection, which is performed in an effort to avoid the use of these devices [89].

Picard and colleagues presented in [90] an implementation of a MAF method, in which the motion detection is performed by detecting a set of three luminous landmarks placed on the source (phantom or subject's head) so they can be simultaneously detected by a pair of video cameras mounted on the gantry of the scanner and connected to a frame grabber. From the frame buffer, the centroids of each spot are

then computed and triangulation is applied to them to compute the spatial position of each landmark. Then, assuming a rigid body transformation and knowing the position of the each landmark, it is possible to recover the six parameters describing the rigid transformation (three rotation angles and three translations).

During data acquisition a signal is triggered and sent to the data acquisition system whenever a motion displacement higher than a specified threshold is detected. The system check if a previous frame has a position that corresponds to the current detected position. If so, data is collected on this frame. Otherwise, data is collected in a new frame and the new position is stored in the frame history file along with the current time and frame number. This way, an otherwise single sinogram is temporally-fractionated in several sub-sinograms. For respiratory motion detection, the trigger signal should be related to the phase state of the breathing pattern (see Fig. 5.3).

Since each frame can be visited several times during data acquisition, decay correction must be incorporated. For this, at the end of the scan each frame is corrected by computing the following decay factor

$$\begin{aligned} f_{decay} &= \frac{\sum_{i=1}^{N} \Delta t_i}{\sum_{i=1}^{N} \int_{t_i}^{t_i+\Delta t_i} \exp^{-\ln 2t/T_{1/2} dt}} \\ &= \frac{\ln 2}{T_{1/2}} \frac{\sum_{i=1}^{N} \Delta t_i}{\sum_{i=1}^{N} \exp^{-\ln 2t_i/T_{1/2}} (1 - \exp^{-\ln 2\Delta t_i/T_{1/2}})} \end{aligned} \tag{5.1}$$

where f_{decay} is the decay factor for one particular frame, N is the number of times the frame was visited, t_i and Δt_i are the times and time intervals during which the frame was visited.

The technique was tested on line sources and on the Hoffman phantom. The authors concluded that the video system should send a signal to switch frames whenever a displacement larger to 5 mm is detected. The results obtained show the ability of the technique to compensate for both discrete and continuous motion, provided there exists a good

spatial correlation between the true lesion's motion and the motion of the landmarks, and a sufficient number of frames is available according to the displacement span of the detected motion.

A similar approach was proposed in [89], where a MAF method was tested on phantom and clinical CDET data. The method consists in performing data fractionation on several frames, each of which considers a full acquisition at a faster speed. This allows to have several frames for each rotation. That is to say to have separated projection data from different time intervals but with same angular positions. The basic idea is that of assuming that if motion occurred between frames, differences will appear on the projection data for those frames. These differences are supposed to be caused by motion, which is be detected by means of an original method based on the computation of cross-correlation (CC) among frames.

As an example, consider fractionation of the projection data in three frames, as illustrated in Fig. 5.5(b), where Set 1, 2, and 3 correspond to the frames corresponding to the first, second and third time period fractionation. Let's assume that motion occurred during the second time period with at a rotation of the camera of 120 °. Imagine now the patient remains in that position for the rest of the acquisition. At the end of the data acquisition process, three projection data frames describe coincident events at the same angular positions. To measure the similarity between corresponding partial projection datasets, the cross-correlation presents itself as a good measure, and it is computed as follows

$$c_{k,l}(\alpha,\theta) = \frac{\sum_{x_r}(S_k^\alpha(\theta,x_r) - \hat{S}_k^\alpha(\theta))(S_l^\alpha(\theta,x_r) - \hat{S}_l^\alpha(\theta))}{\sqrt{(}(S_k^\alpha(\theta,x_r) - \hat{S}_k^\alpha(\theta))^2)\sqrt{(}(S_l^\alpha(\theta,x_r) - \hat{S}_l^\alpha(\theta))^2)} \quad (5.2)$$

where $c_{k,l}$ is the cross-correlation between sinograms k and l, at rotation angle α of the camera and LOR at angle θ with respect to the camera (see Fig. 5.4). In Eq. (5.2), sinograms S_k and S_l are centered

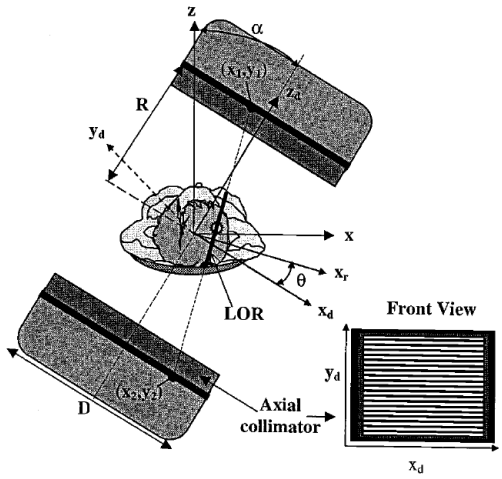

Figure 5.4: Geometry of the detection. Detectors are rotated by an angle α. Coincidence events collected at positions (x_1, y_1) and (x_2, y_2), the resulting LOR is characterized by its position x_r and angle θ relative to the detector reference. Image source [89].

around their mean $\hat{S}_k$ and $\hat{S}_l$ along the axial direction $x_r = (x_1 + x_2)/2$ (see Fig. 5.4).

To facilitate the analysis of the CC values, the authors compute a more synthetic representation of the CC values in the form of a CC curve, which shows the evolution of the partial CC values (Eq. (5.2)) only as a function of the camera angular position α by integrating the partial CC values along θ.

$$C_{k,l}(\alpha) = \min 1, \frac{1}{9} \sum_{\theta=\alpha-4\Delta\alpha}^{\alpha+4\Delta\alpha} \frac{c_{k,l}(\alpha, \theta)}{C_{max}(\alpha)}. \tag{5.3}$$

With $\Delta\alpha$, the angular step of acquisition. Besides, it was empirically found that $4\Delta\alpha$ is the optimal acceptance angle.

This way, at a given rotation angle or angular range, a CC value close to one indicates high agreement between series and so, that no motion occurred during that period of time. On the other hand, lower

CC values are indicatives of inconsistencies between temporal series and thus, they denote presence of motion during that period of time.

For the given example, Fig. 5.5 shows the obtained CC curves. It can be noticed a high CC value between the first and second frame, indicating a high consistency between them. This value decreases around 114°, indicating where the motion occurred between frames one and two. On the other hand, the CC values between frames two and three is low before 114° but then increases, indicating that those frames became consistent after motion. Finally, data from frames one and three are never consistent as indicated by low CC values for all angles.

Once motion has been detected, the data corresponding to the detected motion is eliminated and the pre-motion and post-motion data are rigidly registered into a single final image. The authors state that this last step could be performed in the sinogram space also, by searching the shifts between two partial sinograms that optimize the CC value, to then correct the data accordingly to the found shifts.

The methodology is only applicable when the patient moves from one position to another, which is impracticable for respiratory motion correction (see [59] for another data-driven motion detection method that is applicable in detection of displacements in the axial direction).

The method was tested on phantom data, in which displacements and rotations of spherical sources were performed. Fig. 5.6 shows the results obtained. For patient data, the lack of a ground truth makes difficult the task of validation. In order to validate the method in a clinical scenario, Barakat et al. [89] proposed the introduction of artificial motions in the raw data projections. Although respiratory motion is still present in all cases and it is not being corrected, the method is able to recover for translations added artificially.

In [31], a MAF-based method for correction of head movements in PET imaging considering an optical motion tracking device was developed. The objective of the work was the feasibility study of correcting for head movements in PET using information provided by a Polaris

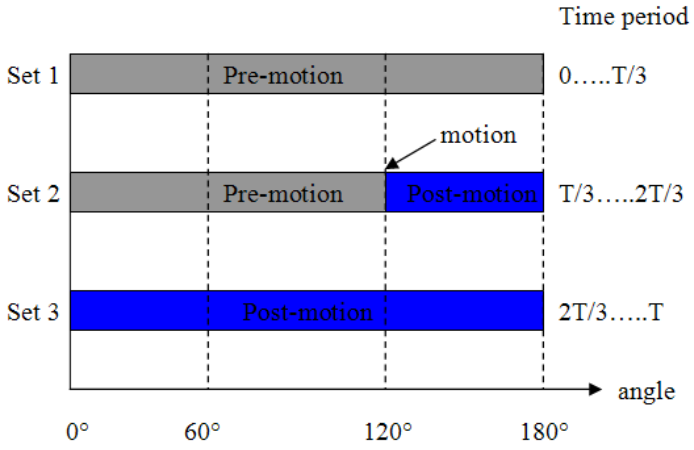

(a) Temporal frame fractionation

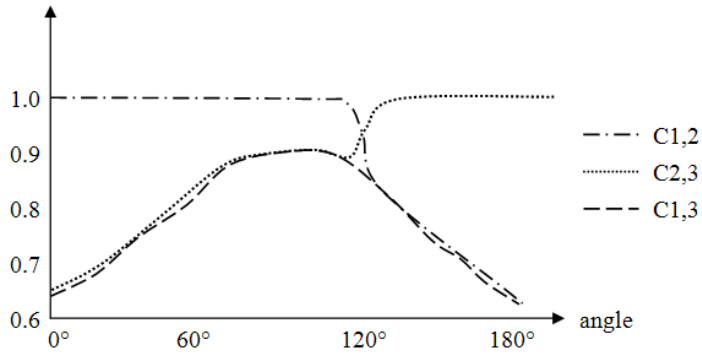

(b) Integrated CC curves

Figure 5.5: Temporal fractionation divides the data in frames with different time periods but with same angular range information (a). Typical CC values among sets (i.e,. C1,2, C2,3 and C1,3) over the whole angular range. It can be noticed that at 120, lower values are found for C1,2, indicating that motion has occurred.

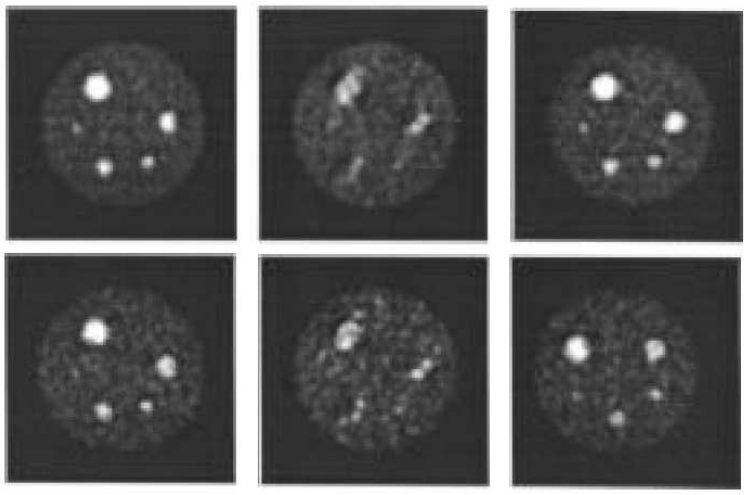

Figure 5.6: Temporal fractionation in phantom data. A set of spherical sources were used to simulate a bulk motion during data acquisition. Motion was simulated as a translation during the second temporal frame (as shown in Fig. 5.5(a)). Superior row and from left to right shows: reference image, without motion correction and after motion correction. Bottom row and from left to right: pre-motion data set, within motion data set and post-motion data set. It can be noticed in the bottom central image the presence of motion in comparison with the bottom left and right, in which no motion has occurred. Image source [89].

optical motion-tracking system. This device (or tracker) stores the position and orientation of rigid targets fitted with infrared-emitting or infrared-reflective markers.

For head tracking a lightweight target composed by four infrared-reflecting marker was constructed and the tracker was mounted on a tripod facing the rear of the PET scanner. In order to relate the axis coordinate systems of both the scanner and the tracker, a calibration methodology was developed, based on a target composed by four reflective markers and an FDG point source. By imaging this point source and capturing the position of the reflective markers (reported by the tracker) it is possible to determine analytically the 3-D position of the point source in scanner coordinates. By repeating this procedure at least three times (or more to increase accuracy) this calibration permits the obtention of the rigid transformation T_c needed to pass from one coordinate system to the other.

Given the position and orientation of the target before and after movement, T_{ref} and T'_{ref} respectively, and the transformation $T'_c = T_c(T_{ref}T'^{-1}_{ref})$, which converts tracker measurements to scanner coordinates for any position of the reference target, it is possible to convert the position and orientation of the head-tracking target H_s (in tracker coordinates) to scanner coordinates H_s as $H_s = T'_c H_p$. Finally, the transformation M describing the motion of the target in scanner coordinates from a reference position and orientation H_s to a new position and orientation H'_s can be obtained as $M = H'_s H_s^{-1}$.

Once the data is acquired in multiples frames, each frame is reconstructed (filtered backprojection reconstruction). Then, each reconstructed image j is transformed to the same position and orientation of the reference frame by applying the transformation M_j^{-1}. Images are then added to form the motion-corrected reconstruction.

The approach presented [31] was further investigated and extended to list-mode data in a PET environment, presented in [113]. The main difference with the methodology presented in [31] is the additional step

of sorting the acquired list mode data into time frames, which are defined interactively with a graphical user interface and taking into account motion information from the optical motion tracking system. Once the list mode data have been sorted in time frames, the methodology previously presented was applied.

According to the authors, this approach presents itself as an intermediate step towards a direct correction of the list mode data on an event-by-event base, which needs, however, a better synchronization between PET data and the information retrieved from the optical motion tracking device.

These approaches, however, present the inconvenient that the signal-to-noise ratio decreases for images reconstructed from smaller subsets of projections, leading to intermediate images suffering from heavy noise. Other drawbacks are associated to instrumentation issues. For instance, the temporal-fractionation needs special acquisition protocols (frame switching) and the number of available frames can be a limitation when the displacement range is considerably larger with respect to the spatial resolution of the system. In other words, the higher the displacement the more frames are required to detect inter-frame motion with a certain degree of precision. For the CC-based approach, this is not an issue of great importance since the method was designed mostly for bulk motion correction, and thus, a small number of frames are enough to detect for motions like those produced when the patient grows uncomfortable or when the patient tilts the head in head studies. However, when a larger number of frames is required, the main constraint comes from the speed capacities of the gantry, which can limit the application of this methodology in studies where repetitive motions are present or when continuous motion must be detected. Besides, faster acquisitions imply lower signal-to-noise ratios, which makes posterior signal processing difficult.

5.3.3 Sinogram data selection

Sinogram data selection based on motion detection, also known as gating, has been used to compensate for motion correction in ET. Respiratory gating as its name indicates, was designed for respiratory motion correction. The quasi-regular periodicity of the breathing pattern and its short time period in comparison with the total acquisition time, allow to collect enough data at a fairly same phase of the breathing cycle, or equivalently, to collect enough data of a lesion at a fairly same position. To achieve this task, the method considers synchronization of the breathing cycle with the data acquisition process by using a respiratory motion tracking device.

In [83], Nehmeh and colleagues performed gating-based respiratory motion correction on PET data. The motion tracking device corresponds to the Real-Time Position Management (RPM)[2], and is composed by an infrared video camera system that tracks the position of two reflective markers rigidly mounted on a lightweight plastic block situated on the patient's abdomen. This way, the infrared video camera follows at every instant the position of the markers, position that is supposed to correlate with the patient's breathing cycle. A prototype breathing pattern is generated through a training session. On this prototype pattern, the user selects the phase or amplitude point where a trigger signal will be generated if the breathing pattern of the patient is regular with respect to the prototype pattern.

The PET data is acquired in synchronization with the breathing cycle. The number and duration of each bin is selected before data acquisition. Since the duration of each bin is in the range 300-500 ms, the effects of motion on projection data within each bin are negligible, allowing motion compensation on images reconstructed from each bin.

Fig. 5.7 illustrates the basis of the method.

Qualitative and quantitative results are very promising. Fig. 5.8

[2]Varian Medical Systems, Palo Alto, CA.

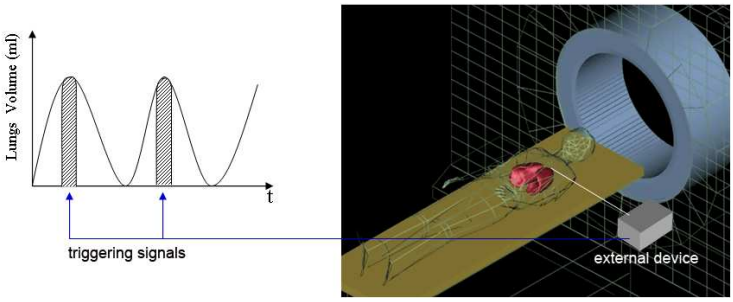

Figure 5.7: Respiratory gating. An external device is used to detect respiratory motion, its output triggers the data acquisition and only data representing nearly the same state of respiration is used for posterior image reconstruction (i.e. gray zone in plot).

presents both a comparison between lesion volumes for gated and non-gated images and quantitative results in terms of SUV values for gated and non-gated images.

In respiratory gating, the need of extra devices to perform respiratory motion detection is a limiting factor [84]. Motivated by this fact, Nehmeh and colleagues developed which is called Respiratory Correlated Dynamic PET (RCDPET) [84]. This method differs from that of respiratory gating (RGPET) by the way respiratory motion is detected. While in respiratory gating, the motion detection is performed online, RCDPET performs offline detection. To do this, RCDPET is based on the tracking of an external FDG source point situated on the patient's abdomen. This source point is attached to a low-density plastic rod, with the other end attached to a Styrofoam[3] block. The block is then secured to the abdomen of the patient.

As the patient breathes, the source point will move. The main assumption is that the motion of the source point correlates with the patient's breathing cycle. To improve this correlation, the plastic rod is extended or contracted to situate the source point at an approximative

[3]The Dow Chemical Co.

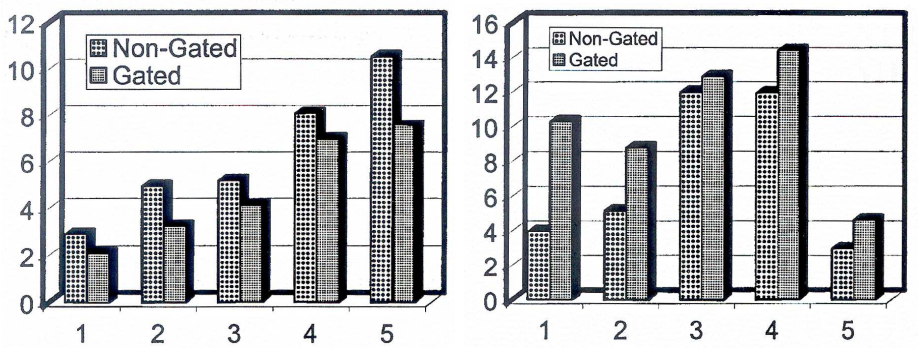

(a) (b)

Figure 5.8: Volume changes between gated and non-gated images in five patients (a). A noticeable volume reduction is observed when gating is used. Quantitative results indicate that larger SUV values are found in gated reconstructed images in comparison with its non-gated counterpart (b), which indicates larger concentrations over the true lesion volume. Image source: [83]

position of the lesion. Fig. 5.9 illustrates the basic concept.

PET data was acquired at the maximum temporal resolution (1 second). From this, two hundred 1-s frames were acquired using the standard dynamic scanning mode provided by the PET scanner software. All two-hundred frames were reconstructed and on one image a ROI including the source point was drawn. This ROI was repeated on every image and detection of the source point was performed. The images containing the source point inside the ROI were selected and the frames corresponding to the selected times were added and reconstructed.

Results in phantom and patient data show the capacity of RCDPET to compensate for the effects produced by respiratory motion. When comparing RCDPET with RGPET, results indicate that RCDPET performs as well as RGPET with a 10% of agreement for both activity quantification and noise levels.

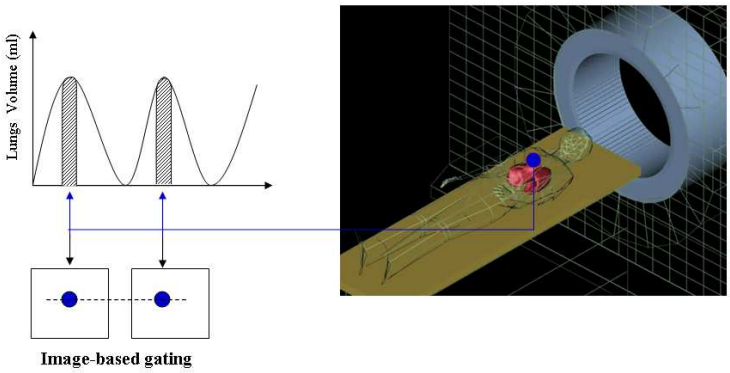

Figure 5.9: Respiratory Correlated Dynamic PET (RCDPET). Respiratory motion detection is performed by offline tracking of a FDG source point situated on the patient's abdomen. Detection of the source point in the image space allow to select the projection data corresponding to the same motion phase or amplitude.

Figure 5.10: Motion detection is performed in RCDPET by tracking a source point situated on the patient's thorax. By correlating the motion of the source point with the patient's breathing cycle, an estimation of the patient's breathing pattern can be created. In the picture, the source point is located at the end of the low-density rod, which is attached to a styrofoam block.

Gating techniques have shown improvements in reducing the blurring effect caused by motion, contributing to a better quantification of lesions. However, they require extra hardware or specific data acquisition modes and they discard data for the image reconstruction. For RCDPET, the extra hardware constraint does not apply. However, the methodology requires extensive image reconstructions to perform motion detection and considerably more computer memory than RGPET. Furthermore, it has been shown that using tracking devices based on external information (e.g. elasticized belt, skin markers, etc.) may not always correlate with lung tumor location [8, 120], which has motivated the use of more complex tracking devices systems (e.g. implanted radio-opaque markers).

Inspired by the problem related to extra hardware needed to perform gating, in [122] an approach based on a posteriori respiratory motion gating of dynamic PET images was presented, which does not need an external signal to perform the gating of data. In this method, a Fourier analysis of the acquired FDG PET dynamic data allows to estimate the respiratory frequency, from which projection data can be retrospectively selected (a posteriori gating) and motion correction can be performed without the need of external devices. The basic principle of the method consists in assuming that although the amplitude of the motion can vary inside an organ, the frequency of the periodic motion is the same. From this hypothesis, the activity $A(x, y, z, t)$ is modelled as the sum of a constant intensity and of a cyclic one

$$\begin{aligned} A(x, y, z, t) &= a(x, y, z) + a_1(x, y, z)\cos(w_0 t - \phi(x, y, z)) \\ &= a(x, y, z) + b(x, y, z)\cos(w_0 t) + c(x, y, z) sin(w_0 t) \end{aligned}$$

where $a(x, y, z)$ is the intensity constant component, $a_1(x, y, z)$ is the intensity amplitude and $\phi(x, y, z)$ is the phase of the motion in voxel (x, y, z).

To estimate the frequency parameter, w_0, a power spectrum, $S(f)$, of the time activity curve, $s(t)$ is computed. Under the assumption

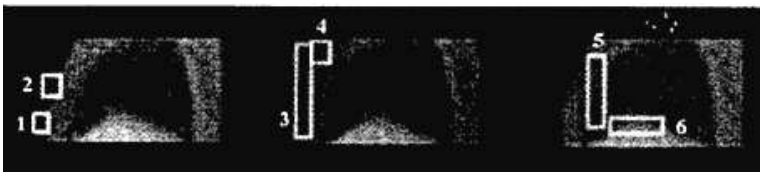

Figure 5.11: Sagittal slice of thorax phantom including six ROI's considered to obtain time activity curves. Image source [122].

that $s(t)$ fairly describes the periodicity of the respiratory motion, $S(f)$ should have a sharp peak at the frequency w_0. This condition is dependent of the region-of-interest (ROI) on which the time activity curve is analyzed. Fig. 5.11 shows the ROI's chosen by the authors, which would allow to describe the periodicity of the respiratory motion. It should be remarked that the location selection of the ROI's is critical: it has to be placed across an organ interface, such that during part of the motion the organ is inside the ROI and during the other part the organ is outside. This property allows to capture the periodical activity changes inside the ROI produced by respiratory motion. Which in turn, by Fourier analysis of these time activity curves, allows the estimation of the frequency of these changes modelled by the parameter w_0.

Concerning the temporal frame resolution needed to produce the time activity curves without increasing excessively the signal-to-noise ratio. The authors have concluded from simulated data experiments that a good tradeoff between temporal resolution and noise level is a time duration greater than 0.45 seconds. However, they claim that from 0.15 seconds, motion correction is feasible with the proposed method.

As it has been mentioned, respiratory gating reduces the counts used for image reconstruction, which, as the case of multiple acquisition frames, produces projection subsets with lower count statistics, and consequently increasing noise on reconstructed images. In [121], PET simulations studies were carried out to evaluate the effects of reduced

count statistics in reconstructed respiratory gated images. Results from their experiments have shown that a minimum of $6e+6$ to $8e+6$ events per frame, in each dynamic bin is necessary in order to profit from the benefits of respiratory gating.

5.3.4 Sinogram correction

More interesting are the approaches based on sinogram correction. These methodologies act directly on the projection data by repositioning the lines-of-response (LOR) when the motion is known [97, 114].

In [114], Thielemans and colleagues present a motion scheme for rigid body motion in PET if the movement is known. For their experiments, Thielemans and colleagues track motion using a Polaris optical motion tracking device, which tracks the motion of a plate with four reflectors using infrared radiation. This plate is attached to a neoprene cap fitting the patient's head.

The motion correction methodology considers two stages. A first step of binning LOR-repositioned events into sinograms and secondly, a step of image reconstruction. For each event in the list mode data, the LOR is repositioned following the rigid transformation given by the Polaris device. The motion correction procedure of binning each list mode event into a sinogram bin consists in a linear procedure. The correction and combination can be conceptually defined as:

$$s_b = \frac{1}{N} \sum_t M^t s_b^t \tag{5.4}$$

where s_b^t stands for the projection data acquired during time interval t for voxel b, M^t is a matrix of rigid transformations (assumed to be known) for time interval t, N is the number of very short time frames, and s_b is the resulting accumulated projection data for voxel b.

Another issue of concern presented by the same authors [114] is the possible artifacts caused by the rigid transformations. These are due to the fact that the transformations can lead to LORs exiting the field of

view (FOV) and so, to LORs generating "holes" in the sinogram space (i.e. parts of the sinogram are completely missing or have too low values because they are partially filled during the acquisition). Therefore, the artifacts are proportional to the amount of motion and are more prone to appear at the end planes than at the center. Compensation of these effects is carried out in the form of weighting schemes.

After binning of the list mode data into a motion corrected sinogram, the method considers computation of scale factors

$$d_b = \frac{1}{N} \sum_t d_b^t \tag{5.5}$$

with $d_b^t = 0$ if the binned event b during time t was out of the field of view, $d_b^t = 1$ if it was completely inside the field of view, or equal to a value between 0 and 1 for bins at the border of these two regions.

The data is then divided by the scale factors, and scatter and attenuation correction are performed as usual.

A similar approach is presented in [97], where motion correction is performed on PET data. A known spatial transformation L rules the rotations and translations of LORs. This time however, no histogramming of the list mode data is necessary and the motion correction methodology has been formulated for both, histogram mode and list-mode data sinograms (see Fig. 5.12).

For histogram mode data, motion correction on LOR's is performed by means of modifying each term of the projection matrix of the MLEM algorithm, according to the motion transformation L, describing rotations and translations of LOR's. Each motion compensated system matrix term m_{ij} takes into account the probability of detection that an event generated by voxel j is finally binned into LOR i. For this, it must be considered the contributions from any LOR l that could have received events, which in the absence of motion would have been detected by LOR i. Under this consideration, the probability term m_{ij} can be computed as a average sum of partial probabilities, as follows

$$m_{ij} = \sum_t w_l^t g_{lj}^t \frac{\Delta T_t}{T}, \tag{5.6}$$

where $l = L^{-1}(i)$, t is the index of time interval of duration ΔT_t in which the motion does not move, g_{lj} stands for the probability of detection between voxel j and LOR l. T is the total time and weights w_l^t are additional attenuation and normalization correction weights.

For the case of list-mode data, since the events are stored one by one, the summation is no required. Indeed, the interaction between the LOR l and voxel j at time t denoted by $g_j^t(l)$ is given by the interaction between the transformed LOR $L_t(l)$ and voxel j at time 0, i.e. $g_j^t(l) = g_j^0(L_t(l))$.

Rhamin and colleagues remarked that interpolation issues do not exist for list-mode data when the LORs are defined as pair of coordinates (this of course, is implementation dependent) which aims at obtaining a more accurate motion correction. Artifacts due to LORs escaping the FOV and other correction factors (i.e. attenuation, detector normalization, etc.) are considered as well in the form of weighting schemes.

When comparing with the method in [114], one can see that both approaches perform LORs repositioning to correct for motion. However, each method acts differently in the way this repositioning is taken into account in the image reconstruction step. Indeed, in [114], LORs repositioning is performed to generate a motion corrected histogrammed sinogram, which is used posteriorly as input of an image reconstruction algorithm. Differently, as described before, the method in [97] performs motion correction simultaneously within the image reconstruction step. The link between these two steps is based on the projection matrix, which as it was discussed in chapter 4, relates emission elements (whose spatial activity we want to recover) and LORs. Each term of the projection matrix establishes the probability that an emission from a certain voxel is detected by a given detector tube, which is commonly

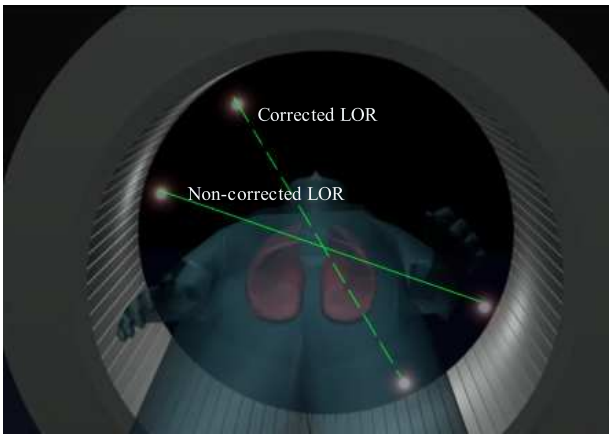

Figure 5.12: Sinogram correction. A given LOR is rigidly transformed and its new position (dashed line) is considered either when forming a motion corrected sinogram (this method requires histogramming of list mode data) or in the computation of the projection matrix (image reconstruction is performed simultaneously).

calculated considering spatial considerations (see [105, 104, 73] for examples). This way, one can reconstruct the object as if it had not moved during the data acquisition.

Preliminary results on phantom data (point and line sources) show the effectiveness of the proposed methods in correcting translational and rotational motions. However, further studies are needed in order to validate such methodologies in more realistic cases.

In [32], a feasibility study of a LOR rebinning method was assessed in list mode data of a Hoffman brain phantom, in which multiple six degree-of-freedom movements were applied.

To track motion, the Polaris optical tracking motion device was used to recover the translational and rotational parameters, in the form of a transformation matrix M, describing the position of the brain in the scanner coordinates system.

Given the two detectors coordinates involved in a coincidence detection, $d_a = [x_a, y_a, z_a]$ and $d_b = [x_b, y_b, z_b]$, motion compensation is

performed by applying the inverse motion transformation of the object to yield the transformed coordinates $d'_a = M^{-1}d_a$ and $d'_b = M^{-1}d_b$. Similarly to the approach presented in [114], transformation of LOR's in this way can produce LOR's falling in positions that are not valid. To deal with this problem, the extrapolation of the line connecting d'_a and d'_b is performed to find the intersection coordinates with the crystal ring.

These approaches do not need extra devices or special acquisition protocols (provided the motion is known or an estimation of it can be achieved). However, they require to deal with motion-corrected LORs that may fall in non-valid positions, which is commonly solved through interpolation schemes (e.g. nearest neighbor), decreasing their practical interest. Moreover, since they implicitly assume that a line is transformed into a line, they are only applicable to motions following this constraint, which is less suitable for respiratory motion correction.

The rigid motion constraint was further investigated by Lamare and colleagues in [67], where affine transformation of list mode for respiratory motion correction in PET was performed. On simulated data the affine transformations parameters are retrieved from affine registrations between images at seven different states of breathing and the reference image. The registration process, based on the maximization of the normalized mutual information was applied for the lungs, heart, and diaphragm regions. The hypothesis was to study the effect of considering a single transformation to describe the deformations due to respiration in different organs. To assess the quality of the registration step the distance between surfaces describing each organ was measured.

As mentioned, the first concern of the authors was to evaluate the impact of using a single affine transformation of the lungs to describe the deformations in other organs due to respiration. From their experiments, it was concluded that a single set of affine parameters considerably improve the lungs and heart regions, whereas the same set of parameters is not able to deal with the deformations of organs situated

below the diaphragm.

For motion correction in list mode, the affine transformation of the lungs is applied to each pair of detected photons with coordinates $p_a = [x_a, y_a, z_a]$, $p_b = [x_b, y_b, z_b]$ given by the emission tomography simulator GATE [4]. The motion corrected events are then reconstructed with the One-pass list mode EM (OPL-EM) algorithm [95]. Preliminary results on simulated data, demonstrate the improvements of motion compensation in list-mode data, by application of affine transformation. The authors consider the need of dealing with transformations having more degrees-of-freedom in order to take into account the deformations encountered at the bottom of the lungs.

5.3.5 FBP-based

In [24], Crawford and colleagues developed a filtered backprojection algorithm that accounts for motion correction. The main assumption follows the idea proposed in [4], where respiratory motion artifact reduction for MRI is performed. The basis of both methods is the assumption that respiratory motion causes a time-varying magnification and displacement in the anterior-posterior and lateral directions (see Fig. 5.13). Formally, the parametric motion model considers that given the cross section to be reconstructed $f(x, y)$, the time-varying cross section $f'(x, y)$ is :

$$f'(x, y) = f(\alpha_x + \beta_x x, \alpha_y - \beta_y y), \tag{5.7}$$

with

$$\beta_x = m_x^{-1}, \quad \beta_y = m_y^{-1}, \quad \alpha_x = x_p(1 - \beta_x), \quad \alpha_y = y_p(1 - \beta_y).$$

Incorporating this model in the classical filtered backprojection algorithm allows to take into account acquisitions taken from a time-varying magnified and shifted object. After some algebraical manipu-

[4] www.opengatecollaboration.org/

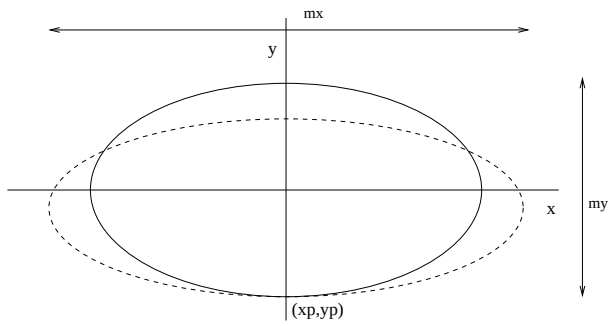

Figure 5.13: Respiration is modelled by a time-varying magnification. Solid and dashed lines represent two states of magnification. The point (x_p, y_p) is the fulcrum and m_x and m_y are the magnification factors.

lation (see [24] for more details) one can obtain an expression for $f(x, y)$ as follow:

$$\begin{aligned} f(x,y) &= \int_0^{\pi}\int_{-\infty}^{\infty} FT_{2D}\left(\frac{w\cos\theta}{\beta_x}, \frac{w\sin\theta}{\beta_y}\right)\frac{|w|g(\theta)}{\beta_x\beta_y} \\ &\quad \times \exp\left[j2\pi w\left(\frac{x}{\beta_x}\cos\theta + \frac{y}{\beta_y}\sin\theta\right)\right] dwd\theta \end{aligned}$$

where

$$g(\theta) = \left|1 + \frac{\sin 2\theta}{2}\left(\frac{\beta_x'}{\beta_x} - \frac{\beta_y'}{\beta_y}\right)\right| \tag{5.8}$$

and where β_x' and β_y' are the derivatives of β_x and β_y with respect to θ, respectively and $FT_{2D}(\cdot)$ is the 2-D Fourier transform of $f(\cdot)$.

Although fast and relatively easy to implement, the oversimplification of the motion model results in lack of robustness. In other words, the time-varying parametric motion model is not accurate enough to describe the deformations produced throughout the thorax, which provokes a strong dependency between lesion position and motion correction accuracy.

In [76], Lu and Mackie presented a continuation of the work of Crawford et al. The motion model is similar to that used in [24] but this time two or more internal or external landmarks are used to detect and estimate respiratory motion, provided these landmarks can be

identified in the sinogram image. Motion estimation relies on the hypothesis that motion generates a non-sinusoidal curve in the sinogram image. This way, variations on sinusoidal patterns allow to estimate displacements of the nodal points.

A motion-encoded sinogram is first obtained by acquiring the projection data with landmarks whose traces are visible in the projection space. This requires higher contrast of the markers with respect to their neighboring points. The traces are then used to track patient motion in the following way.

Assume three nodal points (x_i, y_i), $i = 1, 2, \ldots$ associated with the patient. Assume their traces $p_i(\theta)$ for every gantry angle θ, can be recognized in sinogram space. If no motion occurs $p_i(\theta)$ will be a perfect sinusoidal curve given by

$$p_i(\theta) = x_i \cos(\theta) + y_i \sin(\theta) \tag{5.9}$$

If motion occurs, then the curves generated by $p_i(\theta)$ deviate from sinusoidal curves. Thus, under the considered motion model, the new traces $p'_i(\theta)$ after motion are be given by

$$p'_i(\theta') = [\sigma_x(\theta')(x_i - x_0)] \cos(\theta') + [\sigma_y(\theta')(y_i - y_0)] \sin(\theta') \tag{5.10}$$

where $\sigma_x(\theta')$ and $\sigma_y(\theta')$ the functions describing the time-dependent scaling, (x_0, y_0) the fulcrum point, and (x_i, y_i) the position of marker i.

Therefore, the problem consists in finding for $\sigma_x(\theta')$ and $\sigma_y(\theta')$. This can be performed by applying a first order approximation to Eq. (5.10) and fitting this equation to the obtained sinusoidal approximation. This provides with a set of equations from where the following expressions for $\sigma_x(\theta')$ and $\sigma_y(\theta')$ can be found.

$$\sigma_x(\theta) = \frac{\langle y'^*_2 \rangle p^*_1(\theta') - \langle y'^*_1 \rangle p^*_2(\theta')}{(\langle x'^*_1 \rangle \langle y'^*_2 \rangle - \langle x'^*_2 \rangle \langle y'^*_1 \rangle) \cos(\theta')} \tag{5.11}$$

$$\sigma_y(\theta) = \frac{\langle x_1'^* \rangle p_2^*(\theta') - \langle x_2'^* \rangle p_1^*(\theta')}{(\langle x_1'^* \rangle \langle y_2'^* \rangle - \langle x_2'^* \rangle \langle y_1'^* \rangle) \sin(\theta')} \tag{5.12}$$

where $\langle x_i'^* \rangle$, $\langle y_i'^* \rangle$ are the expected values for $x_i^* = x_i - x_0$, (i=1,2,...).

Once the time-dependent scaling functions $\sigma_x(\theta')$ and $\sigma_y(\theta')$ have been estimated, a motion corrected sinogram, $f(p, \theta)$ can be found as

$$f(p, \theta) = f'(p', \theta')/k(\theta') \tag{5.13}$$

with $k(\theta') = [(\sigma_x(\theta') \cos(\theta'))^2 + (\sigma_y(\theta') \sin(\theta'))^2]^{1/2}$.

The authors state that this methodology can be applied not only to CT studies but also in ET. This is questionable since in ET the required longer acquisition times results in a sort of averaged sinogram image and thus, in a temporal-averaged sinusoidal curve in the sinogram space, which breaks the main hypothesis.

5.4 Discussion

The motion correction methods described in this chapter present different approaches to compensate for the effects produced by motion during an emission tomography study. As it might be noticed, the two major factors influencing the conception of a motion correction methodology are the motion information and how it is obtained and used, and the underlying instrumentation characteristics.

Direct application of all of these methods to respiratory motion is not always possible, and in some cases adaptation would be needed. Among the methods best adapted to respiratory motion, one finds that gating-based and MAF-based have had success and a more widespread application. Up to this moment, gating-based and, maybe with lesser magnitude, MAF-based methods used in conjunction with external motion tracking devices (Polaris optical devices, Varian RPM, pneumatic-bellows based systems, etc) represent the best approach or

gold standard against which other motion correction techniques are generally tested.

Part II

New model-based respiratory motion correction for emission tomography

Chapter 6

Model-based respiratory motion correction

6.1 Method Description

Each one of the motion correction methodologies discussed in the previous chapter present a different approach to solve the problem of patient motion. Moreover, as it was discussed, not all methods fit well into the task of respiratory motion correction. Certainly it is not easy to evaluate which method is better, because in practice there exist other factors to take into account like current data acquisition instrumentation, access to external devices which supply information about motion, etc.

In this work, a motion correction methodology was developed without having access to external devices to be used during data acquisition nor modifying the data acquisition protocols. To address this limitation, we propose to approximate the patient's respiratory motion by a model of respiration motion. Moreover, we plug directly this model into the image reconstruction step to compensate for motion effects. This hypothesis follow the works of [76] and [97]. However, contrary to [76], the method do not consider an external device to detect and estimate motion. This consideration is twofold: first, the method could be

used at institutions not having the means to access such devices and secondly, the method could be used in data sets acquired previously where no motion information was recorded at the moment of the data acquisition.

In this study, motion correction is incorporated into the MLEM algorithm [104] through the projection matrix R, which as it was already mentioned, describes the relationship between emissions elements (i.e voxels) and detection elements (i.e. detector tubes). The fact of incorporating motion information into the projection matrix is convenient since mostly all corrections factors can be added to this matrix, providing an efficient way to group all corrections factors into a single matrix. Besides, it facilitates the implementation.

In the static case, when no motion occurs during the data acquisition period, each emission element will contribute to a given set of detector tubes. In the presence of motion, it is more likely that the number of photons detected by each detector tube will change (even to the point in which some tubes would not receive any contribution from a given emission element). Considering this, one has to estimate the motion corrected contribution R^C_{db} of a moving voxel b to every detector tube d.

To describe the motion each voxel undergoes, let us first consider a continuous motion modeled by the spatio-temporal transformations $\varphi : \mathbb{R}_+ \times \mathbb{R}^3 \mapsto \mathbb{R}^3$, where $\varphi(t, m) = \varphi_t(m)$ denotes the position of a point $m = (x, y, z)$ at time t. The motion is observed from time $t = 0$ to $t = T$. Since we are dealing with a discrete approach of image reconstruction this motion is then discretized in a set of N spatial transformations $\varphi : \mathbb{N} \times \mathbb{R}^3 \mapsto \mathbb{R}^3$, where $\varphi(i, b) = \varphi_i(b)$ describes the position of voxel b at time i ($i = 0 \ldots N - 1$), and φ_i being valid from $t = t_i$ to $t = t_{i+1}$.

The discrete transformations φ_i allow us to construct R^C_{db} as the weighted sum of partial contributions R^i_{db} of deformed voxels $\varphi_i(b)$ to d, as follows:

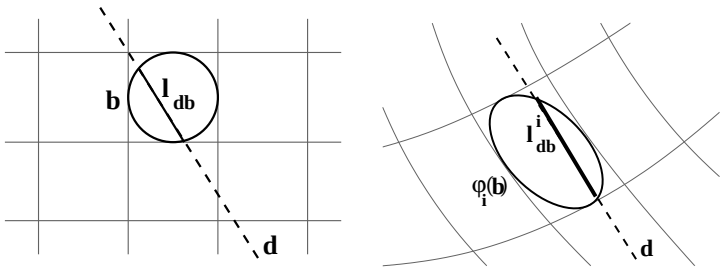

(a) (b)

Figure 6.1: The contribution of an emission element b to a detector tube d, represented by a dotted line, is defined by the intersection (continuous line) of (a) a sphere with a line (static case) or (b) an ellipsoid (a deformed sphere) with a line (dynamic case).

$$R^C_{db} = \sum_i w_i R^i_{db}. \tag{6.1}$$

The weights $w_i = (t_{i+1} - t_i)/T$ allow to take into account the kinetic of the motion: $w_i T$ represents the duration where φ_t can be effectively approximated by φ_i.

6.2 Computation of system matrix terms

The voxels contributing to a detector tube d are assumed to intersect a 3-D line. Let's denote by l_{db} the length of the intersection of this line with the emission element b. We thus define the contribution of b to d by

$$\text{static: } R_{db} = \frac{l_{db}}{\sum_{d'} l_{d'b}} \qquad \text{dynamic: } R^i_{db} = \frac{l^i_{db}}{\sum_{d'} l^i_{d'b}}. \tag{6.2}$$

In the static case, the emissions elements are modelled as spheres inscribed in voxels, which facilitates the calculation of Eq. (6.2) (see Fig. 6.1a). The summation in each denominator of Eq. (6.2) acts as a normalization term.

6.3 Incorporating voxel deformations

If no deformations can be assumed for emission elements b during their motion, we could still have used the intersection of a line with a sphere for the computation of the contribution R^i_{db}. However, this would not be realistic. Indeed, it has been shown that the displacements in the thorax present a non-linear and a non-homogeneous behavior [102, 123]. Thus, we have to consider also the deformations of b. When under motion, the emission element b will deform into $\varphi_i(b), i = 0 \dots N-1$. As a first order approximation, a deformed sphere is an ellipsoid. The contribution of b at state i to d, *i.e.* $\varphi_i(b)$, is then similarly defined as the length intersection of the line d with this ellipsoid (see Fig. 6.1b) (see Appendix A.8).

The study of the jacobian matrix of φ_i, $\nabla\varphi_i$, allows to estimate the ellipsoid.

$$\nabla\varphi_i = \begin{pmatrix} \frac{\partial\varphi_{i,x}}{\partial x} & \frac{\partial\varphi_{i,x}}{\partial y} & \frac{\partial\varphi_{i,x}}{\partial z} \\ \frac{\partial\varphi_{i,y}}{\partial x} & \frac{\partial\varphi_{i,y}}{\partial y} & \frac{\partial\varphi_{i,y}}{\partial z} \\ \frac{\partial\varphi_{i,z}}{\partial x} & \frac{\partial\varphi_{i,z}}{\partial y} & \frac{\partial\varphi_{i,z}}{\partial z} \end{pmatrix} \tag{6.3}$$

where the following notations are used for sake of simplicity

$$\varphi_i(b) = (\varphi_{i,x}(b), \varphi_{i,y}(b), \varphi_{i,z}(b)), \tag{6.4}$$

Let's be $U_i(x, y, z)$ the displacement vector field (DVF) having the information of how an emission element with coordinates (x, y, z) moved in space to the position (x^p, y^p, z^p). The relation between the DVF $U_i(x, y, z)$ and $\varphi_i(x, y, z)$ is thus:

$$\left.\begin{aligned} x^p &= x + U_{i,x}(x, y, z) = \varphi_{i,x}(x, y, z) \\ y^p &= y + U_{i,y}(x, y, z) = \varphi_{i,y}(x, y, z) \\ z^p &= z + U_{i,z}(x, y, z) = \varphi_{i,z}(x, y, z) \end{aligned}\right\} \varphi_i(x, y, z) \tag{6.5}$$

Since $\nabla\varphi_i = Id + \nabla U_i(x, y, z)$ with Id the identity matrix, equation (6.3) can be written as:

Figure 6.2: Jacobian map of a DVF obtained after non-rigid registration of two MRI images of the same volunteer taken at expiration (left) and inspiration (center). Expansion in the lungs are clearly visible with values of $|\nabla\varphi| > 1$.

$$\nabla\varphi_i = \begin{pmatrix} 1+\frac{\partial U_{i,x}}{\partial x} & \frac{\partial U_{i,x}}{\partial y} & \frac{\partial U_{i,x}}{\partial z} \\ \frac{\partial U_{i,y}}{\partial x} & 1+\frac{\partial\ U_{i,y}}{\partial y} & \frac{\partial U_{i,y}}{\partial z} \\ \frac{\partial U_{i,z}}{\partial x} & \frac{\partial U_{i,z}}{\partial y} & 1+\frac{\partial U_{i,z}}{\partial z} \end{pmatrix} \tag{6.6}$$

Eq. (6.6) is presented merely for implementational issues. But it is worth to present it since in practice it is more likely to obtain $U_i(b)$ than $\varphi_i(b)$.

The value of the determinant of $\nabla\varphi_i$ (also known as jacobian of φ_i) describes if the emission element suffers an expansion ($|\nabla\varphi_i| > 1$), a contraction ($|\nabla\varphi_i| < 1$) or if it preserves its volume ($|\nabla\varphi_i| = 1$) [96](see Fig. 6.2). Moreover, it is possible to calculate in what direction and magnitude the emission element will either expand or contract.

Let's consider the singular value decomposition (SVD) of the matrix $\nabla\varphi_i$, that is $\nabla\varphi_i = \mathbf{U}\mathbf{\Sigma}\mathbf{V}^T$, where $\mathbf{U}$ and $\mathbf{V}$ are square and orthogonal matrices and $\mathbf{\Sigma} = diag(\delta_1, \delta_2, \delta_3)$, with $\delta_j, j = 1, 2, 3$ the singular values of $\nabla\varphi_i$.

It turns out that the columns of $\mathbf{U}$ are the eigenvectors of $\nabla\varphi_i{\nabla\varphi_i}^T$, which also give the preferred local deformation directions, while the δ_j are related to the magnitude of the deformations in the direction of the eigenvectors.

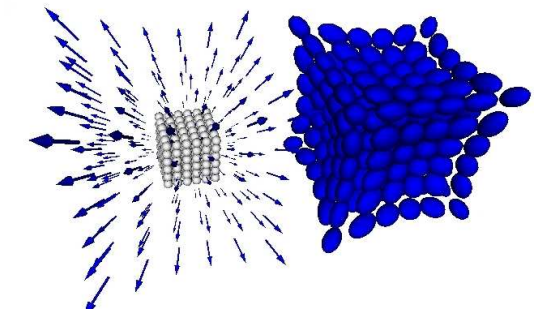

Figure 6.3: Testing the deformation of a set of sphere-shape-modelled emission elements following a pre-built DVF. Left: Original and displacement vector field. Right: Emission elements after transformation.

Consider now the center c_b of an emission element b; the study of $\nabla\varphi_i(c_b)$ results in these directions and magnitudes. If b is supposed to be spherical, then, by applying this simple deformation model to a sphere, it turns out that $\varphi_i(b)$ can be considered as an ellipsoid. This is obviously an approximation, since we only consider $\varphi_i(c_b)$ to estimate $\varphi_i(b)$. However, if φ_i is regular enough, as a respiratory motion model is expected to be, this justifies the calculation of R^i_{db} by considering the intersections l^i_{db} of lines d with the ellipsoids $\varphi_i(b)$ (see Fig. 6.1b). Fig. 6.3 shows a test in which emissions elements have been modelled as spheres and deformed into ellipsoids with a pre-built displacement vector field (DVF).

The modelling of the emission elements as spheres that translate and deform locally into ellipsoids according to a given DVF, represents a novel contribution. Furthermore, computations of the system matrix elements are faster than those using classical methods of voxel/detector-tube intersection (e.g. Siddon algorithm [105]) used by others, e.g. [95, 49]. On the other hand, by approximating the voxel's cubic space by an inscribed sphere, there is a volume portion that is not covered (corners of pixel for the 2-D case). However, the volume distribution is such that computation of Eq. (6.2) fairly reflects

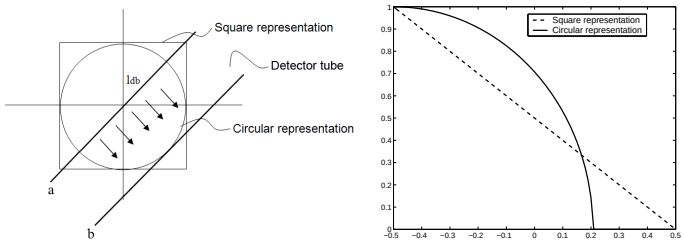

(a) (b)

Figure 6.4: Modelling emission elements. The circular representation is illustrated and compared with the square one (2-D case) (a). Fig. 6.4(b) is a plot of intersection lengths (equivalent to the detection probability) when a detector tube (represented as a line) moves from point a towards point b, where a minimum is reached for the circular representation.

the spatial interaction of emission elements with detector tubes. Fig. 6.4(b) shows for the 2-D case the normalized intersection length l_{db} (Eq. (6.2)) between a detector tube (represented as a line) and an emission element represented as a square and a circle (dashed and continuous lines respectively in Fig. 6.4(a)).

6.4 Attenuation correction

The value μ_b in an attenuation map $\mu(x)$, represents the linear attenuation coefficient for voxel b. As it is also known, this coefficient represents the fraction of a beam of gamma rays that is absorbed when it passes through voxel b. This coefficient is dependent on the tissue type the particular voxel represents and is typically obtained by using a transmission image to map voxel intensities to attenuation coefficients.

Along a detector tube d the attenuation experienced by a pair of photons can be written as:

$$\exp\left(-\int_d \mu(x)dx\right) \tag{6.7}$$

which can be approximated to

$$\exp\left(\sum_b -l_{db}\mu_b\right). \tag{6.8}$$

In presence of motion, we must take into account the displacements and deformations of emission elements. To do so, attenuation correction weights a_d^i associated to the detector tube d to each time state i can be computed as follows

$$a_d^i = \exp\left(\sum_b l_{db}^i \mu_b\right). \tag{6.9}$$

with μ_b assumed to be measured at the reference state.

This way, attenuation correction can be incorporated to the reconstruction step by modifying Eq. (6.2), as follows

$$R_{db}^C = \sum_i w_i a_d^i R_{db}^i. \tag{6.10}$$

6.5 Respiratory Modelling

6.5.1 Introduction

As it was presented in chapter 5, the respiratory motion correction methodology involves the use of a model of the patient's breathing pattern. As it was also discussed, obtention of such a model is not an easy task unless extra hardware is used. Nevertheless, use of additional hardware does not assure good estimation of the respiratory cycle. Indeed, it has been shown that using tracking devices based on external information (e.g. elasticized belt, skin markers, etc.) may not always correlate with lung tumor location [8, 120], which has motivated the use of more complex and not widely available tracking device systems (e.g. implanted radio-opaque markers).

Respiratory modelling has been performed in different ways. A group of methods, mostly used for radiotherapy purposes, describe the

respiratory cycle as a modified cosine function, with its amplitude, period and phase, as main parameters [77, 102, 21]. Other methods perform estimation of the respiratory cycle from other physiological waveforms (e.g. heart rate, blood pressure, central venous pressure, etc.) [103, 53]. In the context of the proposed motion correction methodology, these methods are not appropriated since respiratory motion is described only in one direction [76] or it is considered homogeneous [85]. Furthermore, these models do not take into account the spatial dependence of motions within the thorax. In [125], a finite-state respiratory model is proposed. It has the advantage of allowing motion description in a 3-D space. However, the spatial independence still exists. We have chosen a voxel-wise respiratory motion model, which allows to describe the location of each point in a given volumetric frame to its location in the next frame [123, 110]. Besides, the voxel-wise feature of this model eases the task of characterizing for each voxel the deformations it suffers due to respiration.

As a first approach this respiratory motion model, which we will call "simplified respiratory motion model", was obtained from computing displacement vector field (DVF) (i.e. a 3-D vector associated to each voxel, which describes the displacements due to respiration), computed between end-expiration and end-inspiration images of a healthy subject, to the patient's anatomy.

Since the simplified respiratory motion model does not account for inter-patient breathing variability and is obtained from one single subject, it can produce a respiratory motion model biased towards a specific breathing pattern. To account for this variability, a statistical model was constructed from a set of images coming from several subjects at different phases of the breathing cycle. From this statistical analysis, a first statistical model called STAT-1 was developed, which takes into account only the end-expiration and end-inspiration phases of half of a breathing cycle.

A second statistical model consisted in five states describing a com-

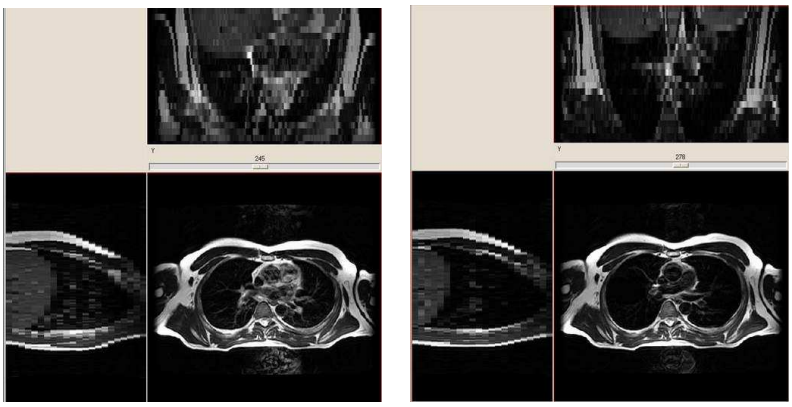

(a) Expiration (b) Inspiration

Figure 6.5: Two MRI images from a volunteer (taken at inspiration and expiration) were non-rigidly registered to create a real and known respiratory motion deformation.

plete cycle (end-expiration, intermediate state, end-inspiration, intermediate state and end-expiration). This model was called STAT-2 and its construction was motivated from the concern of using only the two extreme states, as is the case of STAT-1. For each one of the statistical models, the computed average transformation was used for the motion correction step.

Finally, each model needs to be adapted to the patient anatomy. In the next sections, description of the models construction and model adaptation to patient anatomy are described.

6.5.2 Materials

For the simplified model, two MRI images of a volunteer were taken at expiration and inspiration (see Fig. 6.5) to simulate the two respiratory phases used on the model. The images have size 512x512x12 voxels with a voxel size of 0.85x0.85x12 mm^3, T2 weighted sequence, repetition time and echo time of TR=2200 ms and TE=93 ms, respectively.

For the statistical models the dataset consisted in twelve volume

images acquired from twelve healthy subjects. Each image of dimensions 512x512x60 and a voxel size of 1.06x1.06x5.0 mm^3. For each subject, the Real-time Position Management (RPM) system (Varian Medical Systems, Palo Alto, CA) was used to monitor the respiratory cycle [1]. It consists of a plastic box with two reflectors, illuminated by an infrared light, which are tracked by a CCD camera. The marker is generally placed on the patient's abdomen. During the acquisition, the CCD camera records the motion of the RPM marker and the corresponding signal is stored in an ASCII file. This file mainly contains for each sample a time stamp, motion amplitude, and breathing phase.

For each axial slice (out of 60), 10 CT slices were acquired. The acquisition delay between two axial slices was chosen to be slightly longer (+ 1 second) than the breathing cycle duration to insure a coverage of an entire cycle for each table position. Thus, we obtained for each slice of the object, a representation at 10 different phases of the breathing cycle. Then, by processing the RPM file, images with a common time stamp were combined to produce volumetric images corresponding to each phase [107].

Fig. 6.6 shows as example the set of images for a complete respiratory cycle of one subject.

6.5.3 Single-subject based model

The single-subject model considers the deformation produced by respiration between the two extremal motion states of the breathing cycle (i.e. end-expiration and end-inspiration). To build this model, the two acquired MRI images representing end-expiration and end-inspiration (see Fig. 6.5) were non-rigidly registered with the Pasha algorithm [15].

The reference image was set to be the end-expiration image, whereas the floating image (the image to be registered against the reference one) was set to be the end-inspiration. This provides a volumic DVF

[1] Many thanks to Mr. Luc Simon, Mr. Philippe Giraud, Mr. Jean-Claude Rosenwald, and Mr. Vincent Servois for providing the data used for the PCA study.

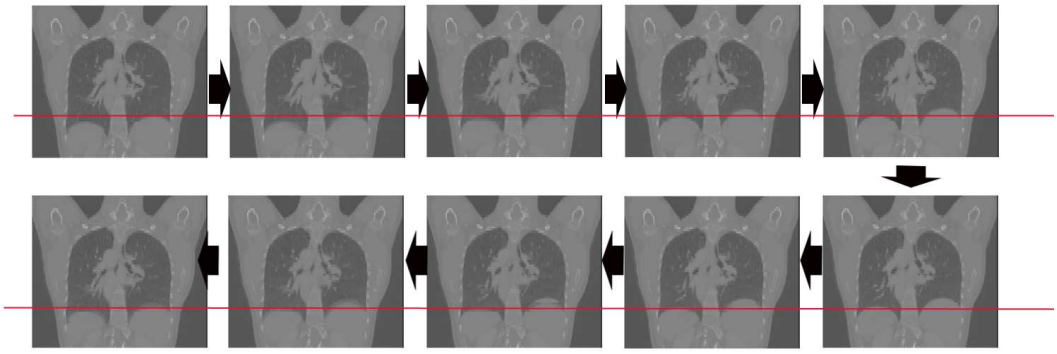

Figure 6.6: Complete respiratory cycle. Each image represents a specific phase within the breathing cycle. The arrows indicates the increase in the phase. The red lines are indicatives of motion at the bottom of the lungs.

(a 3-D vector per voxel) ψ describing the transformation of the end-expiration image towards the end-inspiration one. To simulate $(N-2)$ intermediate states (*i.e.* to use N states, including the extremal ones) when performing motion correction, transformations $\Phi_n(b)$ are then estimated at time state $n = 0 \dots N$, as follows

$$\Phi_n(b) = b + \frac{n}{N}\psi(b). \tag{6.11}$$

This discretization of the respiratory motion is by no means robust. Indeed, a point inside the lungs does not follow the same trajectory during exhalation and inspiration. Moreover, these two trajectories (one for exhalation and the other for inspiration) are certainly not straight paths between the two extremal positions (exhalation and inspiration). Thus, the motion discretization provided by Eq. (6.11) is a double approximation of the true respiratory motion of the imaged subject.

Moreover, since this motion depends on one single subject, it is likely to be biased, and not to be representative. For a better representability, we propose to compute a respiratory model from images of

a group of patients, which is the purpose of the next sections.

6.5.4 Statistical respiratory modelling through averaging of motion transformations

The statistical models, were conceived to be more representative of the population's breathing patterns. This, in order to obtain a more robust model than the single-subject based model, allowing a better approximation to the unknown patient's motion transformation. To obtain such a models, the average motion transformation computed from a given population is obtained. To do so, these motion transformations must be transformed to the common space of the average anatomy, to account for the anatomical differences found among subjects. Such task can be performed through the algorithm proposed by Guimond [43, 42] (see AppendixA.8.1 for more details). Once the average anatomy has been computed, the motion transformations computed on each subject can be adapted to the common anatomy. The different way these motion transformations were computed, generated the STAT-1 and STAT-2 models. To obtain the motion transformations, for each subject $k_{\{k=1...12\}}$ non-rigid registrations [15] were performed in two different ways, from where the two statistical models STAT-1 and STAT-2 were derived.

Before describing the way the motion transformations were computed, let's include some notations that would ease the description.

Let be I_i^k with $i = 1 \ldots 10$, the image describing the ith sample point within the breathing cycle for the subject k, and $\Upsilon^k(i,j)$ the non-rigid transformation between images I_i^k and I_j^k. $\Upsilon^k(i,j)$ is then an image of 3-D vectors that has the same size than I_i^k.

STAT-1 model

Since STAT-1 takes into account the end-expiration and end-inspiration phases of half of a breathing cycle, non-rigid registrations were per-

formed between images representing maximal and minimal amplitudes. Thus, transformations Υ^k_{1-6} where computed for each subject k.

Posteriorly, the averaging procedure (Appendix A.8.1) was applied to the set of I^k_6 images (corresponding to the reference state of STAT-1), obtaining the average image $\hat{I}_6$. Then, computation of affine transformations T^k_6 between the average image $\hat{I}_6$ and images I^k_6 are computed and applied to images Υ^k_{1-6} as follows

$$\tilde{\Upsilon}^k_{1-6} = T^k_6 \circ \Upsilon^k_{1-6} \circ {T^k_6}^{-1}, \tag{6.12}$$

where $\tilde{\Upsilon}^k_{1-6}$ describes the transformation between expiration and inspiration under the space configuration of $\hat{I}_6$.

Finally, the average transformation can be easily obtained by:

$$\bar{\Upsilon}_{1-6} = 1/N \sum_{k=1}^{N} \tilde{\Upsilon}^k_{1-6}. \tag{6.13}$$

With N the number of DVF's used in the averaging. With $\bar{\Upsilon}_{1-6}$ the obtained averaged transformation, which corresponds to the statistical model **STAT-1**.

STAT-2 model

For the second model, STAT-2, transformations Υ^k_{1-3}, Υ^k_{3-6}, Υ^k_{6-8} and Υ^k_{8-10} were computed for each subject k to describe a complete breathing cycle.

Posteriorly, averages models $\hat{I}_x$, $x = \{1, 3, 6, 8\}$ were obtained (Appendix A.8.1), and affine transformations T^k_x, $x = 1, 3, 6, 8$ between the average image $\hat{I}_x$, $x = \{1, 3, 6, 8\}$ and images I^k_x, $x = \{1, 3, 6, 8\}$ were computed and applied to images Υ^k_{1-3}, Υ^k_{3-6}, Υ^k_{6-8}, and Υ^k_{8-10}, as follows

$$\tilde{\Upsilon}^k_{1-3} = T^k_1 \circ \Upsilon^k_{1-3} \circ T^{k^{-1}}_1 \tag{6.14}$$

$$\tilde{\Upsilon}^k_{3-6} = T^k_3 \circ \Upsilon^k_{3-6} \circ T^{k^{-1}}_3 \tag{6.15}$$

$$\tilde{\Upsilon}^k_{6-8} = T^k_6 \circ \Upsilon^k_{6-8} \circ T^{k^{-1}}_6 \tag{6.16}$$

$$\tilde{\Upsilon}^k_{8-10} = T^k_8 \circ \Upsilon^k_{8-10} \circ T^{k^{-1}}_8. \tag{6.17}$$

This produces a set of transformations, which can be averaged to obtain the **STAT-2 model**, as follows

$$\bar{\Upsilon}_{1-3} = 1/N \sum_{k=1}^{N} \tilde{\Upsilon}^k_{1-6} \tag{6.18}$$

$$\bar{\Upsilon}_{3-6} = 1/N \sum_{k=1}^{N} \tilde{\Upsilon}^k_{3-6} \tag{6.19}$$

$$\bar{\Upsilon}_{6-8} = 1/N \sum_{k=1}^{N} \tilde{\Upsilon}^k_{6-8} \tag{6.20}$$

$$\bar{\Upsilon}_{8-10} = 1/N \sum_{k=1}^{N} \tilde{\Upsilon}^k_{8-10}. \tag{6.21}$$

With N the number of DVF's used in the averaging.

6.5.5 Statistical analysis of population-based model

The data used to build STAT-1 was analyzed by means of a PCA study, in order to assess the variability of the respiratory motions. As a side effect, it also allows to detect (and remove from the population) the outliers in this population.

This analysis was then applied to the set of displacement vector field $\bar{\Upsilon}^k_{1-6}$ of STAT-1. Each sample k is then made of 3x512x512x60 values. By applying such analysis, it is possible to study the variability of the deformations with respect to a reference state, which typically is the mean transformation. Furthermore the orthogonality property

of the PCA decomposition allows us to study non-redundant information and to characterize the variability of the deformations in a compact way. PCA also allows to study possible outliers from the input dataset, which allows to improve the data used to construct a statistical model. Although other tools exist to analyze multidimensional data (see [38, 29, 118] for example), in this study PCA was chosen mainly due to its adequacy to this particular problem and its simplicity of implementation.

As it was stated before, PCA performs a decomposition of a random vector into its orthogonal and non-correlated components or modes (in our case this vector corresponds to a displacement vector field).

Formally, given a learning dataset N formed by n random observation vectors $\mathbf{x_i} = (x_1 \dots x_p)^t{}_{i=1\dots n}$, PCA estimates a modal approximation of $\mathbf{x}$ of the form

$$\mathbf{x} = \overline{\mathbf{x}} + \mathbf{\Phi b}, \tag{6.22}$$

where $\overline{\mathbf{x}}$ is the mean value of the data set

$$\mathbf{x} = 1/n \sum_{i=1}^{n} \mathbf{x_i}$$

$\mathbf{\Phi}$ is the matrix formed by the eigenvectors of the covariance matrix $\mathbf{C}$ of the dataset N,

$$\mathbf{C} = \frac{1}{n} \sum_{i=1}^{n} d\mathbf{x_i} d\mathbf{x_i}^t, \tag{6.23}$$

with $d\mathbf{x_i} = \mathbf{x_i} - \overline{\mathbf{x}}$. And the vector $\mathbf{b} = (b_1 \dots b_p)$ that represents the observation vector under the new modal base. Each element b_i corresponds to the modal amplitude associated to the ith mode of variation.

The matrix $\mathbf{\Phi}$ can be found by computing the diagonalization of C (see appendix A.11 when $n \ll p$):

$$\mathbf{C} = \mathbf{\Phi} \Lambda \mathbf{\Phi}^t \tag{6.24}$$

with,

$$\mathbf{\Phi} = (\phi_1 | \dots \ |\phi_p) \ \text{ and } \Lambda = \begin{pmatrix} \lambda_1 & 0 & \dots & 0 \\ 0 & \lambda_2 & \dots & 0 \\ \vdots & \vdots & \ddots & \vdots \\ 0 & 0 & \dots & \lambda_p \end{pmatrix} \tag{6.25}$$

The set of scalars $\{\lambda_i \dots \lambda_p\}$ are the eigenvalues of the covariance matrix $\mathbf{C}$ such as $\lambda_1 \geq \lambda_2 \geq \dots \geq \lambda_p$.

One aspect of interest about PCA is that by decreasing the number of modes used to represent $\mathbf{x}$, it can produce a more compact data representation[2]. Let's consider the first m modes of variation ($m \leq p$). The vector of observation $\mathbf{x}$ can be represented in a more compact way as:

$$\mathbf{x} = \overline{\mathbf{x}} + \mathbf{\Phi_m b_m} \tag{6.26}$$

With $\mathbf{\Phi_m} = (\phi_1 | \dots \ |\phi_m)$ and $\mathbf{b_m} = (b_1 \dots b_m)$ a submatrix and a subvector of $\mathbf{\Phi}$ and $\mathbf{b}$ respectively. However, using less components to represent the observation vector produces an error caused by the reduction on information used in the new compact representation. The quality of the representation obtained with the first m modes of variation can be measured by the ratio between the accumulated variance up to mode m and the total variance. This measure, called the inertia ratio, can be calculated as follows:

$$\tau = \frac{\sum_{i=1}^{m} \lambda_i}{\lambda_T} \ \text{ with } \lambda_T = \sum_{i=1}^{p} \lambda_i = trace(\Lambda) \tag{6.27}$$

Other use of PCA of great interest is its capacity to generate new cases that are not part of the initial learning set N. Let's make the assumption that the vector $\mathbf{x}$ follows a gaussian distribution with mean

[2]This property has been exploited in the past in data compression schemes.

$\overline{\mathbf{x}}$ and covariance $\mathbf{C}$. Under this hypothesis vector $\mathbf{b}$ follows in turn a gaussian distribution, which allows to obtain the margins of admissible or more plausible values for the vector $\mathbf{b}$ [3]:

$$-3\sqrt{\lambda_i} \leq b_i \leq +3\sqrt{\lambda_i} \tag{6.28}$$

This way, by varying b_i in (6.26) according to (6.28) new cases can be produced, which used along with the compactness property, allow to study each mode of deformation separately at its most probable range of variation.

Another measure commonly used in PCA analysis is the so-called contribution measure, $Cr(i,k)$ that gives the contribution of the subject i to the mode k. It is defined as:

$$Cr(i,k) = \frac{1}{n}\frac{(b_i^k)^2}{\lambda_i}, \tag{6.29}$$

with b_i^k the modal amplitude of subject i for the kth mode and λ_i the ith eigenvector.

The analysis of the terms $Cr(i,k)$ allows to study possible outliers of the learning dataset. This, since a disproportioned Cr value would indicate a strong influence of a particular subject over a certain mode, introducing undesirable bias in the principal modes decomposition.

Finally, the generalization capacity of the model was studied. As it was stated, PCA offers the possibility of generating new subjects belonging to the studied class (i.e. to produce an subject that falls within the range of variation given by the learning dataset). From this fact, one could be interested in checking the precision of the model to reproduce a certain known subject (chosen from the input dataset) without using such observation in the model generation. In other words, the idea is to measure the reproducibility capacities of a model generated with a reduced input dataset that lacks the observation for which the

[3] In fact $P(|b_i| \leq 3\sqrt{\lambda_i}) = 99.7\%$

model's output is compared against. This is known as the "leave-one-out" method.

Let's define $\mathbf{x_e}$ as the observation vector being excluded from the input dataset N. Now, from the reduced dataset $N_e = N - \mathbf{x_e}$ the excluded observation vector is represented in a modal base as

$$\mathbf{b_e} = \mathbf{\Phi^t}(\overline{\mathbf{x}} - \mathbf{x_e}), \tag{6.30}$$

where $\mathbf{\Phi}$ and $\overline{\mathbf{x}}$ are generated from the reduced input dataset N_e.

The appealing compactness property of PCA can be incorporated here to study the error produced when reconstructing the excluded observation with a limited number of modes. Formally, let's define $\mathbf{x_{r,b}}$ as the reconstructed observation of $\mathbf{x_e}$ considering the first m modes of variation:

$$\mathbf{x_{r,m}} = \overline{\mathbf{x}} + \mathbf{\Phi_m}\mathbf{b_{e,m}}, \tag{6.31}$$

with $\mathbf{b_{e,m}}$ the vector formed by the m first components of $\mathbf{b_e}$.

Thus, the error of reconstructing the subject $\mathbf{x_e}$ with m modes of variation can be defined as:

$$e_{i,m} = ||\mathbf{x_{r,m}} - \mathbf{x_e}||. \tag{6.32}$$

A global reconstitution error e_T^m that measures the error generated by excluding each subject at a time and considering the first m modes of variation can be computed as follows:

$$e_T^m = \frac{1}{n}\sum_{i=1}^{n} e_{i,m}. \tag{6.33}$$

6.5.6 Respiratory model adaptation

As previously discussed, adaptation of the generated respiratory models (simplified, STAT-1 and STAT-2) are needed in order to match

them to the patient anatomy, and so, to produce and estimation of the respiratory motion of the patient.

For sake of simplicity, let's be Θ the transformation describing the respiratory model, which needs to be adapted to the patient's anatomy. This consideration also allows to separate both steps of model construction and model adaptation, since in practice transformation Θ could be constructed in different ways.

We adapt the respiratory model Θ to a given patient by transforming it by an affine transformation T. We consider two different cases

1. If there is an attenuation image, that is acquired with breath holding, generally at inspiration, we register the inspiration image of the model with this attenuation image (registration is done by registering the segmented lungs), which yields the transformation T.

2. If such attenuation image is not available, we consider the reconstructed image (without any motion correction). The "lungs" in this image, that can be segmented by thresholding, represent the volume spanned by the true lungs during the respiratory cycle. To simulate the same effect with the model, we segment the lungs in the expiration and inspiration images of the models. By merging them into an image I_{av}, we obtain also the volume spanned by the lungs during respiration. By registering I_{av} with the lungs segmented from the non-corrected reconstructed image, we finally get the transformation T.

This affine transformation T allows the transform the respiratory model Θ as follows

$$\tilde{\Theta} = T \circ \Theta \circ T^{-1}. \tag{6.34}$$

The composed transformations in Eq. (6.34) allow to adapt the spatial configuration of each point in Θ (i.e. the position of each vector in

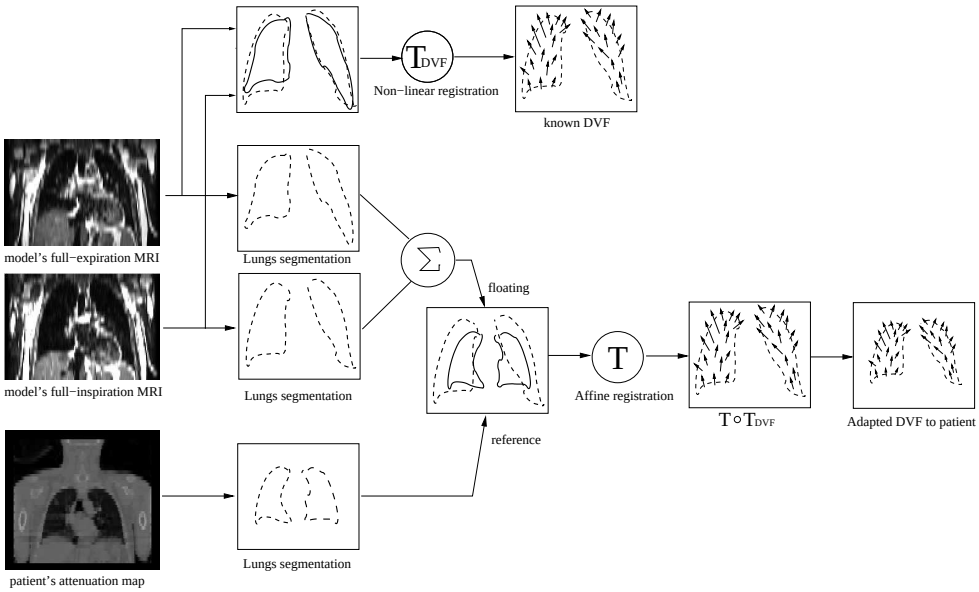

Figure 6.7: Adapting a known respiratory motion transformation to patient anatomy.

the transformation image), and the motion magnitude (i.e. the length of each vector in the transformation image). This way, the adapted transformation $\tilde{\Theta}$ describes the respiratory motion of the model Θ in the space configuration of the patient.

To illustrate these steps, Fig. 6.7 shows as a matter of example the adaptation performed between the simplified model and the patient's attenuation map.

6.5.7 Results

Simplified model

The simplified model was later used on patient data in conjunction with the motion correction methodology. Here, as a matter of example, results from the adaptation step to one patient data (described in chapter 8).

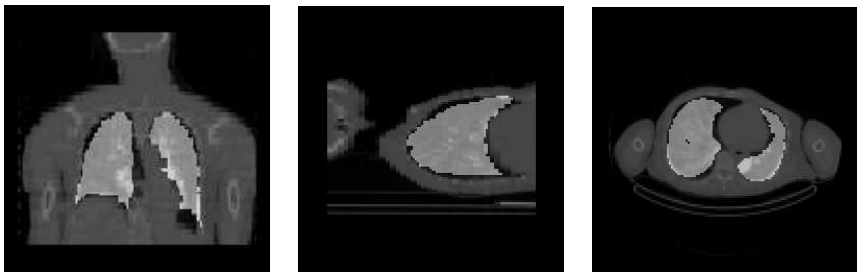

(a) Coronal (b) Sagittal (c) Axial

Figure 6.8: Example of image fusion between a patient's attenuation map and the averaged lungs anatomy of the simplified respiratory motion model after affine registration.

Fig. 6.8 shows the result of the affine registration between attenuation map of patient number two with the anatomy of the simplified respiratory motion model.

Fig. 6.9 shows the axial slice number ten of the expiration MRI image used to construct the simplified model, and the displacement vector field represented as vectors.

Finally, Fig. 6.10 shows the adaptation result of the simplified model to the patient anatomy.

Statistical models

Fig. 6.11 shows the obtained average image computed to transform the subjects into a common anatomy.

Fig. 6.12 show the evolution of the RMSN and NID values (Eqs. A.42 and A.43) used to measure, as a function of the iterations, the convergence of the averaging anatomy procedure. It can be noticed the fast convergence at the beginning (first two iterations), from where a slower convergence is attained. Four iterations were computed, and the obtained average image was selected as the common anatomy over which the subjects were transformed.

The contribution of each subject to each mode (i.e. principal mode

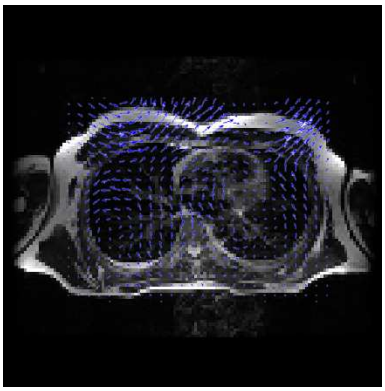

Figure 6.9: Axial slice number 10 of expiration MRI image. Displacement vector field is represented as vectors.

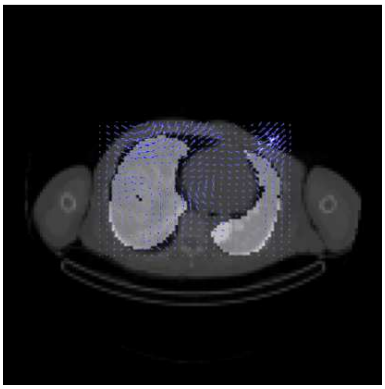

Figure 6.10: Simplified model adapted to the patient anatomy. Displacement vector field is represented as vectors.

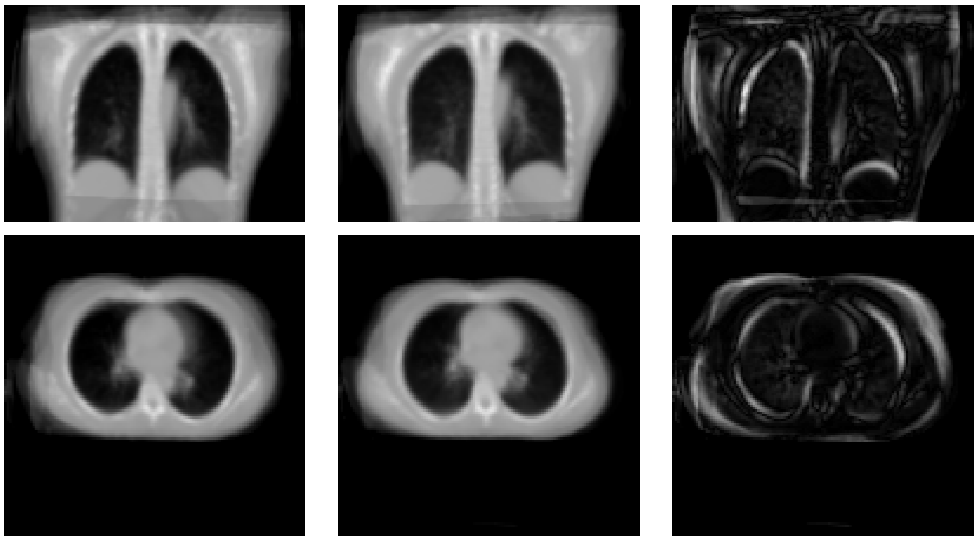

(a)First iteration (b) Fourth iteration (c) Absolute difference

Figure 6.11: Coronal and Axial images from average model obtained at first iteration (a), fourth iteration (b) and absolute difference between them (c)

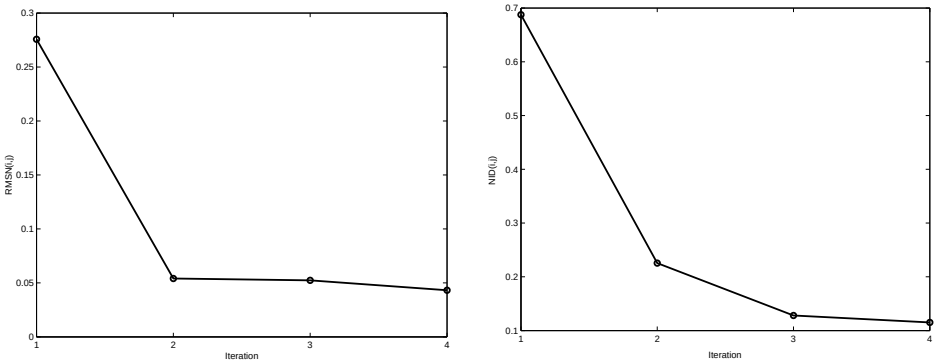

(a) (b)

Figure 6.12: Shape and intensity differences between successive iterations given by the RMSN and NID measures respectively. The image converges towards a shape and intensity average image.

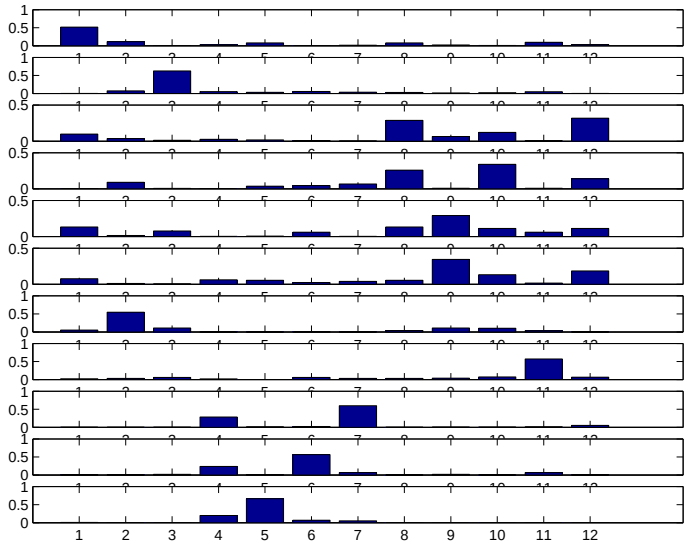

Figure 6.13: Contribution of each subject (columns) to each mode (rows). Modes order is increasing starting with first one at the upper row.

of deformation) was measured according to Eq. (6.29). Fig. 6.13 shows the obtained results. The modes are ordered as rows starting with the first mode in the upper row (see Appendix A.11 for computational issues).

It can be noticed from Fig. 6.13 that the first mode is strongly influenced by the first subject. By visual inspection of its corresponding displacement vector field, it is quite noticeable the amount of craniocaudal displacement (which is expected to be the main mode of deformation) in comparison with the rest of the learning dataset. Further inspection of Fig. 6.13 allows to determine that the second mode is heavily influenced by the third subject (contribution over 50%), which corresponds to an aberrant case (see Fig.6.14 lower lung region). As a consequence, the first and third subjects were rejected from the learning set. Fig. 6.15 shows the new contribution of each subject to the each mode, and Fig. 6.16 the new contribution of each subject to the first mode.

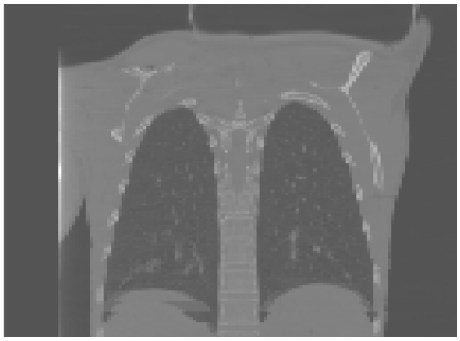

Figure 6.14: Coronal slice of third subject. It can be seen the artifact at the base of the lungs producing the high contribution of this subject to the second mode of variation. This subject was excluded from the final dataset.

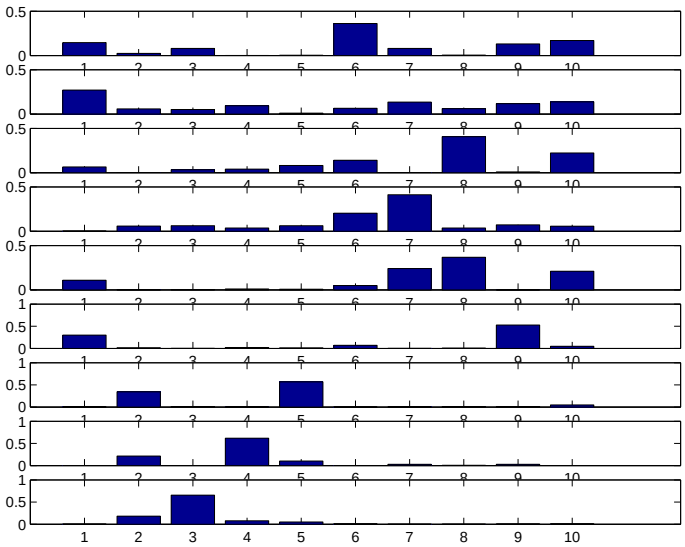

Figure 6.15: Contribution of each subject (columns) to each mode (rows) with subjects one and three rejected. Modes order is increasing starting with first one at the upper row.

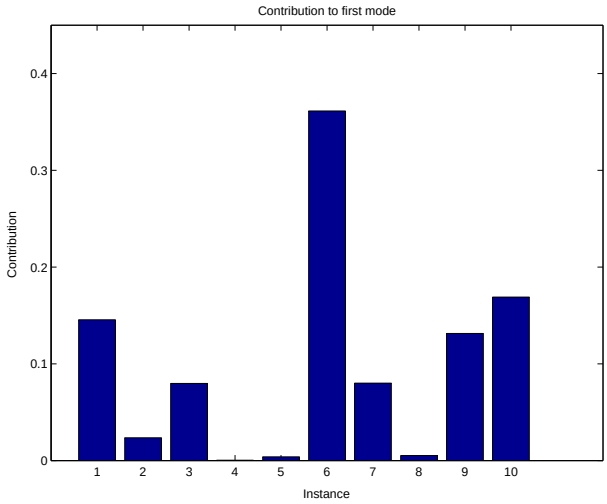

Figure 6.16: Contribution of each subject to the first mode when subject one and three have been rejected. A much better balanced contribution is seen.

Once outliers and aberrant cases have been eliminated from the dataset, the STAT-1 model was set to the average motion transformation obtained from the PCA study applied to the reduced set. Figure 6.17 shows the 3-D displacement vector field and the isosurfaces of both states of respiration considered by the model.

The inertia ratio (Eq. (6.27)) was calculated for the ten-subjects dataset. Fig. 6.18 presents the obtained results. It can be noticed the expected increase on the inertia values as more modes are considered. It can also be remarked that the first mode represent by itself almost 30% of the total variance, by considering the first four modes of variation one can reproduce approximately nearly 70% of the total information.

To study the preferred deformations expressed by the first modes of the PCA decomposition, a specificity study was carried out by generating deformations according to the range $-3\sqrt{\lambda_i} \leq b_i \leq +3\sqrt{\lambda_i}$. The obtained transformations were then applied to the mean lungs form for better visualization and understanding on how each mode acts.

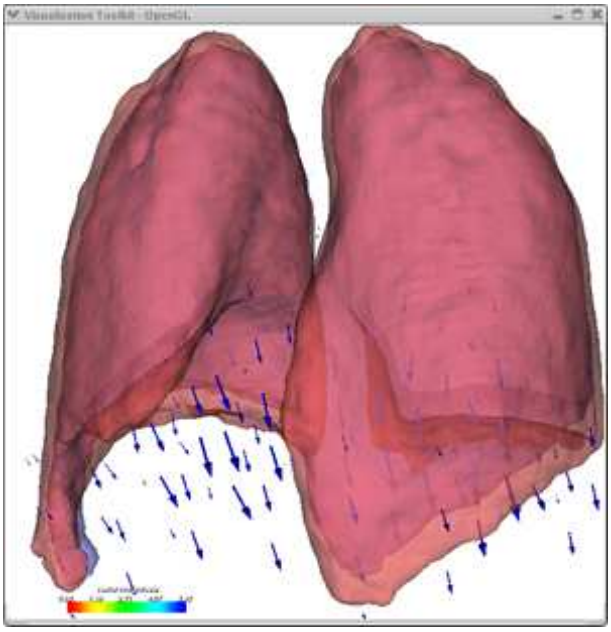

Figure 6.17: The STAT-1 model. The 3-D DVF is rendered as arrow glyphs, and isosurfaces were generated corresponding to the two states of respiration considered by the model.

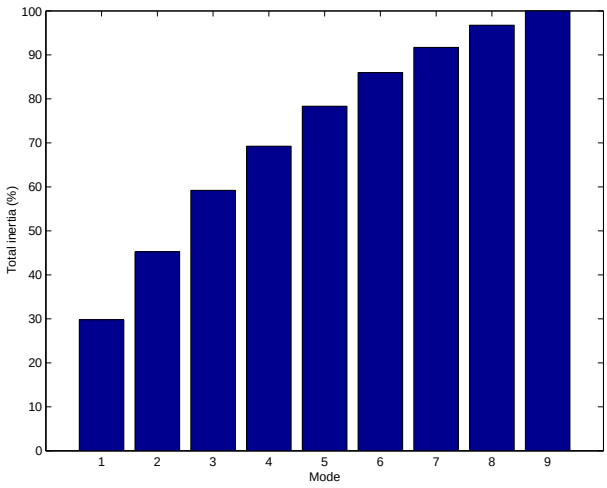

Figure 6.18: The inertia ratio measures the accumulated variance contribution of each mode to the modal decomposition.

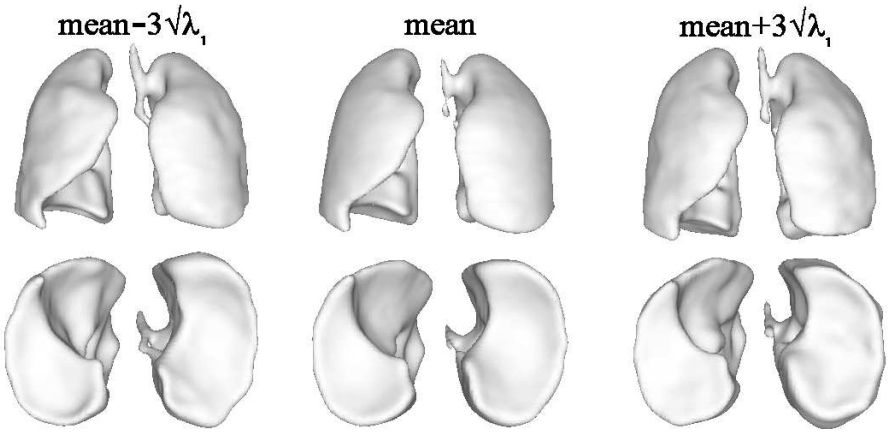

Figure 6.19: First mode of variation. The modal amplitude for the first mode is varied in the range $-3\sqrt{\lambda_1} \leq b_1 \leq +3\sqrt{\lambda_1}$.

Fig. 6.19 shows the results obtained for the first mode of variation.

Two supplementary visualizations are given. The first one corresponds to the superimposition of the iso-surfaces representing $\overline{x}+3\sqrt{\lambda_1}$ and $\overline{x}-3\sqrt{\lambda_1}$. Fig. 6.20 shows the result obtained. The second one, shown in Fig. 6.21, corresponds to the absolute difference between image segmentations of the lungs at $\overline{x}+3\sqrt{\lambda_1}$ and $\overline{x}-3\sqrt{\lambda_1}$. Similarly, the second mode of variation is visualized following the same chosen modes of visualization. The results obtained are presented in Fig. 6.22, Fig.6.23 and Fig.6.24.

At this point, the deformations are mostly governed by expansions and contractions in the cranio-caudal direction and expansion and contractions at the base of the lungs. The third mode of variation is more complex to visualize following the method previously used. Rather than comparing between extreme points in the range of modal amplitudes (i.e $\overline{x}+3\sqrt{\lambda_i}$ and $\overline{x}-3\sqrt{\lambda_i}$), the third mode is better visualized by comparing it with the mean form. Fig. 6.26 presents the result obtained.

The fourth mode describes the little remaining global expansion of

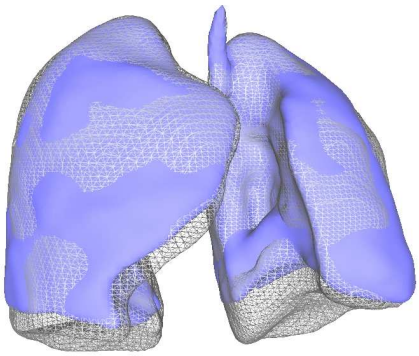

Figure 6.20: Superimposition of isosurfaces representing $\overline{x} + 3\sqrt{\lambda_1}$ (wire-frame) and $\overline{x} - 3\sqrt{\lambda_1}$ (blue surface) for the first mode of variation.

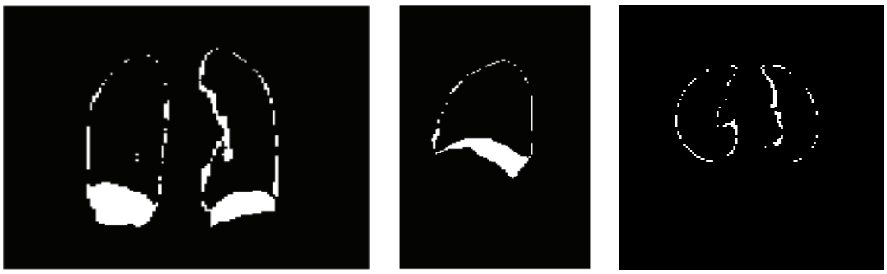

(a) Coronal (b) Sagittal (c) Axial

Figure 6.21: Absolute image difference between lungs image segmentation at $\overline{x} + 3\sqrt{\lambda_1}$ and $\overline{x} - 3\sqrt{\lambda_1}$.

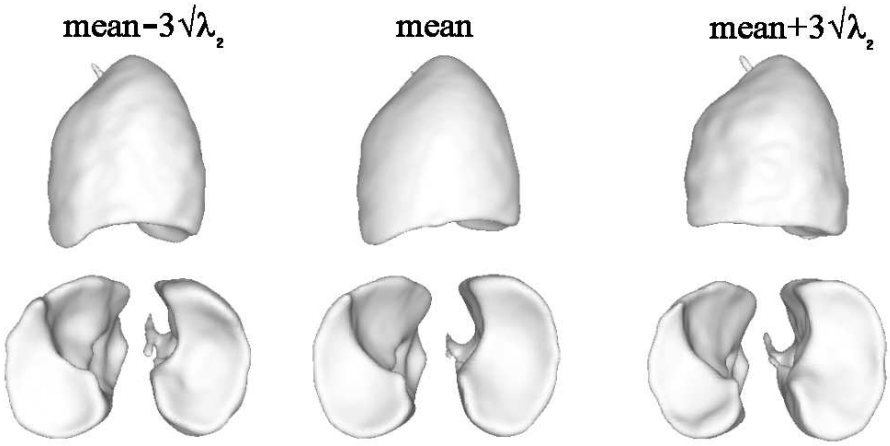

Figure 6.22: Second mode of variation. The modal amplitude for the second mode is varied in the range $-3\sqrt{\lambda_2} \leq b_2 \leq +3\sqrt{\lambda_2}$.

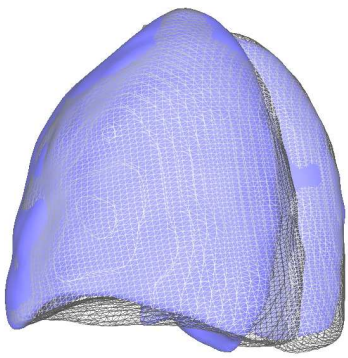

Figure 6.23: Superimposition of isosurfaces representing $\overline{x} + 3\sqrt{\lambda_2}$ (wire-frame) and $\overline{x} - 3\sqrt{\lambda_2}$ (blue surface) for the second mode of variation. Notice the deformation at the base of the lungs.

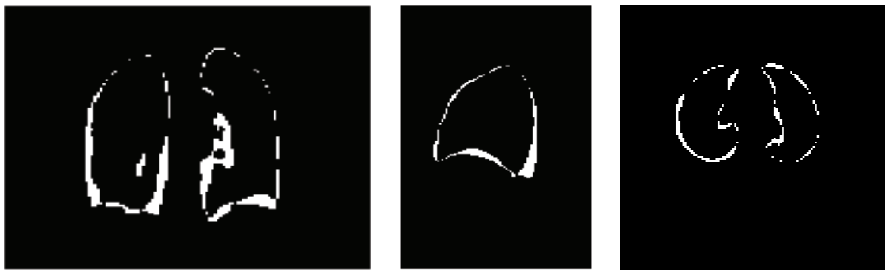

(a) Coronal (b) Sagittal (c) Axial

Figure 6.24: Absolute image difference between lungs image segmentation at $\overline{x} + 3\sqrt{\lambda_2}$ and $\overline{x} - 3\sqrt{\lambda_2}$.

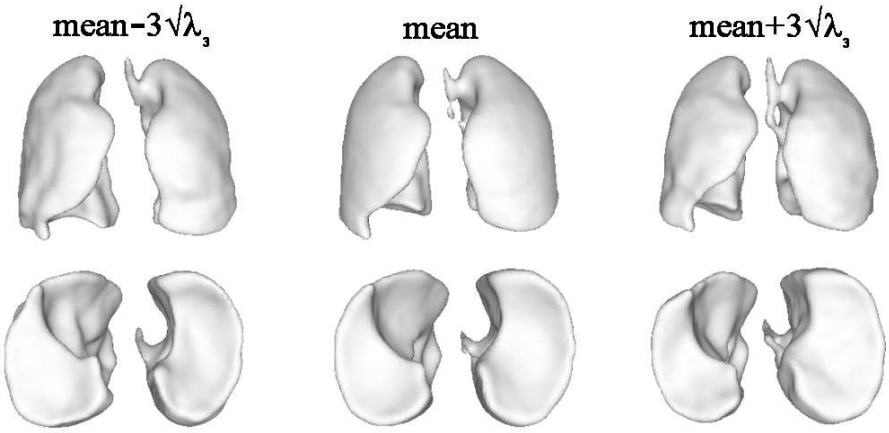

Figure 6.25: Third mode of variation. The modal amplitude for the third mode is varied in the range $-3\sqrt{\lambda_3} \leq b_3 \leq +3\sqrt{\lambda_3}$.

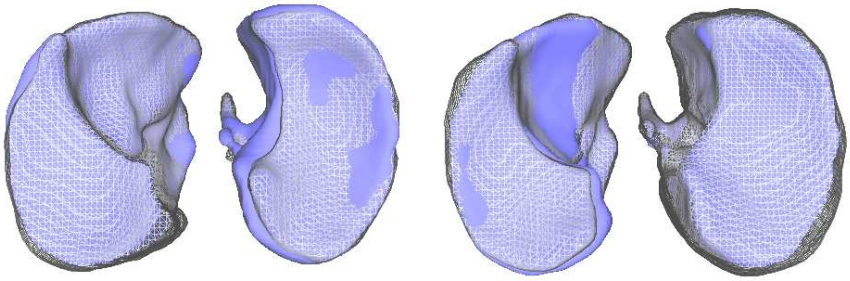

Figure 6.26: Superimposition of isosurfaces representing $\overline{x}-3\sqrt{\lambda_3}$ (left wireframe) and $\overline{x}+3\sqrt{\lambda_3}$ (right wireframe) against $\overline{x}$ (blue surface) for the third mode of variation.

the lungs. Fig. 6.27 shows the iso-surfaces obtained for $\overline{x} - 3\sqrt{\lambda_4}$ and $\overline{x} + 3\sqrt{\lambda_4}$ and Fig. 6.28 shows the absolute image difference between lungs image segmentations at $\overline{x} + 3\sqrt{\lambda_4}$ and $\overline{x} - 3\sqrt{\lambda_4}$. Only these two visualization methods were chosen for the fourth method since they provide the best way to inspect and study the deformations it describes.

Fig. 6.29 presents the progression of the global reconstitution error obtained by considering more modes of variation.

Comparing the simplified model and STAT-1

It was mentioned before that one of the interest of the statistical models was that of including subject physiological variability in order to obtain a more robust model which under the initial consideration would yield better results than a simplified model not representative of the breathing cycle. The statistical STAT-1 model was compared with the simplified one. For this, on both anatomies, image segmentation of the lungs was performed and then transformed by means of an affine transformation into the common reference configuration of the average anatomy. The obtained affine transformation was then used to trans-

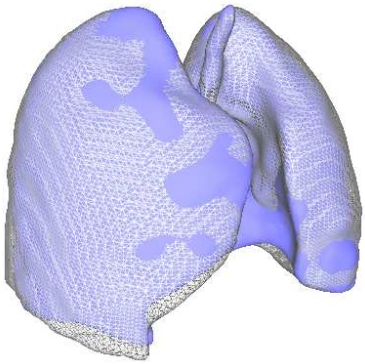

Figure 6.27: Superimposition of isosurfaces representing $\overline{x} - 3\sqrt{\lambda_4}$ (wire-frame) and $\overline{x} + 3\sqrt{\lambda_4}$ (blue surface) for the fourth mode of variation. Notice the regular distance between surfaces compared with previous one.

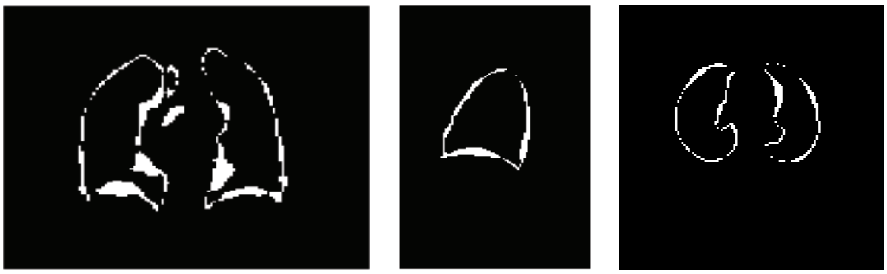

(a) Coronal (b) Sagittal (c) Axial

Figure 6.28: Absolute image difference between lungs image segmentation at $\overline{x} + 3\sqrt{\lambda_4}$ and $\overline{x} - 3\sqrt{\lambda_4}$.

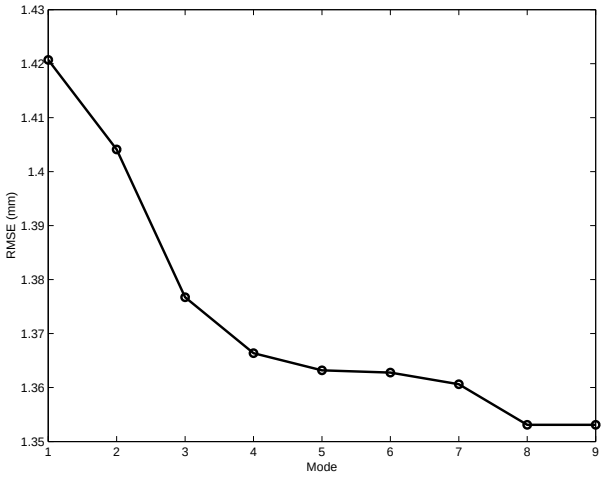

Figure 6.29: Leave-one-out study performed with the data set of ten observations. The mean error over the set of observations is plotted against the number of modes used to reconstruct the subject "left out".

form the displacement vector fields of each model. Once in a common spatial configuration, the residuals errors at each voxel were measured and a relative error with respect to the STAT-1 model was computed as follows:

$$\frac{\|v_s(b) - v_{stat1}(b)\|}{\|v_{stat1}(b)\|}. \tag{6.35}$$

Where $v_s(b)$ and $v_{stat1}(b)$ corresponds to the vector describing the displacement of voxel b given by the simplified and STAT-1 models respectively.

Application of (6.35) shows that the relative error with respect to the STAT-1 model varies in the range of $[6 \pm 5]\%$.

6.5.8 Discussion

The fact of using a single respiratory model (coming from a single subject or an average one) as a layout to produce patient specific res-

piratory motion models yields an estimation method which lacks of robustness and is far from being realistic. We were encouraged however by the fact that under the given constraints (no external tracking devices, retrospective reconstruction, nor specific data acquisition protocols), incorporation of such model can bring improvements on the reconstructed images. In the lack of a ground truth to evaluate and validate the results, the efforts were focused, to study the validity of the simplified method with respect to the statistical ones and to validate the linear hypothesis imposed for the statistical method STAT-1 with respect to the results yielded by STAT-2.

The linear transformation given by (6.11) is not realistic and was chosen as a first approximation. The hypothesis was, that under the given motion correction and image reconstruction constraints, this approximation can yield good results. Comparison with the STAT-2 model will allow to verify this hypothesis on the basis of motion corrected images.

As seen in Fig. 6.8, some residual registration errors are still present. No registration errors measurements were performed. However, in chapter 8, experimental results on simulated data were performed to study the impact of affine registration errors on the reconstructed motion corrected images.

For the statistical models, a first remark is the use of the contribution measure (Eq.(6.29)) to search for possible outliers and aberrant cases, which could introduce biases into the statistical analysis. This point is of importance since our interest is to produce a model which fairly represent a given population, so it can be used for motion correction in the absence of a patient-based respiratory motion model.

By inspecting Fig. 6.19 it can be concluded that the first mode characterizes mainly the deformations in the cranial-caudal direction and in a small degree the expansion anterio-posterior perceptible mostly on the left lung. From Fig. 6.22, 6.23, and 6.24 it can be concluded that the second mode of variation characterizes an expansion and contrac-

tion of the lungs at its base. The third mode of deformation describes the asymmetry with respect to the central axe between lungs during respiration. One could think of a breathing cycle producing a deformation that expands and contracts the lungs in a direction nearly parallel to this axe (as described by the first mode of variation), which in practice, and as highlighted by the third mode, does not occur. Finally, and as stated before, the fourth mode describes the little remaining global expansion of the lungs.

From the comparison between the STAT-1 model and the simplified one, a good match between models was found in terms of relative error with respect to the STAT-1 model. In this comparison, the largest differences were located at the base of the lungs. This could be caused by larger involuntary inspirations of the volunteer during the simulation of end-inspiration and end-expiration states. The results indicate that a good agreement exist between motion transformations, which in turn is expected to produce similar results of motion correction. On the other hand, although a good agreement was found between models, this fact does not validate the use of one single subject to create the simplified model. In practice if this method will be used, care must be taken when choosing the known respiratory motion, which would be checked against a model such as STAT-1 or so.

Chapter 7

Parallel Implementation

This chapter presents further details concerning implementational aspects, and introduces some techniques created to improve the speed of the algorithm.

7.1 Parallel Implementation

In chapter 4 the slow convergence of the MLEM algorithm has been already noticed and some solutions were presented in order to decrease the convergence time. While in two dimensions speed issues are not difficult to solve (e.g. ordered subsets approaches, pixel-based block iterative algorithms, better data access mechanisms, etc.), in three dimensions, a more brute force method like parallelism is required.

Parallelization of EM algorithms has been already used to speedup the convergence, in [63] a summary of previous works is described. Here the common denominator has been the distribution of the computational load of forward and backward projections over a set of processors. The main aspect of the algorithm in terms of parallelization, is without doubt the independence between neighbor emissions elements over a single iteration, which eases its implementation.

Our implementation is composed by three stages of parallelism. First, as suggested by equation (6.1), calculus of the normalization

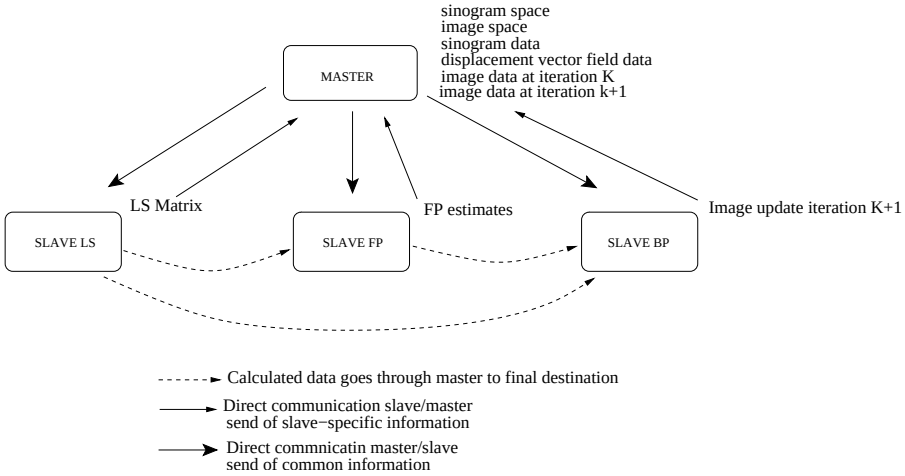

Figure 7.1: Implementation diagram of parallelized MLEM algorithm.

term for the corrected detection probability is performed before the steps of forward and back projection. Then, parallelized forward projection is performed. The counts estimates are stored and used in the next and final step of parallelization: backward projection and image update. Fig. 7.1 shows a diagram describing the relationship between each one of parallelization task and a master process.

Each box in Fig. 7.1 represents an entity of execution, starting by the master that makes the light calculations (i.e., calculating the sinogram and image space dimensions, reading the sinogram data file, initializing the image to be reconstructed, etc.). The first slave created is *SlaveLS*, which calculates the normalization term in equation (6.1). Once the slave has finished its task, it sends the data back to the master, which store it for later use. The second slave, *SlaveFP*, is in charge of the forward projection part (i.e., right denominator in equation (4.16)). Besides from the basic information sent by the master, it receives the already calculated normalization term. Once the the detection count estimates have been computed, they are sent back to the master, which will spawn the last set of slaves that perform the back-projection operation. Once again, the data calculated in the pre-

vious steps is sent to every *SlaveBP*. Once the *SlaveBP* has finished its work, it sends the portion of the updated image estimate to the master, which gets the data from each slave and assembles the image. At this point an iteration is completed.

For the communication between master and slaves, the *PVM (Parallel Virtual Machine)* software was used [33] and execution performed on the INRIA Sophia Antipolis cluster system [41].

7.2 Acceleration schemes

Geometrical considerations can be used to diminish the number of calculations in Eq. (4.16). Specifically in the two more computationally expensive operations: forward and backward projection. Acceleration schemes are discussed for the static case (no motion) and dynamic case (motion correction is considered).

7.2.1 Static case

For the static case the first and simplest approach consisted in computing a region of interest that takes into account the geometrical space traversed by a specific detector tube (see Fig. 7.2).

The well-known Bresenham's algorithm [12, 119] used to represent a continuous line in a discrete space was incorporated as a better accelerator. While the goal of the Bresenham's algorithm is to better represent a continuous line over a grid space, it does not incorporate all the pixels (2-D case) crossed by the line. This, in our case, is of vital importance in order to take into account all voxels contributing to a specific detector tube. Therefore, for each voxel given by the Bresenham's algorithm (in its 3-D version), a 6-neighborhood was considered to ensure that the voxels crossed by the detector tube were included. Fig. 7.3 shows the result from the implementation of the 3-D Bresenham's algorithm with the previously mentioned 6-neighborhood.

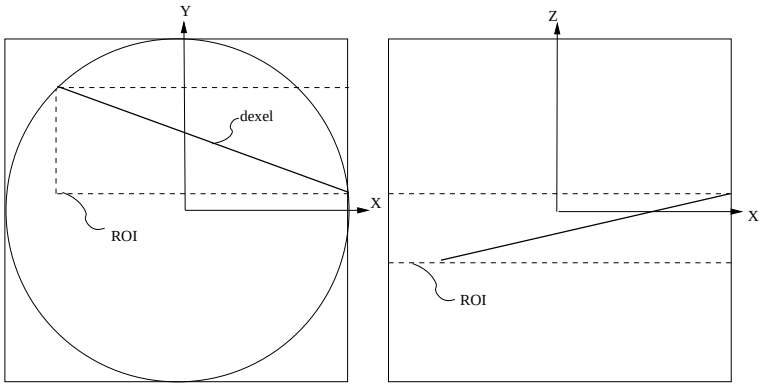

Figure 7.2: Reducing forward projection computation times by selecting a region of interest.

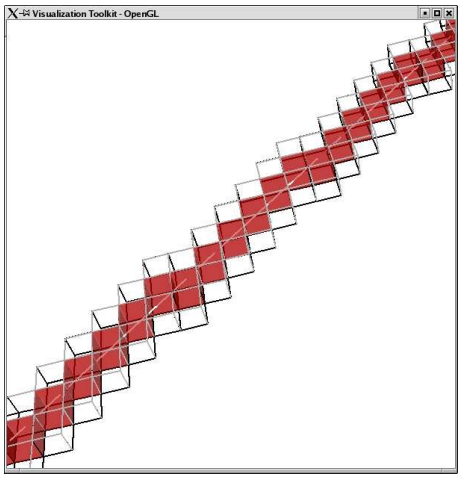

Figure 7.3: Bresenham and 6-neighboring to accelerate forward projection. Red cubes are the ones from the 3-D Bresenham's algorithm, and the others are the 6-neighbors for each of the red cubes. This, to ensure that all voxels traversed by the detector tube are included.

We will define $Bresenham(d)$ as the set of voxels obtained after application of the Bresenham's algorithm plus the 6-neighborhood.

To accelerate the backward projection step, let's first review the non-accelerated structure. For a given emission element b, the backward projection consists in computing

$$\sum_{d} \frac{n_d R_{db}}{\widetilde{n}_d}, \forall\ d \in D \tag{7.1}$$

with D the set of all detector tubes forming the scanner system and $\widetilde{n}_d$

$$\widetilde{n}_d = \sum_{b'} \lambda_{b'}^{<K>} R_{db'}, \tag{7.2}$$

the current estimated value for emissions detected by detector tube d.

As not all detector tubes d will cross the emission element b (yielding null probabilities R_{db}), it is possible to reduce the set of detector tubes to be visited by applying a forward projection operation to the emission element b at every projection direction, $\theta_i, i = 1, ..., n$, where n stands for the number of possible projection directions given by the detector tubes configuration.

$$D' = \{F_{\theta_1}(b), ..., F_{\theta_n}(b)\} \tag{7.3}$$

where, $F_\theta(b)$ stands for the forward projection operator applied to emission element b at angle θ. Thus, the backward projection operation for emission element b will be

$$\sum_{d'} \frac{n_{d'b} R_{d'b}}{\widetilde{n}_{d'}}; \forall\ d' \in D'. \tag{7.4}$$

The previous procedure is depicted in Fig. 7.4 where continuous lines represent detector tubes in a reduced set D' and non-continuous lines are examples of detector tubes being discarded from set D'.

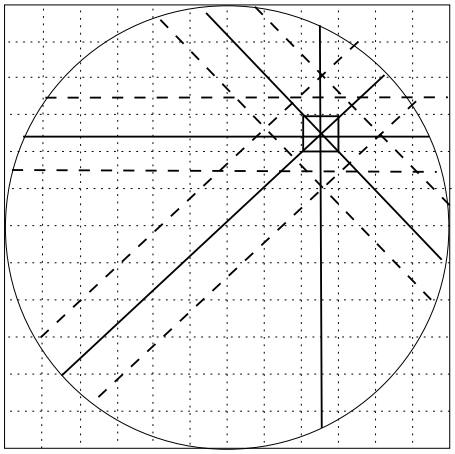

Figure 7.4: Reducing detector tube space in backward projection. Continuous lines represent the detector tubes that are being considered for the forward projection, while dashed lines will not be included in the forward projection step.

7.2.2 Dynamic case

In presence of motion, the emission elements contributing to a specific detector tube have to be added to the set of emission element given by the Bresenham's algorithm. Formerly, for detector tube d, the set B of emission elements to be considered during forward projection is:

$$B = Bresenham(d) \cup \bigcup_i P^i(d), i = 1, ..., N. \tag{7.5}$$

With

$$P^i(d) = \{b_j, \forall j / \exists\, b_k \in Bresenham(d) : b_j = \varphi_i^{-1}(b_k) \wedge l^i_{db_j} \neq 0\}. \tag{7.6}$$

Similarly, for the back-projection step the presence of motion is taken into account. For the dynamic case, Eq. (7.3) can be rewritten as:

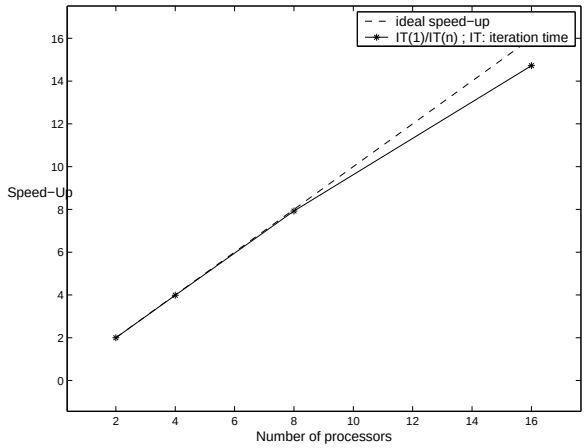

Figure 7.5: Reconstruction speed-up as a function of the number of processors.

$$D' = \bigcup_i [F_{\theta_1}(\varphi^i(b)), ..., F_{\theta_n}(\varphi^i(b))], i = 0, ..., N \tag{7.7}$$

with $\varphi^i(b)$ the transformation that gives the position of emission element b in motion state i.

7.3 Results

Image reconstruction with motion correction and two motion states was performed, the reconstructed image has size of 64x64x64 voxels and the projection matrix was of 64x64x64 elements. Image reconstruction as performed varying the number of processors to measure the speed-up. Fig. 7.5 shows the results.

Figure 7.6 presents a bar plot of time repartition for the principal inter-iteration tasks as communication master-slave, forward projection, backward projection and system matrix normalization.

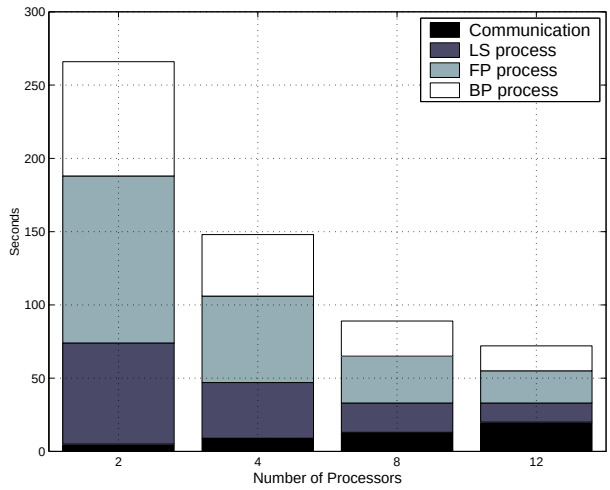

Figure 7.6: Time repartition for communication time, LS process (normalization term for each term of the matrix system), FP process (forward projection) and BP (backward projection) for a single iteration and as function of the number of slaves.

7.3.1 Discussion

Parallelization of the fully 3D MLEM algorithm was developed and acceleration schemes were presented. In this sense the Bresenham's algorithm, a classical algorithm in computer graphics, was successfully incorporated as an acceleration to the forward projection operations.

From Fig. 7.5, it can be noticed a nearly linear increment of speed with respect to the number of processors, with a speed-up reduction starting at eight processors.

It can be seen from Fig. 7.6 an increase in communications as more processors are used. This is expected since a synchronous communication type has been used. Furthermore, when more slaves are used, less time each process takes, but with the inconvenient that the communication time will increase.

In relation to the number of motion states used to describe motion, we found that the inclusion of a new state nearly duplicates the com-

putation times (75% of time increase), which is unfavorable if several motion states are required to obtain good motion corrected images.

Chapter 8

Method Evaluation

8.1 Introduction

The following sections describe how simulated data was created and how the respiratory motion technique was tested. Studies in phantom data were also performed and results are presented. Finally, patient data was used in a first approximation to apply the methodology in a clinical scenario.

8.2 Simulation Data

8.2.1 Materials and Methods

Main components used to simulate motion during an emission tomography study are presented below. Description of the simulated motions and specific simulation parameters will be given for each case.

The SimSET software

The *Simulation System for Emission Tomography* (SimSET) [117] is a software that simulates the process of emission tomography allowing the configuration of several components, going from the physical to the instrumentation process. Fig. 8.1 shows these components.

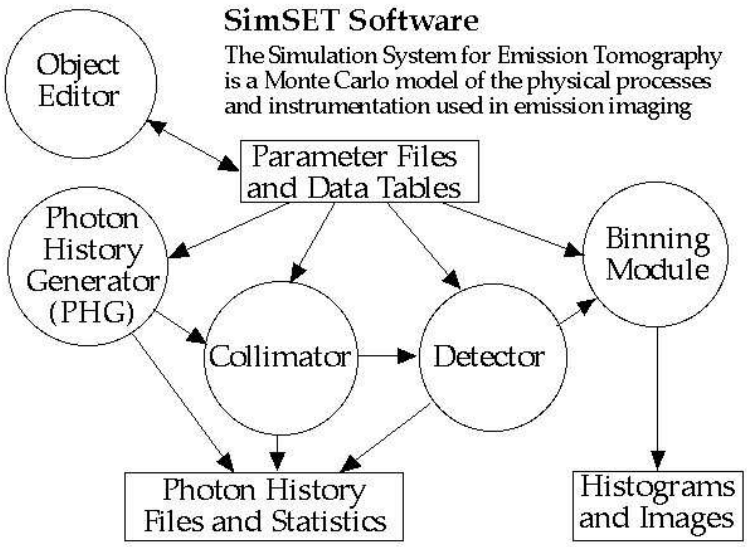

Figure 8.1: The SimSET library modules.

The principal modules are the *Object Editor*, which allows to generate activity and attenuation objects (using basic geometrical forms). The *Photon History Generator*, that creates and follows the photons through the different layers of the simulation. Finally, the tracked photons can be passed to the *Binning Module* which generates the sinogram data file (among others formats).

Through a command line it is possible to generate the activity and attenuation objects. In addition, the library has the flexibility to allow the use of pre-existing image data (e.g., phantoms). By means of a series of questions, SimSET collects the necessary information to read this data.

The *Photon History Generator* is configured using a text file, in which several options can be set, like number of decays to simulate, whether to simulate SPECT or PET, initial photon energy, simulation time, pointers to the already generated activity and attenuation files, effective field of view of the simulation etc. (see Appendix A.9 for an example of a configuration file). Once the configuration is done, the

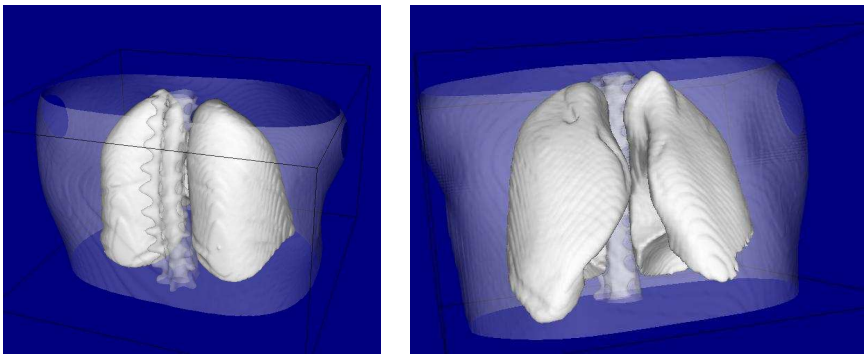

(a) Back view (b) Front view

Figure 8.2: The NCAT phantom. Thorax, lungs and spine are represented as isosurfaces.

simulation can be executed. Several features can be retrieved from the photons detected (e.g, binning according to energy level, binning according to scattering history, setting of format precision, etc.). For more details of the SimSET library, refer to [44, 117].

NCAT Phantom

In order to reproduce respiratory motion in emission tomography simulations, the NURBS-based cardiac torso (NCAT) phantom was used [101]. It is a model of the human thorax anatomy and physiology created primarily for the nuclear medicine imaging research. The fourth dimensionality of the phantom allows modelling of the heart beating and respiratory motion.

Similarly to SimSET, through a script file all the phantom parameters can be set easily, this allows to recreate different patient's specific conditions (see appendix A.10 for a example of this file).

The main interest of using the NCAT phantom was to model ET studies of the thorax when a breathing pattern is present (see Fig. 8.2). For this, different states within the breathing cycle were simulated and the individual images (used as activity images) were used as input data

for the SimSET library. Then, the obtained sinograms were combined to simulate movement during one single data acquisition.

Before presenting results from simulations with the NCAT phantom, simpler preliminary results are presented to show the reader the evolution of the study and how the methodology was tested from simpler to more complex dataset.

8.2.2 Synthetic 2-D Images

Methods

Synthetic images simulating a moving radioactive rod with a lesion-to-background of 10:1, 30 mm diameter were generated. First, an instantaneous simple translation of 32 mm was simulated in the y direction. For this, two motion states were generated (i.e reference and translated), which were used as activity images in a SimSET SPECT simulation. Table 8.1 presents the simulation parameters used for these experiments. The obtained sinograms were averaged to obtain a final sinogram which simulates an instantaneous translation of the radioactive rod. The motion transformation was then described as a single value of 32 mm in the y direction.

Image reconstruction with the MLEM algorithm was performed with the following parameters: ten iterations, reconstructed images of 128x128 pixels, and pixel size of 3x3 mm^2. No other corrections were considered.

A more realistic simulation consisted in linearly deforming the radioactive rod as illustrated in Fig. 8.3. This in order to better simulate the motions that one expect to find in the human thorax. The motion transformation φ that rules this deformation had the following form

$$\begin{aligned} \varphi(y) &= y_0 + k(y - y_0) \qquad \text{if } y \geq y_0 \\ \varphi(y) &= y \qquad \text{otherwise} \end{aligned}$$

Table 8.1: SIMSET simulation parameters for the moving (1) and deforming radioactive rod (2).

Modality	SPECT
Photon Energy	140.5 KeV
Minimum energy threshold	110.0 KeV
Acceptance angle	(±) 5.0 degrees
Number of decays to simulate	5e+6
Decay time	180 seconds
Total photons reaching the detector (1)/(2)	72703/73820
Total accepted photons (1)/(2)	54596/56306
Attenuation	none

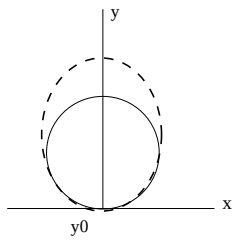

Figure 8.3: Linearly deforming a simulated radioactive rod. The attained deformation (dashed line) and the original object (continuous line).

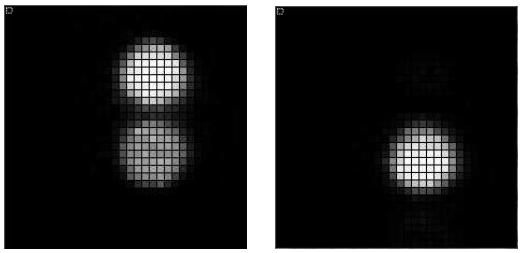

(a) Without motion correction (b) With motion correction

Figure 8.4: Reconstruction of a radioactive rod moved instantaneous without (a) and with motion correction (b).

For our experiment the parameters k and y_0 were set to $k = 1.8$ and $y_0 = 30$, and we use the simulation parameters of Tab. 8.1. The same approach as above (i.e generate activity images, then combine sinograms into a single one) was performed. The deformation was applied to the simulation process and used for correction. Image reconstruction was performed with the following parameters: ten iterations, reconstructed images of 128x128 pixels, and a pixel size of 3x3 mm^2. No other corrections were considered.

Results

For the translational motion, Fig. 8.4 shows the reconstruction obtained without motion correction (a), and with the proposed motion correction methodology (b).

Although the simulation is quite far from being realistic and representative of what the respiratory motion really is, it gives a first approach to the results that can be attained with the proposed methodology.

For the homothetic deformation, Fig. 8.5 shows the reconstruction obtained without (a) and with motion correction (b).

Fig. 8.5 shows how the deformation adds to the reconstructed image a fuzzy region in the upper border of the rod.

(a) Without motion correction (b) With motion correction (c) Image difference between reference and corrected images

Figure 8.5: Reconstruction of a linearly deforming radioactive rod without (a) and with motion correction (b). There is no noticeable difference between (b) and the reference, as denoted by their difference (c).

Discussion

These first 2-D experiments allow to qualitatively assess the behavior of the method, and to somehow validate the proof of concept. However, quantitative measurements were not included at this stage, and will be conducted in a 3-D context. Furthermore, although 2-D simulations are useful as a first approach to see the behavior of the methodology in basic cases, the lack of dimensionality with respect to the motions that actually occur within the thoracic cavity hinders a further validation of the methodology. The next section presents the results obtained in 3D simulations.

8.2.3 Synthetic 3-D Images

Methods

For the 3-D simulations, the NCAT phantom was used. A small sphere-shaped lesion of 15 mm diameter was added to it, with a lesion-to-background ratio of 8:1, Fig. 8.6 shows the activity image for the reference state.

(a) sagittal plane (b) axial plane (c) coronal plane

Figure 8.6: Sagittal, axial and coronal activity image planes of the reference state. The lesion is modelled as a sphere with a 15 mm diameter.

Table 8.2: SIMSET simulation parameters for 3-D NCAT simulations

Modality	SPECT
Photon Energy	140.5 KeV
Minimum energy threshold	110.0 KeV
Acceptance angle	(±) 5.0 degrees
Number of decays to simulate	50e+6
Decay time	180 seconds
Total photons reaching the detector	3.5e+6
Total accepted photons	2.9e+6
Attenuation	homogeneous

To simulate respiratory motion the simplified model (cf section 6.5.3) was used with a discretization, either varying between 2 and 6 states, or in 3 states describing inspiration, expiration and an intermediate state. Sinograms were then computed for each transformed state and combined into one single sinogram. Table 8.2 presents the simulation parameters used on these experiments.

The images were reconstructed with the MLEM algorithm without and with motion correction. Regularization was performed by means of iterative Gaussian filtering every 2 iterations with a full-width at

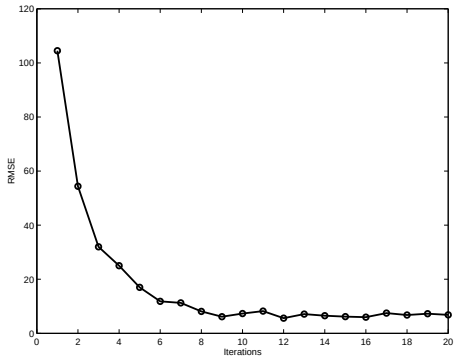

Figure 8.7: RMS error for the first twenty iterations. It can be noticed how the RMS values decrease drastically within the first iterations.

half maximum (FWHM) of 8.0 mm as in [73]. The stopping criteria for the MLEM algorithm was based in the marginal error between iterations with respect to the reference image. The threshold error value was set to 5%. However, more iterations were executed to visualize the stationary evolution of the measured error. After 20 iterations a stationary pattern was found (see Fig. 8.7). Finally, 10 iterations was selected to stop the iterations.

Attenuation was modelled from the reference image, i.e. the expiration state: the image is first smoothed with a Gaussian kernel, then thresholded so that its resolution resembles to the SPECT image, and finally given the lung attenuation coefficient supplied by the attenuation translation tables of SimSET. No other correction was included for the image reconstruction.

Motion correction was performed using the simplified model and attenuation correction was performed with the same attenuation map used in the simulation and the methodology explained in section 6.4.

The reconstructed 3-D images have a size of 128x128x128 voxels with a voxel size of 3x3x3 mm^3.

Two figures of merit were used to measure quantitatively the performance of the motion correction methodology, namely the coefficient

of variability (CV) and the contrast recovery (CR) [73], defined by

$$CV = \sigma(lesion)/\gamma(lesion). \tag{8.1}$$

where $\gamma(lesion)$ and $\sigma(lesion)$ denote, respectively, the average and the standard deviation of the intensity values over the lesion, and

$$CR = \gamma(lesion)/\gamma(background). \tag{8.2}$$

The computation of CR and CV involves a segmentation step of the lesion. This segmentation was performed by thresholding at a given percentage of the maximum intensity in the image. Such percentage was manually chosen and depends on the images to be segmented. For the simulation data this percentage was set to 60%, value that was found to better describe the lesion area.

To compute CR and CV, a region-of-interest (ROI) around the lesion has to be chosen. However, as we will compare two different images (reconstructed without and with motion correction), it is rigourously not possible to choose the same ROI in both, since the projection matrices are different. Then, to deal with this problem, we compute the CR and CV values in 3 different ROIs, and this will additionally allow to study the dependence of these values with respect to the ROI choice. The only criteria for the manual ROI selection was including the whole lesion volume.

A final concern was investigated on simulated data, which is related to the error introduced by the adaptation of the motion model into the patient anatomy (in this case the NCAT anatomy). Indeed, the matching between the respiratory motion model with the patient anatomy involves a step of affine registration (see Fig. 6.7). Our concern was to measure the influence of the errors introduced bythis step in the reconstructed images. The hypothesis is that an increase in volume due to an error in the registration step should produce a decrease in the mean intensity of the lesion activity, and conversely. To test this hypothesis, errors were introduced in the form of an affine transformation, which was applied to the adapted transformation of the simplified

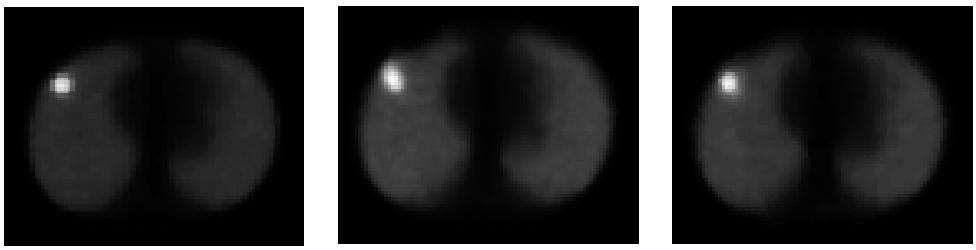

(a) Reference (b) Non-corrected (c) Corrected

Figure 8.8: Image reconstruction of reference frame (static) (a), without motion correction (b) and with motion correction (3 states used) (c).

model. The affine matrix has the following parameters:

$$\begin{pmatrix} 1+e & 0 & 0 & a \\ 0 & 1+f & 0 & 0 \\ 0 & b & 1+g & 0 \\ 0 & 0 & 0 & 1 \end{pmatrix} \tag{8.3}$$

For simulated data, three tests were carried out: varying only the parameter e, varying only the parameter b, and a combination of different variations of all parameters.

Results

Fig. 8.8 shows the reconstructed image with and without motion correction after 10 iterations of the MLEM algorithm. As described in the literature, the lesion appears larger in the non-corrected reconstruction.

A visual comparison of the intensity profiles allows to visualize the good agreement between the motion-corrected reconstruction and the ground truth. Fig. 8.9 presents the profiles after 20 iterations, but it can be observed that few modifications take place after 10 iterations.

To better assess the results, a qualitative study based on a fuzzy c-means segmentation of the lesion was performed (see [2] for more details). The parameters used for the fuzzy c-means segmentation are m-value=1.2, error-threshold=0.1, number-of-partitions=3, partition

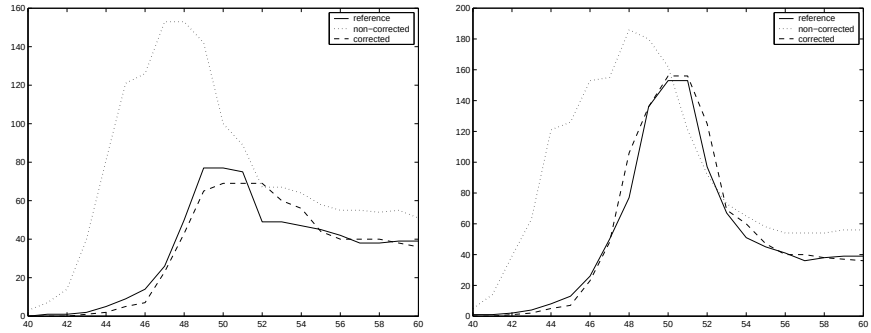

(a) x-coordinate: 34 (b) x-coordinate: 35

Figure 8.9: Intensity profiles for axial slice 43 around the lesion area. After 20 MLEM iterations the corrected profiles (dashed line) show a close relationship with the reference profiles (continuous line) in comparison with the non-corrected profile (dotted line).

centers=[5,50,150] representing the background, lungs and lesion activities (over an intensity scale 0-255). From the segmented images, isosurfaces were generated for the reference volume (i.e., expiration state) and for the non-corrected and corrected reconstructed volumes (see Fig. 8.10).

Concerning the quantitative measures, Fig. 8.11 presents the evolution for the CR values as the iterations proceeds (CV was found to be almost constant with respect to the iteration numbers), while Table 8.3 summarizes the CR and CV values obtained after ten iterations of the MLEM algorithm for the reference, non-corrected and corrected reconstructed images with respect to the chosen number of motion states (N) used for the image reconstruction.

Figure 8.12 shows the evolution of CR values corresponding to the non-corrected and corrected images for three different ROI's.

From Fig. 8.12, it can be noticed the different values obtained when using different ROIs. However, the real interest is to measure the differences in gain or increase between corrected and non-corrected CR values, which is the main objective of these measures. Fig. 8.13

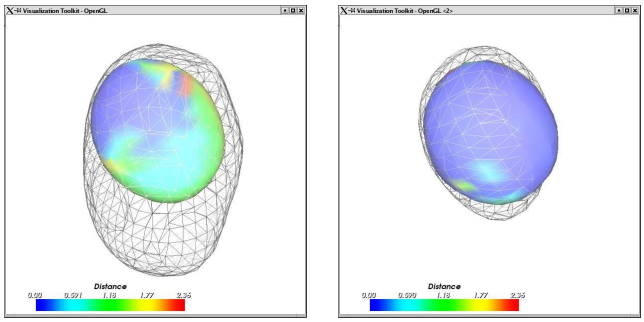

(a) Non-corrected (b) Corrected

Figure 8.10: Comparison of the reconstructed lesion volumes after 10 iterations. Without motion correction (a) and with motion correction (b) for the activity volume shown in Fig. 8.6. Isosurfaces extracted from reconstructed images are rendered in wire-frame, while the one extracted from the reference is colored. The color indicates the distance between the two displayed surfaces, *i.e.* an error between the reference lesion and the reconstructed one.

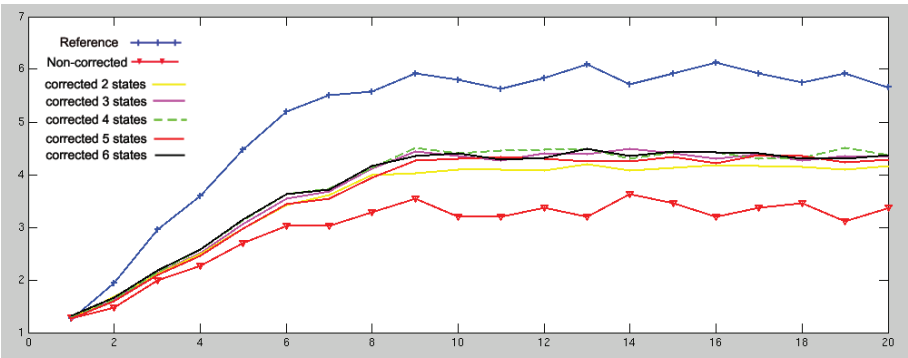

Figure 8.11: Evolution of CR values as a function of the number of iterations for the reference, non-corrected and corrected cases (from 2 to 6 motion states).

Table 8.3: Coefficient of variability (CV) and contrast recovery (CR) values for the reference, non-corrected and corrected reconstructions for different number of time states.

	Reference	**Non-corrected**	**Corrected**				
			N=2	**N=3**	**N=4**	**N=5**	**N=6**
CR	5.80	3.20	4.10	4.35	4.40	4.30	4.40
CV	0.14	0.13	0.14	0.14	0.13	0.14	0.13

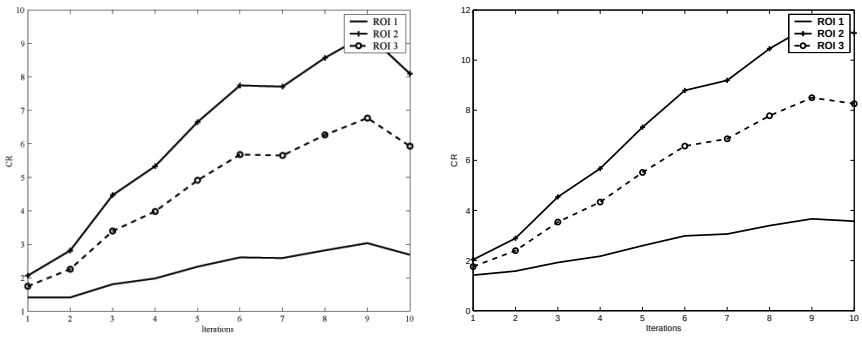

(a) Non-corrected CR values (b) Corrected CR values

Figure 8.12: Evolution of CR values as a function of the number of iterations for three different ROI. (a) CR values for the non-corrected case and (b) CR values for the corrected case.

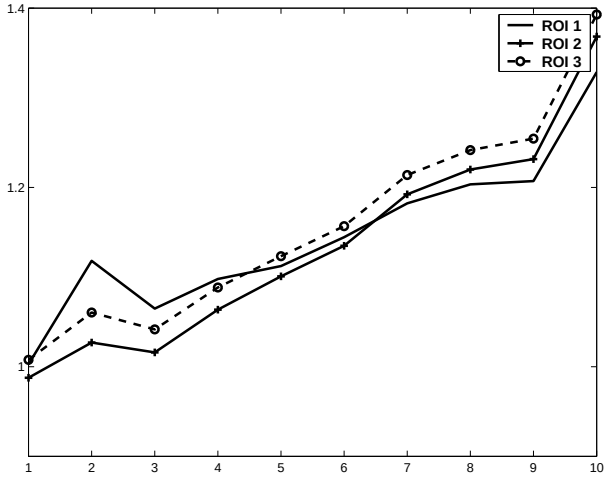

Figure 8.13: Evolution of CR rate values (corrected/non-corrected) as a function of the number of iterations for three different ROI.

presents the ratios between corrected and non-corrected CR values obtained for each ROI.

The measured relative volume error with respect to the reference image, was of 23.8%. After motion correction it decreased to 1%, with a centroid error before correction of 2.49 voxels (7.5 mm) and of 0.45 voxels (1.5 mm) after correction.

Motion correction was applied without considering voxel deforming as ellipsoids, but only displacements. In terms of volume error before correction with respect to the reference image, it was found an increase from 1% (considering deforming voxels) to a 5.36%. This result agrees with the analysis of the jacobian map performed in the lesion area, where an average factor of 1.06 was computed, meaning that the volume expansion in the region is on average of 6%.

Finally, it is of interest to visualize the volume evolution as the iterations proceed. Fig. 8.14 presents the volume rates between the corrected and reference images at each iteration.

The results obtained from introducing errors in the form of a "small"

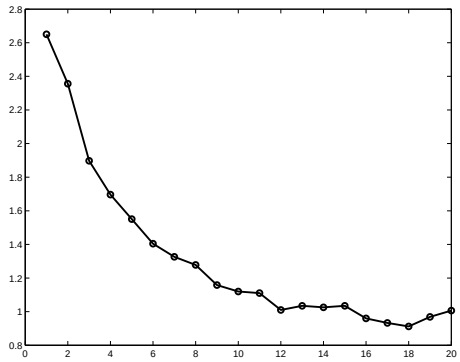

Figure 8.14: Volume ratio between corrected and reference volume as a function of the number of iterations.

affine transformation composed to the patient-to-model affine transformation are shown in Fig. 8.15.

Discussion

From Fig. 8.9, it can be noticed the good agreement between the reference and corrected profiles. It can also be noticed a non-corrected profile with higher maximum than the reference and corrected profiles. This is due to the fact that profiles were obtained from an axial slice near the border of the lesion. This allows to visualize the impact that motion can produce on profile analysis of images degraded by motion.

From Fig. 8.11, it can be noticed the expected stationary behavior after 10 iterations. Furthermore, the non-corrected images presents the lower CR values (red-inversed-triangles curve or lower curve), while the corrected cases (intermediate curves in the graph) show the improvement achieved by the motion correction methodology. Although no total correction of the CR value was attained (as comparing with respect to the reference curve in blue cross marks), the methodology improved the CR measures. Indeed, from the values shown in Table 8.3, it can be concluded that higher CR values are found for the corrected cases in comparison with the non-corrected one, with a 27±4%

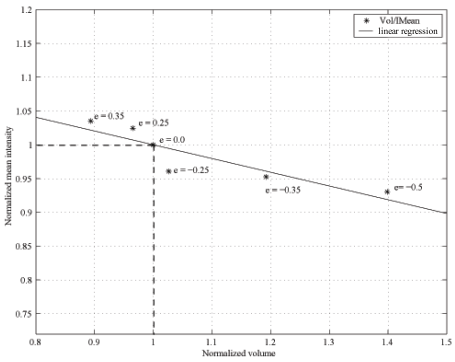

(a)

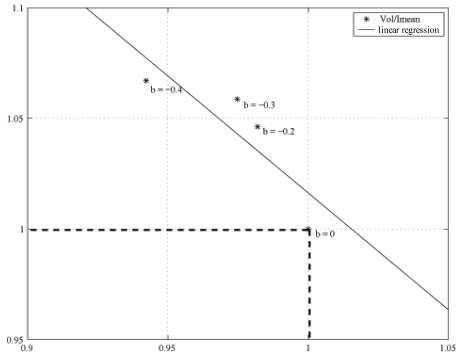

(b)

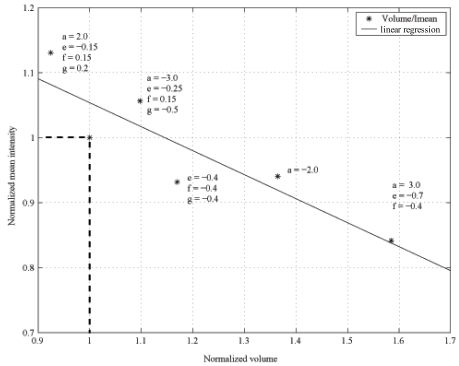

(c)

Figure 8.15: Testing the influence of the matching errors in the step of affine image registration. (see Fig.6.7). A known affine transformation was set with three different configurations of parameters (varying one parameter (a),(b), and a mixture of them (c)) and applied to the patient-to-model affine transformation. The plots show that an increase in volume produces a decrease in intensity. The dashed lines points the case with no error.

of increment, which demonstrates the deblurring effect of the motion correction. It can also be noticed from Fig. 8.14 that there is no relation between the number of iterations needed to reach a same CR value when using different numbers of motion states. Besides, it can be remarked that from a certain point onwards, an increment in the time sampling used to discretize the motion does not improve considerably the reconstruction.

From Fig. 8.13 it can be noticed that the rate values remain approximately the same regardless of the chosen ROI. This fact let us conclude that the selection of the ROI do not introduce biases to the analysis of results in terms of comparing the quantitative improvements the motion correction brings.

From Fig. 8.14, it can be noticed the volume decrease as the iterations proceeds. Furthermore, the convergence speed at which this volume change occurs change as well, passing from a high convergence at the first iterations to then arrive to a stationary point. However, the volume measurement are affected by the poor quality of the image at low iterations. Similarly to the CR value evolution (Fig. 8.11), no relation between the motion states and number of iterations was found. The hypothesis to this fact is that given a motion discretization that fairly describes the true motion, no acceleration on the motion correction will occur.

From Fig. 8.15 the expected inverse relation between lesion volume and mean intensity increase can be seen. However, due to the effects of noise in the reconstructed images, the points do not fall exactly in a line, but the tendency is clearly visualized.

8.3 Phantom Data

8.3.1 Materials and Methods

A phantom made of three spheres (like the one shown in Fig. 8.16) filled with 99mTc, having a concentration of 3145 MBq/ml each, 1.8, 3.2

Figure 8.16: Phantom device used to simulate moving spheres during data acquisition.

and 1.3 cm diameters, and volumes of 0.5 ml, 2 ml and 11.5 ml (inserts numbers 1, 2 and 3 respectively) was acquired with a Millenium-VG SPECT camera (see Table 8.4). This camera consists of two detectors revolving around the field-of-view (FOV). Each of the detectors is of dimensions 540x400x15.8 mm^3. The scanner is capable of producing data in limited angle 3-D mode, (with axial lead septas mounted) and in full 3-D mode, (without the led septas). The experiments presented here were acquired in limited 3-D mode (commonly used for lungs and abdomen studies). Five data acquisitions were performed, and between two successive acquisitions, the phantom was translated 1 cm in the axial direction of the scanner system (see Table 8.5). By summing the sinograms, it is possible to simulate data acquisition of a moving phantom. One single acquisition of duration five times longer was performed in the reference position, to serve as ground truth.

The motion transformation was then formed as a linear displacement in the axial direction with a maximal amplitude of 4 cm. The motion transformation was discretized in two (translations of 0 and 4 cm), and five states (translations of 0, 1, 2, 3 and 4 cm) to test the motion correction technique.

Table 8.4: Acquisition protocol for the phantom experiments.

Camera	Millenium VG
Collimator	Parallel (LEHR)
Acquisition	Tomographic CDET
Matrix	128x128
Energy window	(140 ± 10) keV
Angular sampling	120 steps of 3° over 360°

Table 8.5: Experimental protocol for the moving phantom experiments.

Acquisition Number	1	2	3	4	5	6
Position (cm)	x_0	x_0	x_0+1cm	x_0+2cm	x_0+3cm	x_0+4cm
Acquisition time	10mn	50mn	11mn	11mn	12mn	12mn

The reconstructed volumes had dimensions 128x128x128 voxels with a voxel size of 4.42x4.42x4.42 mm^3.

Following the same analysis used for the 3D synthetic simulations, ten MLEM iterations was found to be a good point to stop the iterations. Gaussian regularization every 2 iterations with a full-width at half maximum (FWHM) of 8.0mm were set as main parameters. No other correction factors were incorporated to the reconstruction.

Quantitative measures were performed for each insert on the reconstructed images. Volume, CR, and CV measurements were calculated to assess the quality of the proposed motion correction in phantom data. Besides, intensity and root mean square error profiles were generated as well as a function of the number of iterations and number of motion states.

Volume-Error-Non-Corrected (VE_{nc}) and Volume-Error-Corrected (VE_c) were defined as the relative error between the reference and non-corrected volumes and between the reference and corrected volumes, respectively. The volumes were computed on a volume-of-interest (VOI)

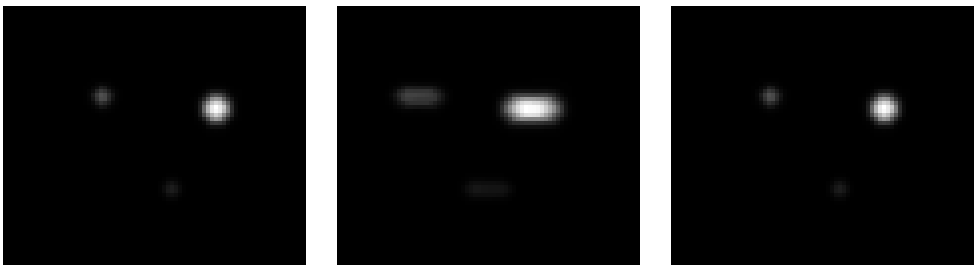

(a) Reference (b) Non-corrected (c) Corrected

Figure 8.17: Effect of discrete axial translations of sphere sources during an ET study. Reference (a), without motion correction (b) and after motion correction (5 motion states) (c).

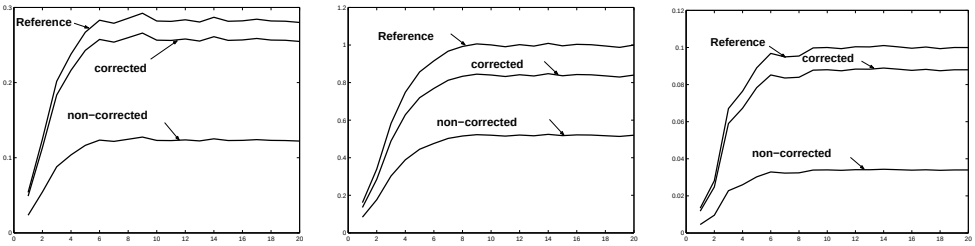

(a) Insert 1 (b) Insert 2 (c) Insert 3

Figure 8.18: CR values as a function of the number of iterations for each insert of the phantom.

selected with a threshold value set at 70% of maximum. Finally, Centroid Error Non-Corrected (CE_{nc}) and Centroid Error Corrected (CE_c) were computed. These are defined as the distance between reference and non-corrected centroids and between reference and corrected centroids respectively.

8.3.2 Results

Figure 8.17 shows the reference, corrected (5 motion states) and non-corrected reconstructed volumes.

Quantitative measures are plotted as a function of the number of iterations. Fig. 8.18 presents the results obtained for the CR values.

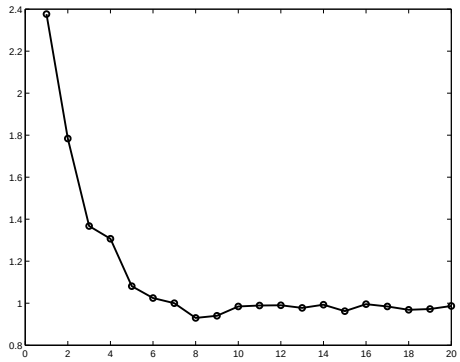

Figure 8.19: Volume ratio between corrected and reference volume of insert number two as a function of the number of iterations.

Table 8.6: Results of motion correction for phantom data.

Insert	VE_{nc}	VE_c	CE_{nc} (cm)	CE_c (cm)	CR_{nc}	CR_c	CV_{nc}	CV_c
1	350%	5.8%	2.0	0.16	41%	91%	184%	107%
2	125%	1%	1.96	0.21	52%	84%	124%	110%
3	166%	8%	1.85	0.21	34%	88%	214%	103%

To measure the evolution on the volume correction with respect to the reference image, volume ratios between the corrected and reference volumes were computed on each insert and at each iteration. Fig. 8.19 shows the case of insert number two to illustrate the common behavior found on the three inserts.

Table 8.6 summarizes after ten MLEM iterations, the obtained CR and CV measures for the non-corrected (CR_{nc}, CV_{nc}) and corrected (CR_c, CV_c) images, these values are expressed as percentages with respect to the reference image (e.g. a CR value of 50% represents half the CR value obtained for the reference image).

Concerning the impact of the number of motion states chosen to perform motion correction, intensity profiles and RMSE values were computed for each axial slice within the hot spot volume for different numbers of time states (see Fig. 8.20).

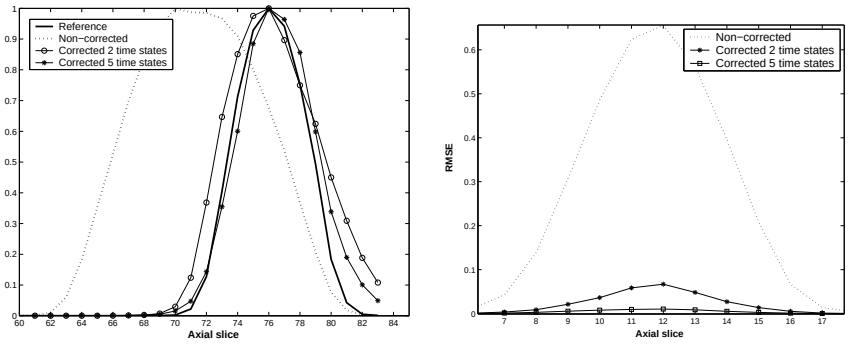

(a) Intensity profiles (b) RMSE error

Figure 8.20: Intensities profiles of reference, non-corrected and corrected volumes of insert number two for different number of time states (a) and root-mean-square errors for each slice in the hot spot volume for the non-corrected and corrected reconstructed images (b).

8.3.3 Discussion

From Fig. 8.18 it can be noticed the improvement on the CR values on each insert. An irregular pattern during the first iterations appears in Fig. 8.18(c), which corresponds to the third insert. This irregularity could be caused by errors on segmenting this insert, since a correct Segmentation is more difficult to obtain due to the lower intensity of this insert.

During the step of image reconstruction, the CV values were found to remain nearly constant or with small reductions, which would be caused by a lesser influence of the motion correction on the reconstructed images, this effect being amplyfied by the stronger influence of the Gaussian regularization on noise reduction. On the other hand no increase of CV values were found during experimentation. Further research is needed to clarify this point.

From Fig. 8.19 it can be noticed how the volume evolves towards the reference image. Starting with a higher volume in the first iterations (corresponding to the one on the non-corrected case), to then reach the

reference volume (i.e. corrected-volume/reference-volume=1.0). The plot in Fig. 8.19 allows to conclude that the convergence speed of the motion correction follows a similar pattern found on MLEM iterations, where fast convergence is attained at the first iterations to then reach a steady state (i.e. convergence) from where if the iterations continue further more, noise start to be included into the reconstructed images, situation that did not arrived in our experiments since the algorithm was stopped before. For the two other inserts the behavior was found to be similar, much in the same way as the evolution of the CR values found for each insert (Fig. 8.18).

It can be seen from Table 8.6 and Fig. 8.20 that the motion correction method compensates for volume size and position of the spheres. From Table 8.6 it can also be noticed an improvement in both figures of merit which indicates an improvement in the spatial distribution of intensities.

As a first approach to real data, the results obtained in phantom data are encouraging. For the three radioactive spheres, good qualitative and quantitative results were obtained. However, it must be considered the simplicity of the simulated motion, which only consisted in a simple translation. Efforts were put to add complexity to the motion without further success due to the complexity of the task.

During experimentation, visual inspection of CR and volume curves for each insert allowed to conclude that no correlation between the sphere size and the motion correction exist. For each measure, around iteration number eight a stationary state was found. If one consider the fact that the motion model is designed to operate on voxel-wise basis, the only expected constraints on this sense come from the resolution characteristics of the acquisition system.

Table 8.7: Data acquisition protocol for the patient data used.

Camera	Millenium VG option Hawkeye (GEMS)
Crystal width	16 mm
Field of View (FOV)	(50x40)cm
Acquisition matrix	128x128
Photopic-compton energy window	(132-321)keV
Photopic-photopic energy window	511 keV ± 10%
Acceptance angle	8°
Tomographic acquisition mode	CDET, continuous heads rotation
Rotation speed	3 mn/cycle
Acquisition time	30 mn

8.4 Patient Data

8.4.1 Materials and Methods

Five patients having one lesion each, underwent dual-head coincidence gamma camera scanning (CDET) (see Table 8.7). The projection data was used to test the methodology of motion correction presented in chapter 6. Fig. 8.21 shows approximative positions of each lesion labelled according to Table 8.8 which summarizes, if available, the lesion position, CT and post-surgery lesion sizes. In addition, for each patient data, the attenuation CT image acquired during the same session was available and used for posterior attenuation correction.

Estimation of respiratory motion was applied to the five patients using the simplified model obtained from a single subject and using the statistical models STAT-1 and STAT-2.

For each patient in Table 8.8, 3D image reconstruction with and without motion correction was performed. The same stop criterion used previously for the simulated and phantom data was used for the patient data. As a result, the algorithm was stopped after 20 iterations for both corrected and non-corrected cases. Discretization in

Table 8.8: patient database summary for respiratory motion correction tests.

Patient N°	Position	CT diameter (mm)	Surgical diameter (mm)
1	Left superior	60	80
2	Left medium	-	40
3	Right medium	16	-
4	Right inferior	28	-
5	Right superior	-	37

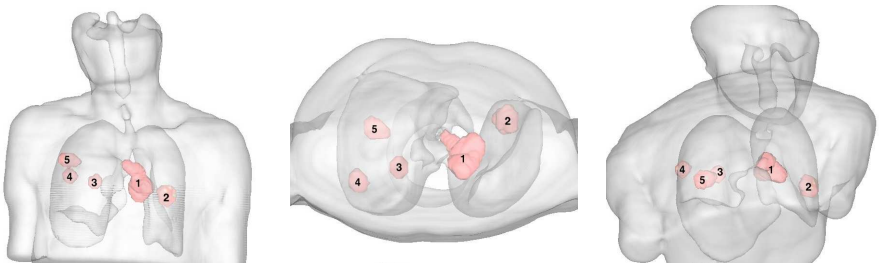

(a) (b) (c)

Figure 8.21: Approximative lesions positions for the five patients. Numeric labels correspond to the patient numbers in Table 8.8.

three motion states, Gaussian regularization with filter full-width at half maximum (FWHM) of 8.5 mm every three iterations were set as main parameters. The reconstructed images dimensions are 128^3 with a voxel size of 4x4x4 mm. Attenuation correction was performed according to the methodology explained in section 6.4. To facilitate computations we assumed that this attenuation map corresponded to the reference motion state (i.e. expiration state). This approximation could be further obviated if the attenuation map is acquired beforehand at the reference state used or if motion correction is applied to it to bring the image to the desired respiratory motion state (e.g. [9]).

As for the phantom experiments, quantitative measurement were computed. To obtain CR, volume and CV values, manual segmentation with a threshold at 70% of maximum was set initially. This value was then manually adjusted for every case (but the same for non-corrected and corrected images) in order to improve the segmentation. In addition, centroid displacements were computed in order to visualize the preferred displacement directions.

8.4.2 Results

For each patient, volume changes were computed for the non-corrected and corrected images using each motion transformation (i.e. simplified model, STAT-1 and STAT-2). For each patient, the observed volume changes were found to be quasi-stationary with respect to the non-corrected case (i.e. little volume decrease was observed in some patient data after correction). Thus, for visualization purposes, the second case is presented, which corresponded to the case with the largest volume reduction.

In terms of CR values, Fig. 8.23 to Fig. 8.27 show the evolution of the CR values as a function of the iterations obtained for the simplified model and statistical models STAT-1 and STAT-2. The CV values were found to remain fairly constant during the iterations. However, no increase of the CV values was found.

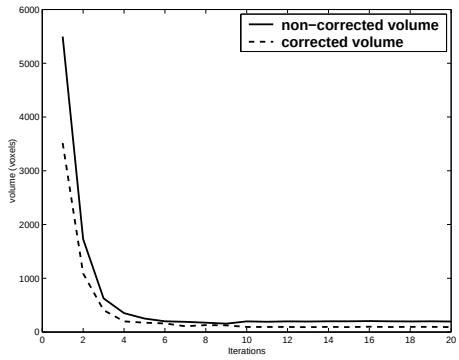

(a) Simplified model

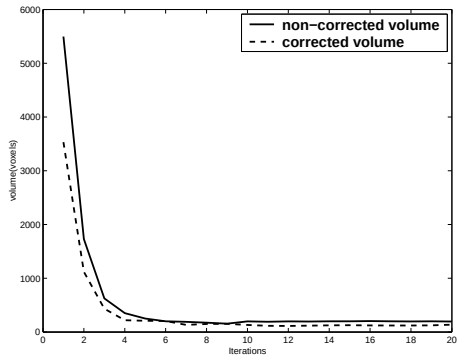

(b) STAT-1

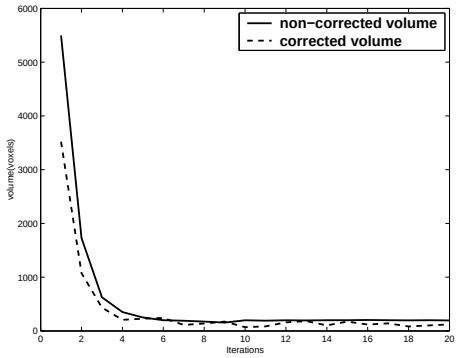

(c) STAT-2

Figure 8.22: Volume changes as a function of iterations for patient number two. (a) Simplified model, (b) Statistical model STAT-1, and (c) Statistical model STAT-2.

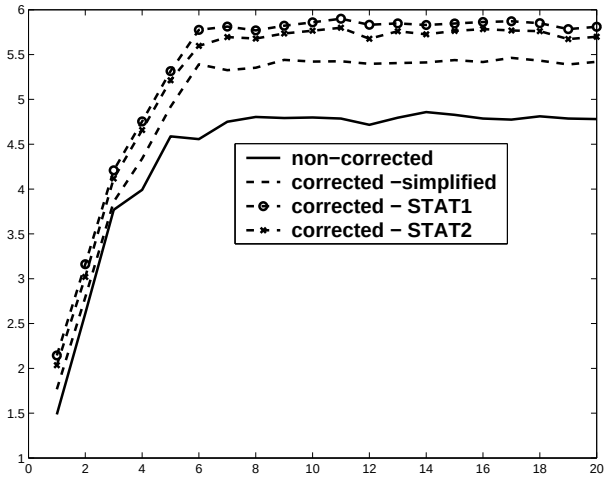

Figure 8.23: CR values as a function of iterations for patient number one. Results corresponding to the Simplified model, Statistical model STAT-1, and Statistical model STAT-2 are presented.

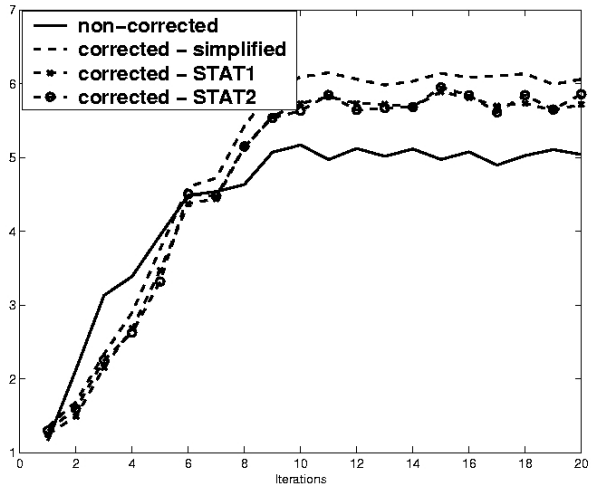

Figure 8.24: CR values as a function of iterations for patient number two. Results corresponding to the Simplified model, Statistical model STAT-1, and Statistical model STAT-2 are presented.

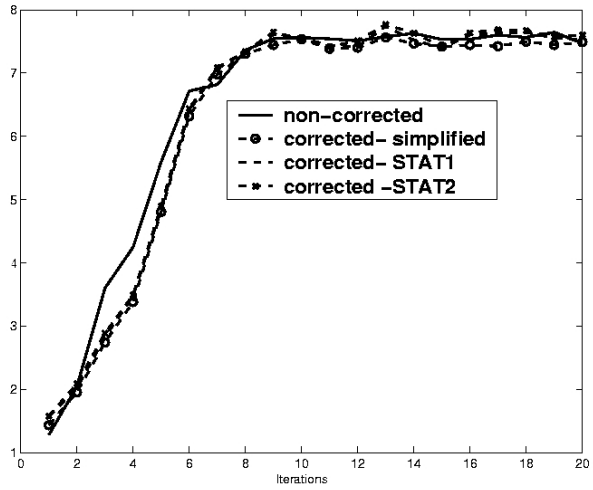

Figure 8.25: CR values as a function of iterations for patient number three. Results corresponding to the Simplified model, Statistical model STAT-1, and Statistical model STAT-2 are presented.

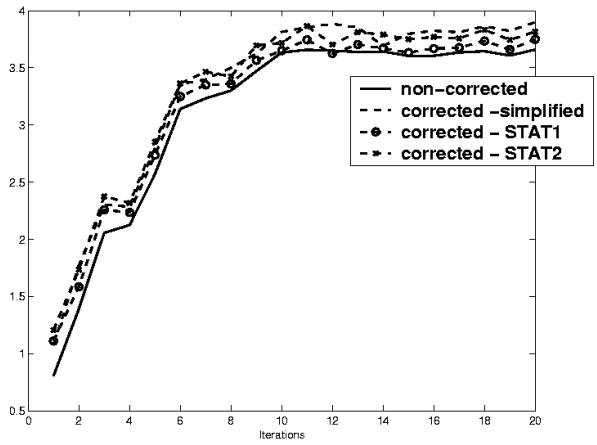

Figure 8.26: CR values as a function of iterations for patient number four. Results corresponding to the Simplified model, Statistical model STAT-1, and Statistical model STAT-2 are presented.

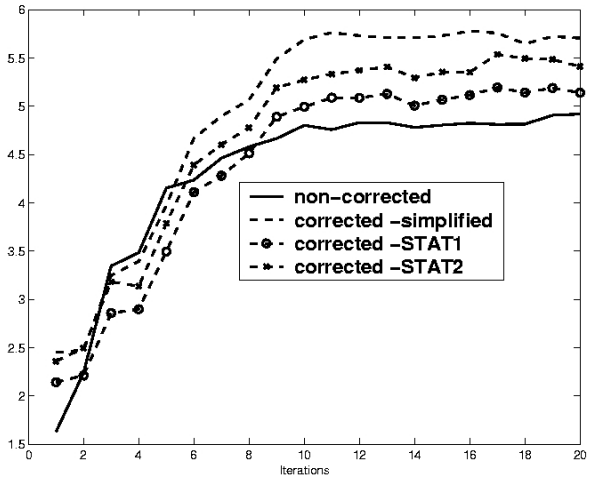

Figure 8.27: CR values as a function of iterations for patient number five. Results corresponding to the Simplified model, Statistical model STAT-1, and Statistical model STAT-2 are presented.

Table 8.9 summarizes the results obtained for the simplified respiratory model,in terms of lesion volume (normalized with respect to the non-corrected case), contrast recovery (CR), coefficient of variability (CV) for the non-corrected (NC) and corrected (C) case, and lesion's centroid displacements in the cranial-caudal (CC), anterior-posterior (AP) and lateral (LR) directions. Table 8.10 and Table 8.11 present the results obtained by using the statistical respiratory model STAT-1 and STAT-2 respectively.

Figures 8.28 to 8.32 show for each patient, coronal, sagittal and axial slices for the non-corrected case, corrected case using the statistical respiratory motion model and a fusion of the non-corrected and corrected contour obtained with a threshold of 70% of maximum.

8.4.3 Discussion

From the results presented in Table 8.9, Table 8.10 and Table 8.11, a reduction in the lesions volume after motion correction can be noticed.

Table 8.9: Results of motion correction for patients in Table 8.8 using the simplified respiratory model.

Patient	**Volume**	**Displacement (mm)**			**CR**		**CV**	
	(C/NC)	LR	AP	CC	NC	C	NC	C
1	0.95	2.00	3.20	3.20	4.78	5.42	0.22	0.23
2	0.64	2.60	3.60	5.10	5.04	6.06	0.24	0.20
3	0.98	0.30	2.62	4.23	7.47	7.49	0.26	0.22
4	0.86	0.45	1.20	1.74	3.66	3.90	0.18	0.16
5	0.77	2.50	0.60	2.33	4.92	5.70	0.09	0.09

Table 8.10: Results of motion correction for patients in Table 8.8 using the statistical respiratory model STAT-1.

Patient	**Volume**	**Displacement (mm)**			**CR**		**CV**	
	(C/NC)	LR	AP	CC	NC	C	NC	C
1	0.91	0.85	2.80	3.00	4.78	5.81	0.22	0.20
2	0.75	2.15	2.80	4.25	5.04	5.72	0.24	0.24
3	0.96	0.35	2.50	4.10	7.47	7.53	0.26	0.21
4	0.90	0.40	1.45	1.50	3.66	3.75	0.18	0.16
5	0.84	1.55	1.20	1.95	4.92	5.35	0.09	0.10

Table 8.11: Results of motion correction for patients in Table 8.8 using the statistical respiratory model STAT-2.

Patient	**Volume**	**Displacement (mm)**			**CR**		**CV**	
	(C/NC)	LR	AP	CC	NC	C	NC	C
1	0.93	1.05	2.60	3.21	4.78	5.69	0.22	0.20
2	0.78	1.95	2.85	4.15	5.04	5.60	0.24	0.22
3	0.92	0.41	2.70	4.23	7.47	7.60	0.26	0.24
4	0.88	0.36	1.23	1.50	3.66	3.81	0.18	0.15
5	0.81	1.68	1.32	1.95	4.92	5.41	0.09	0.12

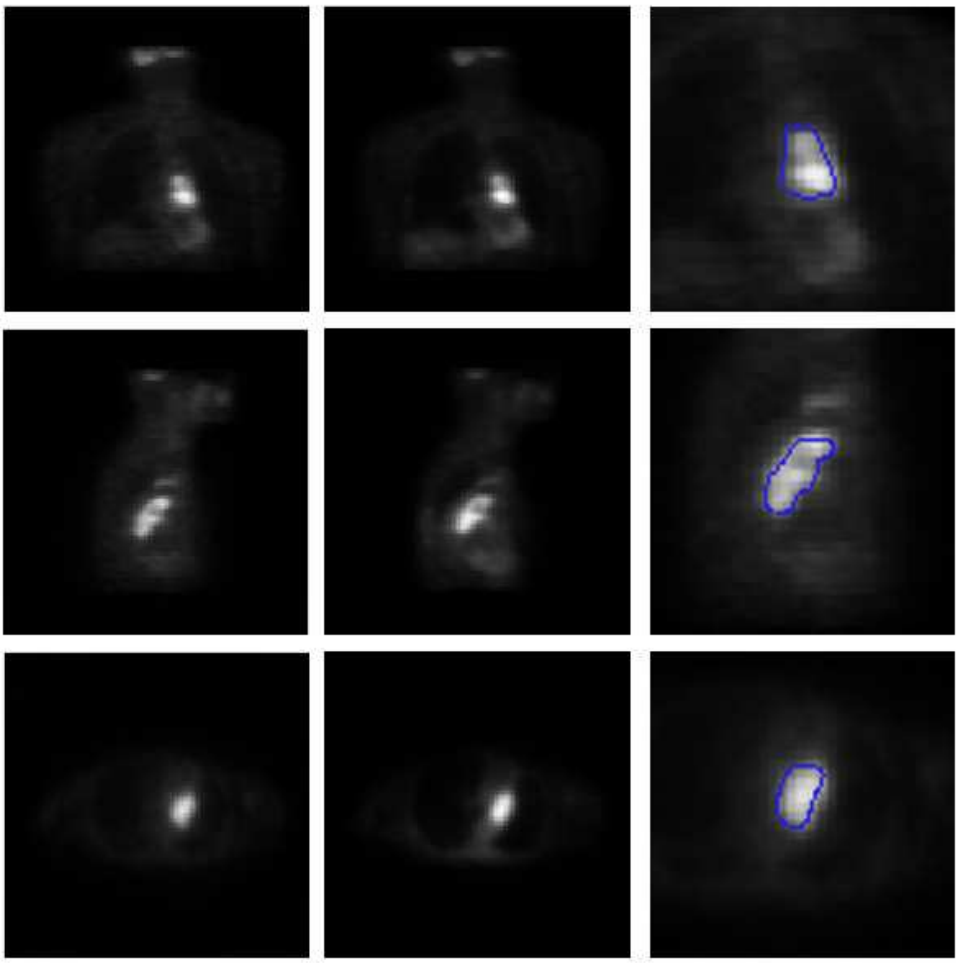

Figure 8.28: Coronal, sagittal and axial slices for patient number one without motion correction (left column), with motion correction using the statistical motion model (central column), and a zoom of both, the region of interest of the non-corrected image and the motion-corrected contour (right column).

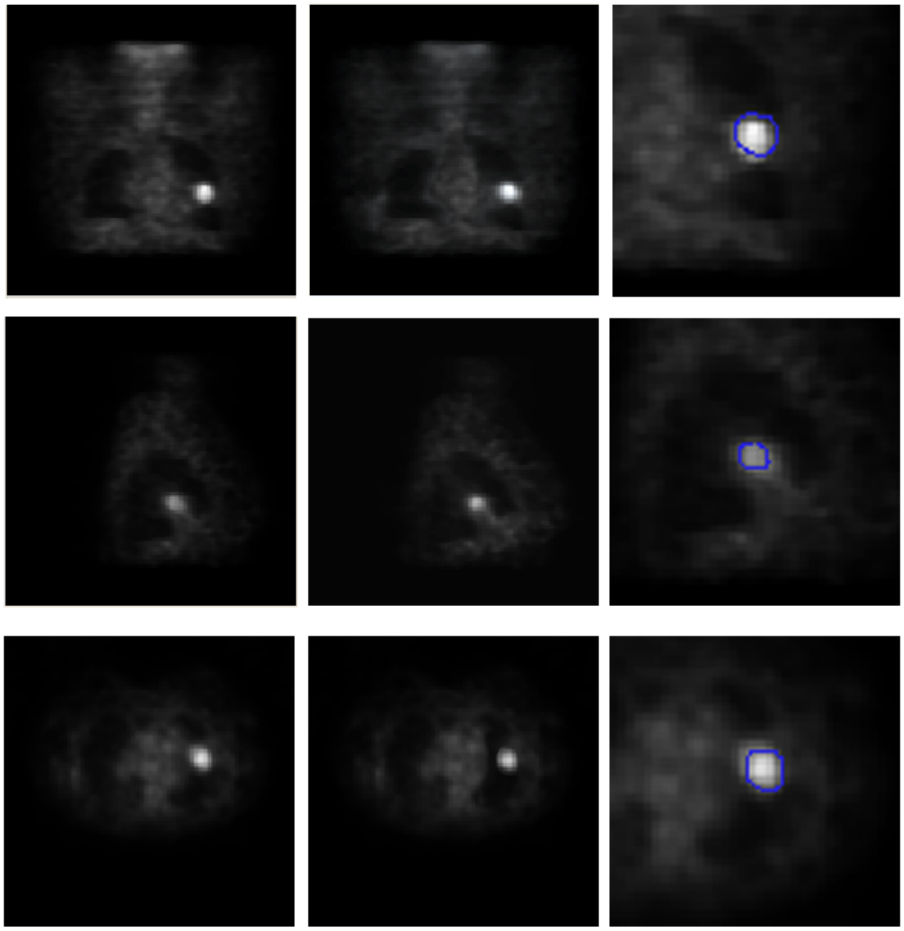

Figure 8.29: Coronal, sagittal and axial slices for patient number two without motion correction (left column), with motion correction using the statistical motion model (central column), and a zoom of both, the region of interest of the non-corrected image and the motion-corrected contour (right column).

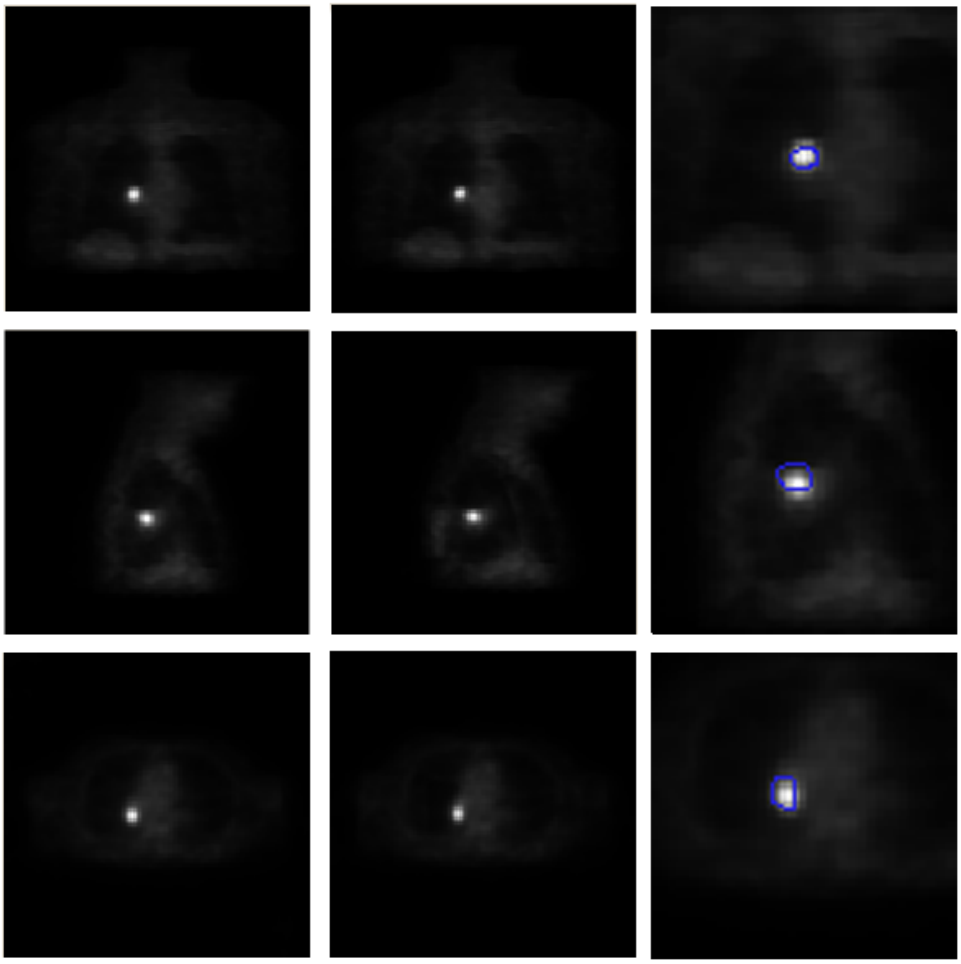

Figure 8.30: Coronal, sagittal and axial slices for patient number three without motion correction (left column), with motion correction using the statistical motion model (central column), and a zoom of both, the region of interest of the non-corrected image and the motion-corrected contour (right column).

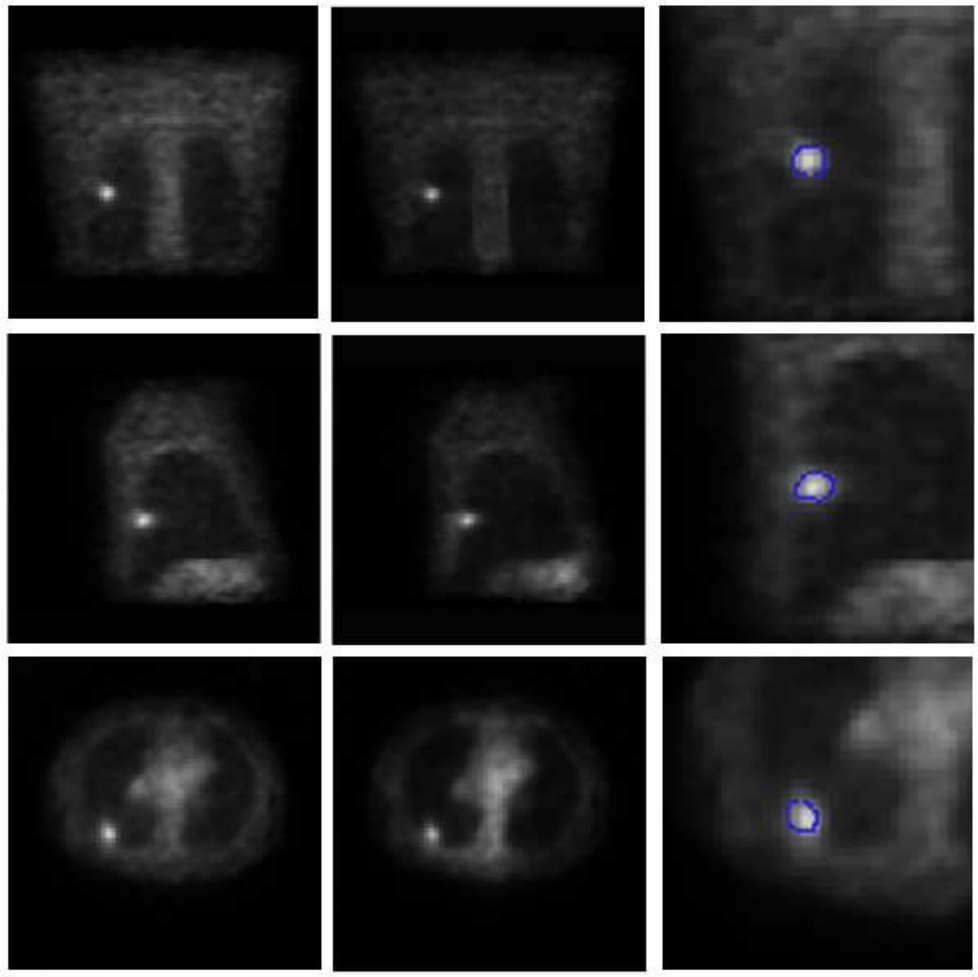

Figure 8.31: Coronal, sagittal and axial slices for patient number four without motion correction (left column), with motion correction using the statistical motion model (central column), and a zoom of both, the region of interest of the non-corrected image and the motion-corrected contour (right column).

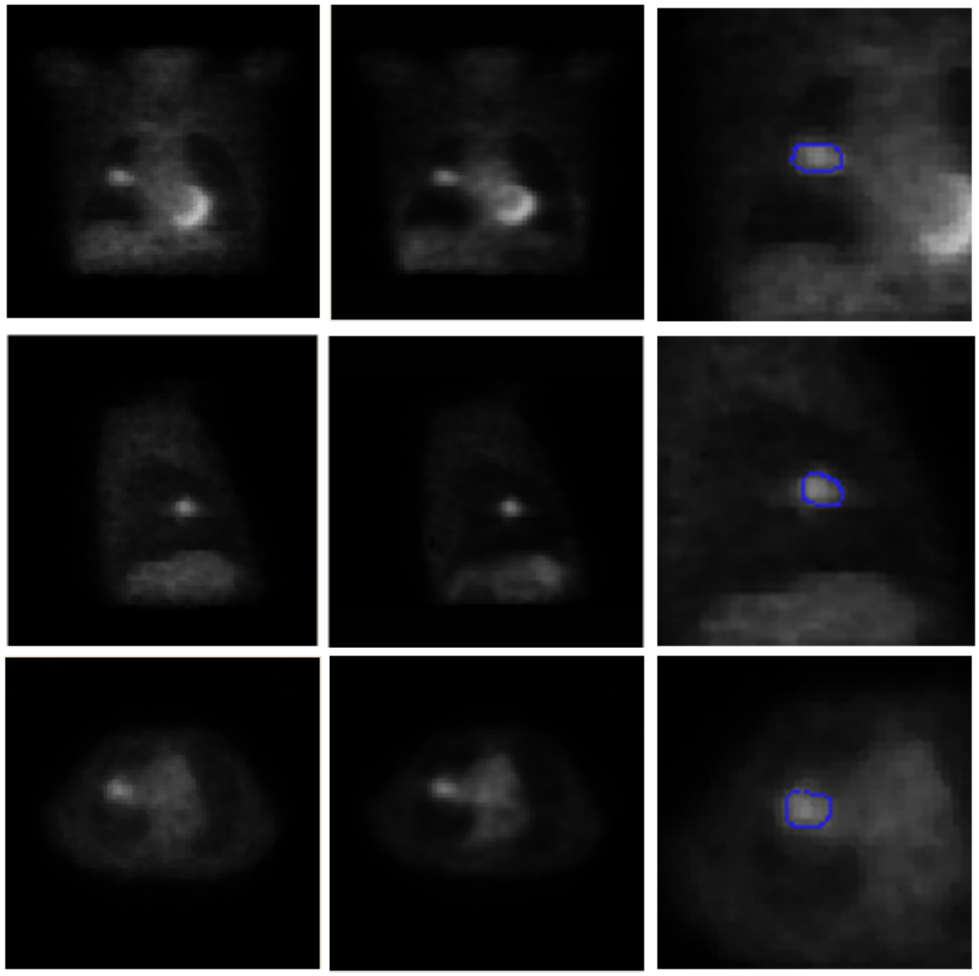

Figure 8.32: Coronal, sagittal and axial slices for patient number five without motion correction (left column), with motion correction using the statistical motion model (central column), and a zoom of both, the region of interest of the non-corrected image and the motion-corrected contour (right column).

In terms of displacements of the lesion's centroids, the cranial-caudal direction presents the maximal displacements, while the lateral direction presents the smaller ones, a fact that agrees with the findings in lung lesions displacements of Seppenwoolde and colleagues [102]. The lesion in the patient number four experiences the smallest global displacement, which is attributed to its position near the back of the thorax, where displacements are found to be minimal. On the other hand, the lesion in patient number two experiences the largest motion in the cranial-caudal direction and the largest change in volume. This is expected to happen due to the position of the lesion, where rigid structures are not expected to be attached to it (see Fig. 8.21). Quantitative measures indicate improvements in contrast after motion correction, which encourages the fact that the proposed method could contribute as a way of compensating the blurring effects in the lesion area and its spatial activity distribution. It must be noticed that these measurements were performed by segmenting the lesions with a thresholding technique, which would require further development in order to improve the quality of the segmentation.

Comparing corresponding values in Table 8.9 and Table 8.10 and Table 8.10, one can notice small variations between the results obtained between the respiratory models. This indicates the good agreement between the simplified respiratory model and the statistical ones from the dataset composed by ten subjects. However, a statistical model presents itself as a more robust model, and always should be preferred over the simplified one. An other issue related to these results is the fact that the dataset mostly presents lesions situated in regions of low motion activity. A larger dataset, which consider lesions situated in regions of higher motion activity (e.g. bottom of lungs), would present itself as a better test in terms of motion correction.

These results remain in a exploratory phase since the lack of a ground truth hinders its validation and so conclusions drawn from such results must stay as part of hypothesis to be proven. We claim how-

ever, that in the absence of external respiratory tracking devices, and provided an adequate motion transformation of the patient, satisfactory results could be obtained. The next chapter discusses more about the improvements in this area through the use of new 4-D CT scans imbedded in ET cameras.

Chapter 9

Conclusions and Perspectives

9.1 General Conclusions

Along this thesis, discussion has been given in each chapter, pointing out the more important concepts and remarks that, according to our belief, merited further commentaries. In this final chapter, we are interested on summing up some of these points and to present the reader some final words concerning the perspectives, we believe would of interest as part of future work.

9.1.1 Respiratory motion in emission tomography studies

In emission tomography, the current long acquisition times (compared to those of other medical imaging modalities) hinder the obtention of images free of artifacts caused by patient motion. In this thesis work, emphasis on lung tumors has been given. The spatial blurring produced by respiratory motion leads to errors in quantitation, inter-modality image registration, diagnostic, therapy, follow up of disease, etc. Thus, the task of correcting images distorted by motion and more specifically, respiratory motion, is of great importance and it has cleared signaled as something to be considered.

Previous efforts of solving this problem have arisen with the idea

of neglecting information not corresponding to the same physiological state or patient position, which in the case of respiratory motion is given by the same phase of the breathing cycle, or by correcting or transforming the distorted data so it represents a same phase of the breathing cycle or same patient position.

9.1.2 Designing a respiratory motion correction methodology; initial assumptions

The proposed method results from an effort to compensate the effects produced by motion during the step of image reconstruction. Its conception follow the strong and challenging considerations of not having access to further information but the projection data itself. Indeed, compared to the ideal situation where respiratory motion information can be retrieved directly from the patient, the constraint imposed by the current available instrumentation, yields the problem of motion correction a very difficult task.

In this thesis, under the mentioned considerations, an approximative model-based motion compensation method was developed as an effort to improve emission tomography images degraded by motion. As mentioned, such constraints make difficult the task of motion correction. On the other hand, the retrospective motion correction feature of the proposed method, that is to say, its ability to process existent patient data in which no tracking device was used, presents itself as an advantage over methods requiring on-site settings of the data acquisition system or the presence of external devices. This feature was already signaled along this thesis, however, it is signaled one more time since we believe that it presents the stronger and more advantageous feature over other techniques.

Two major aspects of the proposed method, deserving further discussion, are next presented.

9.1.3 Motion correction as part of the reconstruction algorithm

In some way, the problems encountered due to the lack of respiratory motion information of the patient hinder the evaluation of the motion correction itself. Below, some points are given concerning the features we believe have to be highlighted.

Among the main advantages of integrating the step of motion correction into the image reconstruction algorithm, it can be first mentioned the compactness of the technique. That is to say, the good integration of the motion correction into the image reconstruction algorithm, through the inclusion of motion information in the computation of the projection matrix terms. The interaction given by the probability terms between projections (known information) and emission elements (whose activity distribution we search), and the fact that this probability can be expressed in terms of geometrical considerations, play an excellent role in the task of correcting motion within the image reconstruction algorithm.

Other advantage of including motion information into the image reconstruction algorithm was noticed to be the "transparency" between the chosen motion model and the motion correction itself. Indeed, the good integration of the motion correction into the image reconstruction algorithm allows to avoid further adaptations of the motion correction technique to specific motion models. Conversely, such feature permits the integration of different motion models, which can be selected, for example, according to the degree of motion correction precision one searches. On the other hand, such strong link between the image reconstruction algorithm and the motion correction method produces a dependence in terms of the type of image reconstruction one can select. Such constraint can be further relaxed if one considers the vast family of algorithms based on the concept of projection matrix, on which the motion correction takes place.

Already mentioned is the concept of modelling voxels as spheres

that deform into ellipsoids under deformation. Up to our knowledge this feature corresponds to a new proposal to deal with the non-linear deformations occurred in the thorax due to respiration. Besides, under these deformations, this modelling is better adapted to compute detection probabilities than using cubic voxels and classical methods of computing intersections between these cubic voxels and detector tubes.

A final little observation that can be added to this discussion, is the fact that although the motion correction was designed under the framework of respiratory motion correction, its independence from the type of motion to be corrected (i.e. discrete, continuous, periodic, etc.) allows motion correction produced not only by respiration.

9.1.4 Single-subject based and population-based respiratory motion modelling

The hardest aspect of this thesis was the development of a respiratory motion-model that does not consider patient-specific information.

In the case of not having access to tracking devices, current methods consist in making an estimation of the motion or just assume the existence of such. In this thesis, three approaches were developed as an effort to compensate for motion under the strong initial conditions, which as mentioned before, render the motion correction problem as a very challenging task, and where a tradeoff between precision and cost exist. Indeed, the use of external tracking device allows to recover patient specific respiratory information which can be effectively used to perform motion correction. On the other hand, such instrumentation has a cost associated, which is not reachable by all institutions.

The single-subject based model, constructed as a first approach of respiratory modelling, considers the transformation between two respiratory states obtained from a single subject. This approach, far from being realistic, represents the simplest and easier model to obtain among the studied models. Its simplicity, coming from the fact of using a single subject, can introduce respiratory pattern biases in motion

compensated images. Fortunately, the chosen model used in our experiments describes fairly well the average respiratory motion obtained from the first statistical model, STAT-1. However, this does not imply that in terms of methodology as such, the single-subject based model is robust, allowing good results independent of the motion transformation selected as layout. In this sense, if this method is going to be used, care must be taken when choosing the known respiratory motion from where the model is generated, which would be checked (in the absence of any patient-specific respiratory information) against a more representative model, as described by the population-based models, STAT-1 and STAT-2.

An interesting issue related to both, the single-subject model, and STAT-1, is the linear interpolation used to derive more motion states between end-expiration and end-inspiration. In this sense, the STAT-2 model allowed to compare the impact of performing such approximation on motion-compensated reconstruction images. Discussion on this point is given further.

9.1.5 Evaluating the method

Results obtained on simulated and phantom data are satisfactory and very promising. Throughout the experiments, the proposed method showed its ability to compensate the effects produced by motion during an emission tomography study. For patient data, unfortunately the lack of a ground truth made its validation impossible. However, from the obtained results we could visualize the improvements of contrast recovery in the lesion area, and a decrease of lesion's volume depending of the lesion's position. Encouraged by these preliminary results, we think that an improvement of images degraded by motion can be obtained by application of this approximative motion compensation technique. At present, further research is needed in this direction.

The so-called simplified model was compared in terms of motion correction against the statistical model. The obtained results were sat-

isfactory since both models contribute with the same tendency (volume change, displacement directions, etc.) on the correction of tumoral lesions on the five patients. However, due to the position of the lesions within the lungs, it could be of great interest to repeat the comparison on lesions situated on what it could be called "more challenging" positions, that is to say, in positions where the lesions would suffer bigger deformations than in those the experiments were carried out. In this sense, validation of the methodology on a larger patient dataset using a ground truth like respiratory gating would be indispensable to measure the true potential of using simplified models, and to determine as well, the true improvements of using more complex respiratory models.

The spatial dependence of the effects of respiratory motion on lungs lesions is another point to be remarked. For instance, it was shown that lesions situated at the base of the lungs are more prone to be subject of greater deformations than those located near the back, attached to rigid structures, etc. This fact can be considered not only from a clinical point of view, where knowledge on this matter can contribute greatly, for example, to the planning target volume, where motion is considered in the determination of the planning tumor volume (PTV)(see appendix A.1), but also from a technical point of view, where knowledge on how this spatial-dependence occurs, can aid at correcting images with a better precision. The statistical respiratory motion models present themselves as a first step in this direction, providing and characterizing information from a set of individuals, and thus yielding a sort of generalized deformation map. This map, up to this moment has been created by considering only the anatomy of lungs. One new hypothesis that can arise from this fact is the eventual need of considering neighbor organs to describe the deformation of lung lesions situated at the interface of these organs, which was not studied in this thesis and is topic of further research [70, 60, 8].

9.1.6 Others considerations

Some remarks at an implementational level can be made. As it was discussed, one of the barrier to breach in order to approach the 3-D MLEM-based algorithms to the clinical scenario is to improve its convergence speed. Although not the main topic of this thesis work, the speed constraints were revisited and some acceleration schemes were proposed. However, the need of parallelizing the task is always present when respiratory motion correction (which occurs in 3-D) is considered.

9.2 Perspectives

Some perspectives have been already mentioned previously. This section summarizes them and presents some others.

- Without a doubt, the more important perspective at present is the evaluation of using approximative respiratory models on a larger patient dataset in conjunction with ground truth references, allowing a correct evaluation and validation of the methodology.
- The use of 4-D CT scan systems coupled to ET cameras would allow the construction of the respiratory motion model directly from the patient. This would be a further and important step to improve the model used for respiratory motion correction.
- Improvements of the respiratory motion models include the use of the main modes of deformation found through the PCA study. In this sense, the variability of deformations described by the first four modes of deformations could be used with the proposed average model in order to give the statistical models a higher specificity towards a more patient-specific model.
- Considering deformations produced by lungs neighbor organs for lesions situated on the lungs frontier. This can be globally seen

as constructing a thorax/abdomen deformation model to treat tumoral lesions situated at the interface of organs.

- As it was described, the proposed voxel model consists in spheres deforming into ellipsoids under the action of a known deformation. In this sense, a further possible improvement is the incorporation of elasticity properties, so tissues would deform accordingly to its elasticity properties as well. This however, should be considered in conjunction with current spatial image resolutions to clarify the real improvement this can bring.

- The motion correction methodology proposed here considers a discrete number of motion states (discretized motion) which is set equally throughout the lungs. One possible improvement would consist in making this selection spatial dependent. This, since deformation due to respiratory motion occurs at different scales depending on the position (e.g., larger displacements at the bottom and smaller at the apex of the lungs). This way, fewer number of motion states are required to characterize more or less static regions, while more number of motion states are set to describe larger deformations.

- Incorporating other correction factors, apart from attenuation correction as presented here, along with the proposed respiratory motion correction.

Appendix A

Appendixes

A.1 Planning target volume and others

Accurate radiation therapy involves delineation of the zone of be body to be irradiated. This is accomplished by specifying several contours (it is performed on a 2-D space). Fig. A.1 depicts the contours and their relationship.

Basically, a first contour is determined, called the Gross Tumor Volume (GTV) that corresponds to the true tumor area. From this,

a margin considering microscopic spread is added to form the Clinical Tumor Volume (CTV). A second margin is added that takes into account for setup variations and patient and organ motion. This results in the Planning Tumor Volume (PTV). More details can be found on the ICRU report #62:Prescribing, Recording and Reporting Photon Beam Therapy (1999).

A.2 The Central Slice Theorem: an example

As a matter of example, we will demonstrate that the 1-D Fourier of a projection at a given angle, equals the 2-D Fourier transformation of the slice of the object at the same angle.

Let's start by defining the 2-D Fourier transform of the object as

$$F(u,v) = \int_{-\infty}^{\infty}\int_{-\infty}^{\infty} f(x,y)e^{-j2\pi(ux+vy)}dxdy. \tag{A.1}$$

Similarly, let's define the projection at angle θ as $P_\theta(t)$, and its Fourier transformation

$$S_\theta(w) = \int_{-\infty}^{\infty} P_\theta(t)e^{-j2\pi wt}dt. \tag{A.2}$$

Let's simplify the example by choosing $\theta = 0$. The Fourier transform of the object along the line in the frequency domain given by v=0 is now

$$F(u,0) = \int_{-\infty}^{\infty}\int_{-\infty}^{\infty} f(x,y)e^{-j2\pi ux}dxdy \tag{A.3}$$

$$= \int_{-\infty}^{\infty}\left[\int_{-\infty}^{\infty} f(x,y)dy\right]e^{-j2\pi wt}dx. \tag{A.4}$$

The expression between brackets is by definition the projection along lines of constant values of x,

$$P_{\theta=0}(x) = \int_{-\infty}^{\infty} f(x,y)dy. \tag{A.5}$$

So, Eq. (A.4) can be written as

$$F(u,0) = \int_{-\infty}^{\infty} P_{\theta=0}(x) e^{-j2\pi ux} dx. \tag{A.6}$$

The right hand of Eq. (A.6) represents the 1-D Fourier transformation of $P_{\theta=0}$. Thus, we have the following equivalence:

$$F(u,0) = S_{\theta=0}(u). \tag{A.7}$$

Which establishes the equality between the vertical projection $S_{\theta=0}(u)$ and the 2-D Fourier transformation of the object. This result is independent of the angle.This body part will be downloaded on demand.This body part will be downloaded on demand.This body part will be downloaded on demand.This body part will be downloaded on demand.This body part will be downloaded on demand.This body part will be downloaded on demand.This body part will be downloaded on demand.

A.3 Regularizing via MAP estimator

It is worth to mention that (4.8) can be obtained from a bayesian framework. Indeed, *a maximum a posteriori* (MAP) estimator can be constructed. By Bayes rules:

$$P(\boldsymbol{\lambda}|\boldsymbol{p}) = \frac{P(\boldsymbol{p}|\boldsymbol{\lambda})P(\boldsymbol{\lambda})}{P(\boldsymbol{p})} \approx P(\boldsymbol{p}|\boldsymbol{\lambda})P(\boldsymbol{\lambda}) \tag{A.8}$$

With $P(\boldsymbol{p})$ the probability density function (PDF) of the realization vector $\boldsymbol{p}$ supposed to be constant, and $P(\boldsymbol{\lambda})$ the a priori PDF of $\boldsymbol{\lambda}$.

Using (4.6) and (A.8), the estimated image is obtained by:

$$\hat{\boldsymbol{\lambda}}_{\boldsymbol{MAP}} = \arg\max_{\lambda}[l(\boldsymbol{\lambda})P(\boldsymbol{\lambda})]. \tag{A.9}$$

Equivalently to the unpenalized ML case, it results convenient to apply logarithm to separate terms:

$$\hat{\boldsymbol{\lambda}}_{\boldsymbol{MAP}} = \arg\max_{\lambda}[L(\boldsymbol{\lambda}) + \log(P(\boldsymbol{\lambda}))]. \tag{A.10}$$

In Bayesian estimation it is usual to use a Gibb distribution to form the prior PDF. That is to say, the prior $P_p(\boldsymbol{\lambda})$ is assumed to be proportional to $e^{-\beta R(\boldsymbol{\lambda})}$, with β the Bayes weight of the prior and $R(\boldsymbol{\lambda})$ the non-negative energy function to be constructed. Then, the log-posterior would be

$$\log(P(\boldsymbol{\lambda}|\boldsymbol{p})) \equiv \log(P(\boldsymbol{p}|\boldsymbol{\lambda})P(\boldsymbol{\lambda})) = L(\boldsymbol{\lambda}) - \beta R(\boldsymbol{\lambda}), \tag{A.11}$$

and the image estimate would be equivalent to (4.8).

The probability density function (PDF) $P(\boldsymbol{\lambda})$ (or the function $R(\lambda)$ in (4.8)) describes *a priori* information of the expected image to be reconstructed. The way $P(\boldsymbol{\lambda})$ is constructed is important since it will reflect the favored type of reconstructed images. A too strict prior will effectively decrease the noise but with the detriment of loosing information. In the other hand, a too mild prior will not regularize the image sufficiently. Thus, a tradeoff between noise and spatial resolution has to be considered in the design of the prior.

There exist several common forms of $R(\boldsymbol{\lambda})$. Typically in ET, one searches to penalize roughness in the reconstructed images. One choice is to consider $R(\boldsymbol{\lambda})$ as a weighted sum of potential energies computed over a neighborhood of each pixel/voxel. Formally,

$$R(\boldsymbol{\lambda}, b) = \sum_{i \in N_b} w_{bi}\psi(\lambda_b - \lambda_i). \tag{A.12}$$

Where $R(\boldsymbol{\lambda}, b)$ stands for the energy value of $R(\cdot)$ on $\boldsymbol{\lambda}$ at pixel/voxel b, w_{bi} is a non-negative and symmetric weight of pixel/voxel i in the neighborhood N_b of b, and $\psi(\cdot)$ is the potential function applied to the difference between image/voxels values in the neighborhood N_b. In general, the design of the potential function ψ must verify the following conditions:

- ψ is nonnegative.
- ψ is symmetric.
- ψ is continuously differentiable.
- $\dot{\psi(x)} = \frac{d\psi}{dx}(x)$ is nondecreasing for $x \geq 0$.
- $\frac{\dot{\psi(x)}}{x}$ is nonincreasing for $x \geq 0$.
- $\lim_{t \to 0} \frac{\dot{\psi(x)}}{x}$ is finite and nonzero.

The selection of the potential function $\psi(\cdot)$ is quite important since it defines the desired prior behavior. Nevertheless, this selection is precisely the weak point of these type of approaches. Indeed, observing Fig. A.1, it can be seen how a different choice of the potential function will penalize much or less (with the quadratic function being the more penalizing one) differences in pixel/voxel values (i.e., roughness criteria) but with the consequence of penalizing edges in the image as well (see [20] for an edge-preserving regularization method). This secondary and unwanted effect goes against the principal goal of ET: to highlight abnormal (and sometimes small) changes in tracer activity. One more time, much in a similar way than the filter selection in the FBP method, a tradeoff between noise reduction and image resolution has to be considered when selecting the potential function. This point will be more clear in the derivation of the penalized version of the classical Expectation Maximization (EM) algorithm, where the derivatives of the potential functions (Fig. A.1(b)) play the role of penalty terms[1].

Almost all prior functions can be written in the form of Eq. (A.12) with the exception of the Median-Root-Prior (MRP) [3]. The prior's basic assumption is of guiding the reconstruction towards locally monotonic images.

[1]Known also as the One-Step-Late (OSL) technique.

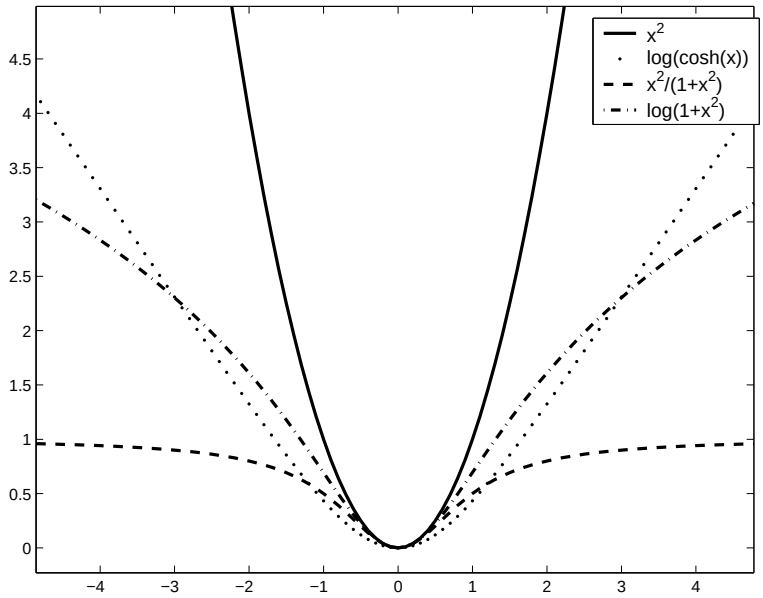

(a) Potential Functions

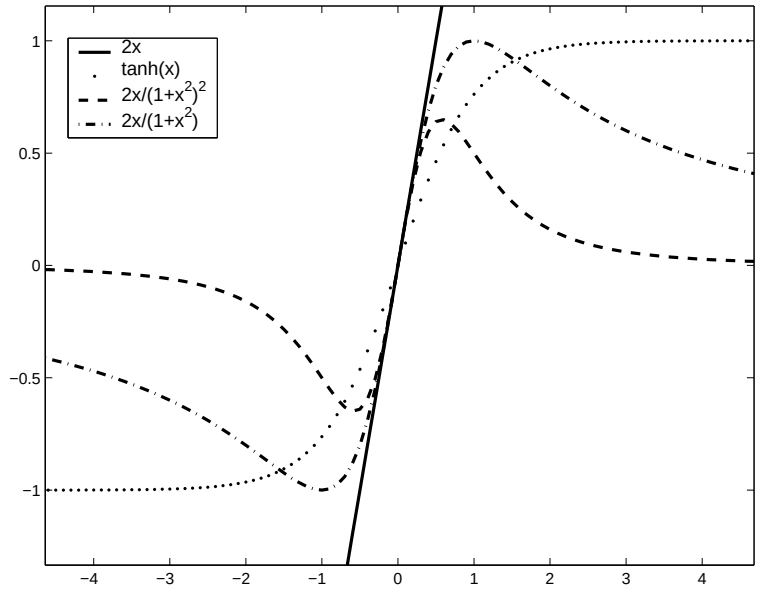

(b) Derivatives of Potential Functions

Figure A.1: Potential functions of Table A.1 as a function of the pixel-voxel difference x (a) and its corresponding derivatives (b).

$\psi(\mathbf{r})$	$\frac{\partial}{\partial \lambda_{\mathbf{b}}}\psi(\mathbf{r})$
r^2	$2r$
$\log(cosh(r))$	$\tanh(r)$
$r^2/(1+r^2)$	$2r/(1+r^2)^2$
$\log(1+r^2)$	$2r/(1+r^2)$

Table A.1: Some Potential Functions used with the Gibbs Prior in (A.12). Their respective plots are presented in Fig. A.1

Definition 1: A 1-D signal is locally monotonic of degree d (or LOMO-d) if every interval of length d is monotonic (non-decreasing or non-increasing)[1].

Definition 2: An image is locally monotonic if it is 1-D locally monotonic in all the allowed orientations [1].

For 2-D images, the orientation set is typically defined as the set of vertical, horizontal and diagonal directions. But this definition can be further extended to the 3-D case.

The derivation of the MRP resulted mostly from an intuitive design of the prior rather than from an analytical analysis. The penalty term ($R(\lambda)$ in Eq. (A.12)) has now the form below

$$R(\boldsymbol{\lambda}, b) = \sum_{b} \frac{(\lambda_b - M_b)^2}{2M_b}, \tag{A.13}$$

with $M_b = Median\{\lambda_i | i \in N_b\}$.

The local-monotonicity condition and the properties of the robust median operator allow to preserve edges information on the reconstructed images. Furthermore, there is no need to adequate or to indicate the prior to act differently in edgy or flat regions of the image, neither to adjust any other parameter responsible of the edge sensitivity (as occurs in the design of the potential function in (A.12)).

The MRP has found great acceptance in the scientific community, which is due mainly to the good results obtained from its utilization, and the simplicity of its practical implementation.

Bayesian image reconstruction helps to reduce the problem of noise on reconstructed images. However, proper hyper parameter settings are need in order to take full advantage of the benefits of such approach. Further discussion of Bayesian methods can be found in [93, 69, 109].

In the next section, we focus on the resolution of the objective function (Eq. (4.7) or (4.8) for the penalized case). For this, the optimization transfer principle will presented, since from this concept almost all algorithms can be derived.

A.4 Optimization Transfer Principle

The optimization transfer principle was generalized and incorporated into the resolution of inverse problems, and posteriorly into tomographic image reconstruction by the works of De Pierro [91] and Lange [69]. It provides us with a tool to simplify or to improve (commonly in terms of convergence) the task of maximization.

Basically, instead of maximizing the original objective function, one chooses an alternative objective function or *surrogate function*, which is more easy to maximize and/or converges faster than the original objective function, accelerating the whole optimization process.

Formerly, let's be Φ the original objective function to be maximized, ϕ the chosen surrogate function, and $\boldsymbol{\theta}$ the set of unknown parameters to be found maximizing ϕ and Φ. Then, at each iteration one wants to find a new surrogate function ϕ, which is maximized towards the maximizer of Φ in the following way.

$$\boldsymbol{\theta}^{<K+1>} = \arg\max_{\boldsymbol{\theta}} \phi(\boldsymbol{\theta}; \boldsymbol{\theta}^{<K>}). \tag{A.14}$$

Where $< K >$ stands for the kth iteration. To find an appropriate surrogate function, the following general condition has to be satisfied:

$$\Phi(\boldsymbol{\theta}) - \Phi(\boldsymbol{\theta}^{<K>}) \geq \phi(\boldsymbol{\theta}; \boldsymbol{\theta}^{<K>}) - \phi(\boldsymbol{\theta}^{<K>}; \boldsymbol{\theta}^{<K>}). \forall \boldsymbol{\theta}, \boldsymbol{\theta}^{<K>}, \tag{A.15}$$

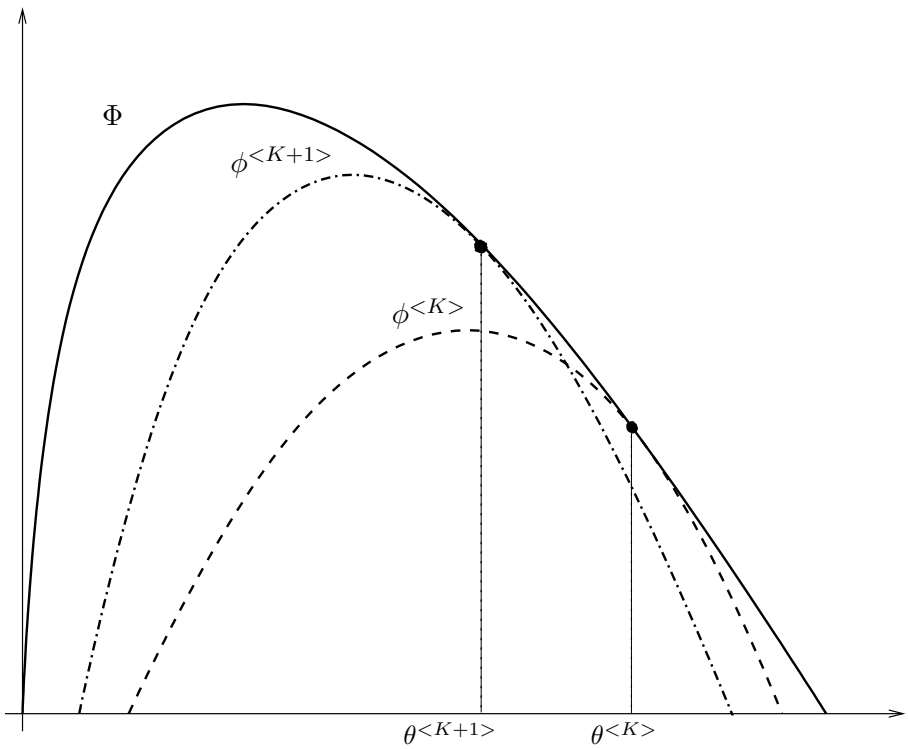

Figure A.2: The optimization transfer principle. A 1-D illustration of its basic idea. A surrogate function ϕ, which is easier to maximize than Φ, is iteratively selected and maximized in order to reach the maximum of Φ.

¿From which, equivalent satisfying conditions can be derived:

$$\phi(\boldsymbol{\theta}^{<K>};\boldsymbol{\theta}^{<K>}) = \Phi(\boldsymbol{\theta}^{<K>}) \tag{A.16}$$

$$\nabla_{\boldsymbol{\theta}}\phi(\boldsymbol{\theta};\boldsymbol{\theta}^{<K>})|_{\boldsymbol{\theta}=\boldsymbol{\theta}^{<K>}} = \nabla\Phi(\boldsymbol{\theta})|_{\boldsymbol{\theta}=\boldsymbol{\theta}^{<K>}} \tag{A.17}$$

$$\phi(\boldsymbol{\theta};\boldsymbol{\theta}^{<K>}) \leq \Phi(\boldsymbol{\theta}), \forall\boldsymbol{\theta} \geq 0. \tag{A.18}$$

Fig. A.2 depicts in 1-D the basic idea of the optimization transfer principle.

The optimization transfer principle provides us with a methodology to find the maximum of Φ, when its maximization is difficult or

not tractable. This is the case of the Maximum Likelihood Expectation Maximization (MLEM) algorithm presented in the next section, in which we will see that maximization of the original objective function is not possible, so a surrogate function based on the expectation of the hidden data is chosen.

A.5 The SAGE algorithm

Similarly to the classical EM algorithm, an EM-based surrogate function is used in the formulation of the SAGE algorithm. But this time the surrogate function is designed to operate over a less informative complete-data space than the one used in the classical EM algorithm.

A first version of the SAGE algorithm, called SAGE-1, divides the parameter vector into subsets, with the number of subsets equal to the number of pixels/voxels in the image. With this criteria, for the subset S the surrogate function is

$$\phi^S(\lambda_b, \boldsymbol{\lambda}^{<K>}) = Q(\lambda_b, \boldsymbol{\lambda}^{<K>}) - \beta R(\lambda_b, \boldsymbol{\lambda}^{<K>}) \tag{A.19}$$

with

$$Q(\lambda_b, \boldsymbol{\lambda}^{<K>}) = \sum_d -\lambda_b R_{db} + \sum_d \tilde{p_{db}} \log(\lambda_b), \tag{A.20}$$

and $\tilde{p_{db}} = E[p_{db}|p_d, \lambda]$.

Eq. (A.19) and (A.20) present the basis of SAGE-1. The iterative form can be found similarly as the classical MLEM algorithm. It is illustrative to visualize the pseudo-code of both, the SAGE-1 and the MLEM algorithm

Algorithm A.5.1: EM($MLEM$)

$$\textbf{for } K \leftarrow 0 \textbf{ to } \text{n-iterations}$$
$$\textbf{do} \begin{cases} \overline{p_d} = \sum_b R_{db}\lambda_d^{<K>}, d = 1, \ldots, M. \\ \textbf{for } b \leftarrow 1 \textbf{ to } N \\ \quad \textbf{do} \begin{cases} C_b^{<K>} = \sum_d \frac{p_d R_{db}}{\sum_{b'} \lambda_{b'}^{<K>} R_{db'}} \\ \lambda_b^{<K+1>} = \lambda_b^{<K>} C_b^{<K>} / \sum_d R_{db} \end{cases} \end{cases}$$

Algorithm A.5.2: SAGE($version1$)

$$Initialize : \overline{p_d} = \sum_b R_{db}\lambda_d^{<K=0>}, d = 1, \ldots, M.$$
$$\textbf{for } K \leftarrow 0 \textbf{ to } \text{n-iterations}$$
$$\textbf{do for } b \leftarrow 1 \textbf{ to } N$$
$$\textbf{do} \begin{cases} C_b^{<K>} = \sum_d \frac{p_d R_{db}}{\sum_{b'} \lambda_{b'}^{<K>} R_{db'}} \\ \lambda_b^{<K+1>} = \lambda_b^{<K>} C_b^{<K>} / \sum_d R_{db} \\ \lambda_j^{<K+1>} = \lambda_j^{<K>}, j \neq k \\ \overline{p_d} \leftarrow \overline{p_d} + (\lambda_b^{<K+1>} - \lambda_b^{<K>}) R_{db}, \forall n : R_{db} \neq 0 \end{cases} \qquad \text{(i)}$$

As it can be noticed, SAGE-1 starts with an initial estimate of the detected measurements. Then, each parameter is estimated (i.e., λ_b) and an update of the detected measurements is immediately performed within the inner loop. In the other hand, the classical MLEM algorithm has to wait until all parameters have been updated in order to re-estimate the detected measurements. In other words, MLEM perform a simultaneous update, whereas SAGE-1 performs a sequential one.

The SAGE-1 algorithm have shown to converge somewhat faster than the classical MLEM. Nevertheless, according to the authors, this speed-up in convergence is only important under well-conditioned problems. A less-informative data space (and consequently producing a faster convergence) has been designed, which takes into account un-

certainties in the background events. For this Eq.(4.4) is modified to account for random events for each detector tube (i.e. r_d), and is as follows:

$$\overline{p_d} = \sum_{b=1}^{n} \lambda_b R_{db} + r_d. \tag{A.21}$$

The derivation of the SAGE-2 algorithm is obtained in the same way as for SAGE-1 and its structure remains the same as well, with the difference that Eq. (i) in the SAGE-1 algorithm is now replaced by:

$$\lambda_b^{<K+1>} = \max\left\{(\lambda_b^{<K>} + z_b)C_b^{<K>} / \sum_d R_{db} - z_b, 0\right\}. \tag{A.22}$$

Where $z_b = \min_{d:R_{db}\neq 0}\{r_d/R_{db}\}$ allows to reduce the Fisher information in the new data space and thus, to increase the speed of convergence. Indeed, for the classical complete-data space the Fisher information is diagonal with entries $\sum_d R_{db}/\lambda_b$, whereas for the new data space the Fisher information is $\sum_d R_{db}/(\lambda_b + z_b)$ [27].

A.6 The penalized MLEM algorithm

For the penalized case, we are interested to maximize the objective function $\Phi = L(\boldsymbol{\lambda}) - \beta R(\boldsymbol{\lambda})$. With $L(\boldsymbol{\lambda})$ the log-likelihood, $R(\boldsymbol{\lambda})$ the potential function serving as penalty term, and β an hyperparameter to be adjusted.

Similarly to the un-penalized case, the E-step is performed as before, but now the M-step maximizes the log-posterior probability

$$L_p(\boldsymbol{\lambda}, \boldsymbol{\lambda}^{<K>}) = Q(\boldsymbol{\lambda}, \boldsymbol{\lambda}^{<K>}) + \log(P(\boldsymbol{\lambda})) = Q(\lambda, \lambda^{<K>}) - \beta R(\boldsymbol{\lambda}). \tag{A.23}$$

Then, maximization is achieved by solving

$$\frac{\partial}{\partial \lambda_b} L_p(\boldsymbol{\lambda}, \boldsymbol{\lambda}^{<K>}) = 0. \tag{A.24}$$

Using (A.23) and (4.15)

$$\frac{\partial}{\partial \lambda_b} L_p(\boldsymbol{\lambda}, \boldsymbol{\lambda}^{<K>}) = \frac{\partial}{\partial \lambda_b} Q(\boldsymbol{\lambda}, \boldsymbol{\lambda}^{<K>}) - \beta \frac{\partial}{\partial \lambda_b} R(\boldsymbol{\lambda}) = 0 \tag{A.25}$$

$$= -\sum_d R_{db} + \sum_d \frac{E[p_{db}|p_d, \boldsymbol{\lambda}]}{\lambda_b} - \beta \frac{\partial}{\partial \lambda_b} \sum_{b'} R(\boldsymbol{\lambda}, b') = 0 \tag{A.26}$$

$$= -\sum_d R_{db} + \sum_d \frac{E[p_{db}|p_d, \boldsymbol{\lambda}]}{\lambda_b} - \beta \frac{\partial}{\partial \lambda_b} R(\boldsymbol{\lambda}, b) = 0 \tag{A.27}$$

The One-Step-Late (OSL) technique uses the current image estimate to calculate the derivative of $R(\lambda)$ [40]. This way, by incorporating this technique and replacing (4.15) into (A.27), the iterative penalized-EM algorithm can be derived

$$\lambda_b^{<K+1>} = \frac{\lambda_b^{<K>} C_b^{<K>}}{\sum_d R_{db} + \beta \frac{\partial}{\partial \lambda_b} R(\lambda, b)|_{\lambda = \lambda^{<K>}}}. \tag{A.28}$$

With,

$$C_b^{<K>} = \sum_d \frac{p_d R_{db}}{\sum_{b'} \lambda_{b'}^{<K>} R_{db'}}. \tag{A.29}$$

As it can be noticed from Eq. (A.28), the derivative of the potential function $R(\lambda, b)$ introduces the penalty component into the iterative algorithm. Little deviations from the assumptions made for the true images, cause low values of the derivative term and thus, low penalty terms. On the other hand large values of the derivative indicate that the image deviates from the prior assumption, and so, it is penalized. In addition, it is useful to visualize the effect of selecting different potential function in function of its derivative, as shown in

Fig. A.1(b), where it can be seen how more complex designs of the potential function search to limit possible over penalization of large pixel/voxel differences, presuming this occurs in edgy regions.

The OSL technique makes possible the MAP estimation by using an approximative maximization step based on the previous values for neighboring pixels/voxels. Other approaches based also in general Markov Random Field (MRF) prior distributions can be found in references [91, 46].

A.7 Gradient-Based Methods

In previous sections, it has been shown how the image reconstruction problem can be addressed statistically by means of ML and MAP estimators, which have shown to yield better results than using deterministic methods as the FBP algorithm. Since the work of Shepp and Vardi [104], the method of choice to find ML or MAP estimators has been the EM algorithm, which uses the concept of "complete data"[2] to make tractable the optimization problem. However, the major problem with this approach is its slow convergence rate. As it was described previously, several approaches have been proposed to overcome this, all of them under the framework of ML(MAP)-EM based estimation. In the other hand, gradient-based algorithms were introduced in ET image reconstruction by retaking and adapting classical optimization tools.

Basically, all gradient-based algorithms can be written in the following form:

$$\boldsymbol{\theta}^{<K+1>} = \boldsymbol{\theta}^{<K>} + \alpha^{<K>}\boldsymbol{d}^{<K>}. \tag{A.30}$$

Where the parameter vector θ is updated iteratively searching in a given direction d at a given step α.

[2]It can also be seen as derived from the optimization transfer principle.

The first and simplest approach one can think of, is the steepest ascent algorithm. The direction of search $\boldsymbol{d}$ is simply the gradient of the objective function, $\boldsymbol{d}^{<K>} = \nabla\Phi(\boldsymbol{\theta})|_{\theta=\theta^{<K>}}$. The scalar parameter $\alpha^{<K>}$ is usually chosen using a line search technique to maximize $\Phi(\boldsymbol{\theta}^{<K+1>})$.

Although simple, the steepest ascent algorithm has a low convergence rate that, as all gradient-based algorithms, has a convergence that depends on the condition number of the Hessian $\boldsymbol{H}(\boldsymbol{\theta})$ of $\Phi(\boldsymbol{\theta})$. It has been shown that better convergence rates can be attained by using pre-conditioners[71]. This, since the convergence properties will be now dependent of the product between the Hessian and the pre-conditioner matrix. In fact, the ideal pre-conditioner is the inverse of the Hessian matrix (which results in the Newton's method), but as its computation and storage is impractical, it is common to use approximations of the Hessian matrix. This generate a family of Quasi-Newton methods, which have the following general form

$$\boldsymbol{\theta}^{<K+1>} = \boldsymbol{\theta}^{<K>} + \beta^{<K>}\boldsymbol{H}^{<K>}\nabla\Phi(\boldsymbol{\theta})|_{\theta=\theta^{<K>}}. \tag{A.31}$$

Where $\beta^{<K>}$ is chosen to maximize $\Phi(\boldsymbol{\theta}^{<K+1>})$ in the direction $\boldsymbol{d}^{<K>} = \boldsymbol{H}^{<K>}\nabla\Phi(\boldsymbol{\theta})|_{\theta=\theta^{<K>}}$.

When $\boldsymbol{H}^{<K>}$ is equal to the inverse of the Hessian matrix, we have the Newton's method, which presents quadratical convergence rate.

The steepest ascent, the Newton's and the Quasi-Newton's methods compute the direction vector $\boldsymbol{d}$ based merely on the gradient of the objective function. Convergence can be further ameliorated by also considering previous computations of the direction vector $\boldsymbol{d}$. This results in the Conjugated Gradient (CG) algorithm. Several forms of CG algorithms have been proposed. As example, the preconditioned Polak-Ribiere form of CG is presented

$$\boldsymbol{\theta}^{<K+1>} = \boldsymbol{\theta}^{<K>} + \alpha^{<K>}\boldsymbol{d}^{<K>} \tag{A.32}$$

$$\boldsymbol{d}^{<K>} = \boldsymbol{a}^{<K>} + \gamma^{<K-1>}\boldsymbol{d}^{<K-1>} \tag{A.33}$$

$$\boldsymbol{a}^{<K>} = \boldsymbol{C}\nabla\Phi(\boldsymbol{\theta})|_{\theta=\theta^{<K>}} \tag{A.34}$$

$$\gamma^{<K-1>} = \frac{(\nabla\Phi(\boldsymbol{\theta})|_{\theta=\theta^{<K>}} - \nabla\Phi(\boldsymbol{\theta})|_{\theta=\theta^{<K-1>}})'\boldsymbol{d}^{<K>}}{\nabla\Phi(\boldsymbol{\theta})|'_{\theta=\theta^{<K-1>}}\boldsymbol{d}^{<K-1>}} \tag{A.35}$$

Where $\boldsymbol{C}$ is the positive definite pre-conditioner matrix.

Different forms of the term γ produce different forms of CG algorithms (e.g. Fletcher-Reeves method, Partan's method, Zoutendijk's method).

Under unconstrained quadratic optimization problems, the CG methods present good convergence rate. However, for non-quadratic objective functions (which can result from the incorporation of non-quadratic priors densities) or when positivity constraints are required, the CG methods have lower convergence rates and even more, convergence is not always guaranteed [99]. The positivity constraint can be assured by restricting the step size α so that the image is positive at each iteration.

This method however, has slow convergence in images with many zero valued elements [57]. In [57], a bent-line-based approach solve the positivity problem by backprojecting images with negative values into a constraint surface by bending the search direction. Nevertheless, the major drawback of this approach is of requiring extra backprojection operations each time negative values are found in the current guess image.

In [81], Mumcuoglu et al. propose to convert the constrained problem into an unconstrained one by using a penalty function f. In addition, a weighting parameter η, such as $\eta^{<K>} > 0$ and $\eta^{<K>} > \eta^{<K+1>}$, is associated to this penalty function. Then, at each iteration K, one finds for $\boldsymbol{\theta}^{<K>}$ and for the resulting sequence any limit point is a solution of the original constrained problem. In other words, instead of maximizing the problem

$$\arg\max_{\theta \geq 0} \phi(\boldsymbol{\theta}), \tag{A.36}$$

we solve the unconstrained problem

$$\arg\max q(\eta, \boldsymbol{\theta}) = \phi(\boldsymbol{\theta}) - \frac{1}{\eta^2} f(\boldsymbol{\theta}) \tag{A.37}$$

With $f(\boldsymbol{\theta})$ satisfying 1) $f(\theta) \geq 0$ for all $\boldsymbol{\theta}$, and 2) $f(\boldsymbol{\theta}) = 0$ if $\boldsymbol{\theta} \geq 0$.

In practice, Mumcuoglu et al. [81] found that rather than computing a sequence of parameters θ for decreasing values of η, a single value of $\eta = 0.01\theta_{max}$ yields good results without significant reduction of convergence rate nor a lost of efficacy of the penalty term. Furthermore, the authors propose a modified preconditioner matrix to account for the positivity constraint. This, based in the previous work of Lange et al. [68] and others, who noted the similarity of the EM algorithm with gradient-based techniques. Indeed, it was shown that the EM algorithm can be rewritten into a form of gradient-ascent where the direction vector is computed as the product of the gradient vector and a diagonal matrix formed by scaled versions of the current image estimates [68].

Improvements in preconditioners, better handling of positivity constraints and development of rapid gradient-based block-iterative methods are centers of interest in current development of gradient-based image reconstruction.

A.8 Computing line-ellipsoid intersection

Given the equation of an ellipsoid in its standard form:

$$x^2/a^2 + y^2/b^2 + z^2/c^2 = r^2$$

For an ellipsoid $r = 1$ and for a sphere $a = b = c = 1$, and the parametric equation of a line in 3-D $(x_{r0}, y_{r0}, z_{r0}) + t(d_x, d_y, d_z)$, where

(x_{r0}, y_{r0}, z_{r0}) is a known point in the line and $d_x = x_{r0} - x_{r1}, d_y = y_{r0} - y_{r1}, d_z = z_{r0} - z_{r1}$, with (x_{r1}, y_{r1}, z_{r1}) other point in the line.

The values of t defining the intersections points are found by: $t_{i=\{1,2\}} = -B/2A \pm \sqrt{B^2/4A^2 - C/A}$, with

$$A = (d_x bc)^2 + (d_y ac)^2 + (d_z ab)^2 \tag{A.38}$$

$$B = 2(d_x x_{r0} b^2 c^2 + d_y y_{r0} a^2 c^2 + d_z z_{r0a^2b^2}) \tag{A.39}$$

$$C = ((bcx_{r0}^2 + (acy_{r0})^2 + (abz_{r0})^2 - (rabc)^2). \tag{A.40}$$

Thus the intersection length l between the line and the ellipsoid is computed as

$$l = |t_1 - t_2| \sqrt{d_x^2 + d_y^2 + d_z^2} \tag{A.41}$$

A.8.1 Transforming subjects to a common anatomy

We describe here the iterative method presented in [43, 42] to build an average image from a set images. Given a set of N images I_i, we pick one of them as a first estimate of the average: this reference image is denoted by I_R. The whole iterative procedure consists in five steps that are iterated until convergence.

1. Compute the elastic registrations between each image I_i, with $i : 1 \ldots N$ and the reference image I_R are performed. This yield N transformations D_i. The *affine* component of these transformations is computed by approximating each D_i by a affine transformation A_i in the least squares sense.

2. Compute the (*residual*) transformations R_i between each image $I_i \circ A_i$ (I_i resampled by A_i) and I_R. The R_i are called residuals transformations since they are assumed to represent only morphological differences between images.

3. An average intensity image $\overline{I}$ is obtained by averaging the I_i after transformation by the composition of A_i and R_i, i.e.

$$\overline{I} = \frac{1}{N} \sum_i I_i \circ A_i \circ R_i$$

this average intensity image $\overline{I}$ has the same shape than I_R.

4. The mean transformation $\overline{R} = 1/N \sum_i R_i$ is computed. This transformation represent the shape variation between the reference image and the set of images $A_i \circ I_i$).

5. 5.- The transformation $\overline{R}$ is applied to $\overline{I}$ to obtain an average intensity and shape image, i.e. $\overline{I} \circ \overline{R}^{-1}$. This resulting image is used as reference image in the next iteration.

To validate the results, the same criteria used in [43, 42] were taken as quality measures of the average model. Namely, the Root Mean Square Norm (RMSN) that measures the shape variation expressed by a displacement vector field D,

$$RMSN(D) = \sqrt{\frac{1}{n} \sum_x \|x - D(x)\|^2}, \tag{A.42}$$

and the Normalized Intensity Difference, which gives a measure of brightness disparity between two images,

$$NID(I_i, I_j) = \sqrt{\frac{\sum_x (I_i(x) - I_j(x)^2)}{\sum_x (I_i(x))^2}}. \tag{A.43}$$

If the procedure converges towards an average model one should find decreasing values for RMSN and NID between successive iterations.

A.9 Configuration file example for the Simset photon history generator module

Example of a typical configuration file for the Simset Photon History Generator (PHG) module

```
# RUNTIME OPTIONS
BOOL simulate_stratification = false
BOOL simulate_forced_detection = false
BOOL forced_non_absorbtion = true
REAL acceptance_angle = 5.0
INT num_to_simulate = 50000000
BOOL simulate_SPECT = true
BOOL adjust_for_positron_range = false
BOOL adjust_for_collinearity = false
REAL minimum_energy = 110.0
REAL photon_energy = 140.5
REAL weight_window_ratio = 5.0
BOOL point_source_voxels = false
INT random_seed = 0
INT length_of_scan = 1800
# OBJECT GEOMETRY VALUES
NUM_ELEMENTS_IN_LIST object = 129
INT num_slices = 128
NUM_ELEMENTS_IN_LIST slice = 9

INT slice_number = 0
REAL zMin = -19.2
REAL zMax = -18.9
REAL xMin = -19.20
REAL xMax = 19.20
REAL yMin = -19.20
REAL yMax = 19.20
INT num_X_bins = 128
INT num_Y_bins = 128
NUM_ELEMENTS_IN_LIST slice = 9
.....
```

Blocks repeated up to slice 127
TARGET CYLINDER INFORMATION
NUM_ELEMENTS_IN_LIST target_cylinder = 3
REAL target_zMin = -19.2
REAL target_zMax = 19.2
REAL radius = 19.2
ACTIVITY INDEX FILE
STR activity_indexes = "lungs_act"
ATTENUATION INDEX FILE
STR attenuation_indexes = "lungs_att"
ACTIVITY TABLE FILE
STR activity_table = "../../phg.data/phg_act_table"
ACTIVITY INDEX TO TABLE TRANSLATION FILE
STR activity_index_trans = "../../phg.data/phg_act_index_trans"
ATTENUATION TABLE FILE
STR attenuation_table = "../../phg.data/phg_att_table"
ATTENUATION INDEX TO TABLE TRANSLATION FILE
STR attenuation_index_trans = "../../phg.data/phg_att_index_trans"
PRODUCTIVITY TABLE FILE
STR productivity_output_table = ""
STR statistics_file = ""
BINNING PARAMATER FILE
STR bin_params_file = "binparam"

A.10 Configuration file example for the NCAT phantom

1 : activity_phantom_each_frame (1=save phantom to file, 0=don't save)
0 : attenuation_coeff_phantom_each_frame (1=save phantom to file, 0=don't save)
1 : activity_phantom_average (1=save , 0=don't save) see NOTE 0
0 : attenuation_coeff_phantom_average (1=save, 0=don't save) see NOTE 0
2 : motion_option (0=beating heart only, 1=respiratory motion only, 2=both motions) see NOTE 1

5 : output_period (SECS) (if ¡= 0, then output_period=time_per_frame*output_frames)

1 : time_per_frame (SECS) (**IGNORED unless output_period¡=0**)

32 : output_frames (# of output time frames)

1 : hrt_period (SECS) (length of beating heart cycle; normal = 1s) see NOTE 2 0.

0 : hrt_start_phase_index (range=0 to 1; ED=0, ES=0.4) see NOTE 2

5 : resp_period (SECS) (length of respiratory cycle; normal breathing = 5s) see NOTE 2 0.

0 : resp_start_phase_index (range=0 to 1, full exhale=0, full inhale=0.455) see NOTE 2 2.

0 : max_diaphragm_motion (extent in cm's of diaphragm motion; normal breathing = 2 cm) see NOTE 3

1.2 : max_AP_expansion (extent in cm's of the AP expansion of the chest; normal breathing = 1.2 cm) see NOTE 3

35.2 : body_long_axis (sets body transverse axis - scales everything except lungs and heart with it) (visible male = 35.2 cm)

23.3 : body_short_axis (sets body AP axis - scales everything except lungs, heart, and ribcage with it) (visible male = 23.3 cm)

41.7 : body_height (sets height of torso - scales everything except lungs, heart, and ribcage with it) (visible male = 41.7 cm)

22.0 : rib_long_axis (sets ribcage transverse axis - scales lungs with it and repositions the heart to adjust to the scaling) (visible male = 22.0 cm)

14.3 : rib_short_axis (sets ribcage AP axis - scales lungs with it and repositions the heart to adjust to the scaling) (visible male = 14.3 cm)

37.3 : rib_height (sets height of ribcage - scales lungs with it and repositions the heart to adjust to the scaling) (visible male = 37.3 cm)

1.0 : hrt_scale (scales heart in 3D - 1.0 is visible male) (Can use this to alter the heart or the following, but not both)

9.43 : hrt_lv_length (sets the length of the LV - entire heart is scaled with the LV) (NCAT heart = 9.43 cm)

2.97 : hrt_lv_radius (sets the ave. radius of the LV - entire heart is scaled with the radius) (NCAT heart = 2.97 cm)

1 : breast_type (0=supine, 1=prone)

0 : which_breast (0 = none, 1 = both, 2 = right only, 3=left only)

15.1 : breast_long_axis (sets the breasts lateral dimension) (PRONE normal = 15.1 cm, SUPINE normal = 18.2 cm)

7.0 : breast_short_axis (sets the breasts antero-posterior dimension) (PRONE normal = 7.0 cm, SUPINE = 4.0 cm)

14.0 : breast_height (sets the breasts height) (PRONE normal = 14.0 cm, SUPINE normal = 14.9 cm)

4.6 : theta angle of the breasts (angle the breasts are tilted transversely (sideways) from the center of the chest (PRONE normal = 4.6, SUPINE NORMAL = 40.0)

0.0 : phi angle of the breasts (angle the breasts are tilted up (+) or down (-) (PRONE normal = 0, SUPINE normal = -20.0)

3.4 : height of right_diaphragm/liver dome (visible human = 3.4 cm)

1.9 : height of left diaphragm dome (visible human = 1.9 cm)

0.1 : intv in cm (thickness of body tissue around the heart and liver)

0.3125 : pixel width (cm); see NOTE 5

128 : array size see NOTE 6

2 : subvoxel_index (=1,2,3,4 -¿ 1,8,27,64 subvoxels/voxel, respectively)

1 : start_slice; see NOTE 7 128 : end_slice; see NOTE 7

1 : increment between slices; see NOTE 7

-90 : zy_rotation (beta) in deg. ; see NOTE 8

-20. : xz_rotation (phi) in deg. ; see NOTE 8

-50. : yx_rotation (psi) in deg. ; see NOTE 8

0.0 : x translation in cm ; see NOTE 8

0.0 : y translation in cm ; see NOTE 8

0.0 : z translation in cm ; see NOTE 8

1 : apical_thinning (1 = present, otherwise not present) /*parameter is ignored*/

0.0 : valve thickness in cm (0= no valve); cannot be a negative value /*parameter is ignored*/

0.3 : av_step(cm): step width for smooth change between Atr & Ven (0=none) /*parameter is ignored*/

0 : total_rotation (deg); /*parameter is ignored*/

1 : activity units (1= scale by voxel volume; 0= don't scale) NOTE 9

50 : hrt_myoLV_act - activity in left ventricle myocardium

50 : hrt_myoRV_act - activity in right ventricle myocardium

50 : hrt_myoLA_act - activity in left atrium myocardium

50 : hrt_myoRA_act - activity in right atrium myocardium

50 : hrt_bldplLV_act - activity in left ventricle chamber (blood pool)

50 : hrt_bldplRV_act - activity in right ventricle chamber (blood pool)

50 : hrt_bldplLA_act - activity in left atria chamber (blood pool)

50 : hrt_bldplRA_act - activity in right atria chamber (blood pool)

50 : body_activity (background activity) ;

50 : liver_activity;

100 : lung_activity;

50 : st_wall_activity; (stomach wall)

50 : st_cnts_activity; (stomach contents)
50 : kidney_activity;
50 : spleen_activity;
50 : rib_activity;
0 : spine_activity;
140. : radionuclide energy in keV (range 1-1000 keV) ; for attn. map only

NOTE 0:

```
The average phantom is the average ONLY OF THOSE FRAMES GENERATED. That is,
if you specify that only 2 frames be generated, then the average phantom is
just the average of those 2 frames.
*****************************************************************************
** FOR A GOOD AVERAGE, generate at least 8-16 frames per 1 complete heart
** cycle and/or per 1 complete respiratory cycle.
*****************************************************************************
```

NOTE 1:

```
Heart motion refers to heart BEATING or contraction, while resp.
motion refers to organ motion due to breathing. Note that the entire heart is
translated or rotated due to resp. motion, even if it is not contracting.
** IF motion\_option=1 , THE HEART WILL MOVE (TRANSLATE) BUT NOT BEAT.****
see NOTE 1b.

If the motion\_option = 1 or 2, then the diaphragm
must be positioned as follows:
       1      : right\_diaphragm/liver position (raised)
       0      : left diaphragm position        (NOT raised)
```

NOTE 2:

```
Users sets the length and starting phase of both the heart
and respiratory cycles. NORMAL values for length of heart beat and
respiratory are cycles are 1 sec. and 5 secs., respectively,
BUT THESE CAN VARY AMONG PATIENTS and will increase if the patient
is under stress.

An index value between 0 and 1 is used the specify the starting phase
of the heart or resp cycles. IF NO MOTION IS SPECIFIED THEN THE STARTING
PHASE IS USED AS THE SINGLE PHASE AT WHICH THE PHANTOM IS GENERATED.
```

```
(see documentation for more details).
```

NOTE 3 :

```
These NORMAL values are for normal tidal breathing.
** Modeling a deep inhale may require higher values. **

The AP\_expansion parameter controls the anteroposterior diameter of the
ribcage, body,and lungs. The ribs rotate upward to expand the chest cavity
by the amount  indicated by the AP\_expansion parameter. The lungs and
body move with the expanding ribs. There is maximum amount by which the AP
diameter can expand, due to the size of the ribs (some expansions are
impossible geometrically). If the user specifies too great an expansion,
the program will terminate with an error message.

The diaphragm motion controls the motion of the liver, the left diaphragm,
the heart, stomach, and spleen. The liver is set to move forward during
inspiration an amount equal to the AP expansion of the chest as controlled
by the rib/body short axes. The liver moves back to its original position
during expiration. The liver is also set to move up/down with the diaphragm.
The heart moves with the liver. The stomach and spleen also move with the
liver but at a reduced extent.
```

NOTE 4:

```
(also see NOTE 1 if using resp. motion)
- if position is set to 1, then diaphragm/liver top protrudes into the
   lungs and is seen in the inferior cardiac slices. This protrusion
   into the lungs causes extra attenuation  of the counts coming
   from the inferior wall of the LV.
      i. When position 0 is chosen, the volume of the
         liver is less than if position 1 is chosen.
      ii. When position 1 is chosen ,the lung volume(s) is less
         than when position 0 is chosen
```

NOTE 5:

```
- Currently, only cubic voxels allowed, therefore,
  voxel\_volume = (voxel\_width)\^3
```

NOTE 6:

```
- The complete phantom array is 3 dimensional with each dimension=array\_size
- Typically, 60 cm x 60 cm is the largest camera field-of-view
  so the MCAT code has an internal check which prints out a warning
  in the *\_log file if (array\_size*pixel\_width) >= 60.0;
  therefore, to keep the FOV less than 60 cm :
        - if array\_size =128 --> pixel\_width <= 0.468
        - if array\_size = 64 --> pixel\_width <= 0.937
- make sure (array\_size)\^3 is smaller than or equal to the size of
  the array fphan() ( or fphana() ) as declared in the main program
```

NOTE 7:

```
- The complete phantom is a cubic, (array\_size)\^3 array; however,
  the whole phantom does not need to be saved. A portion of the
  phantom can be saved by specifying which slices to be saved.
```

NOTE 8:

```
- rotation parameters determine
  initial orientation of beating (dynamic) heart LV long axis
  see the subroutine CALC\_DYN\_HEART\_ROT\_MATRIX for details
- zy\_rotation : +y-axis rotates toward +z-axis (about x-axis) by beta
  xz\_rotation : +z-axis rotates toward +x-axis (about y-axis) by phi
  yx\_rotation : +x-axis rotates toward +y-axis (about z-axis) by psi

- Based on patient data, the mean and SD heart orientations are:
        zy\_rot = -110 degrees (no patient data for this rotation)
        xz\_rot = 23 +- 10 deg.
        yx\_rot = -52 +- 11 deg.
```

NOTE 9 :

```
if option 1 is chosen, the values of the activity specified in
this parameter file are scaled by the voxel volume
 FOR EXAMPLE:
  1) body\_activity = 1.0 and unit option equal 1
     => phantom will output the value 1.0*(pixel\_width)\^3 in body voxel
     OR
  2) body\_activity = 1.0 and unit option equal 0
     => phantom will output the value 1 in body voxels
```

A.11 Diagonalization of the covariance matrix when $n \ll p$

The PCA analysis described in section 6.5 involves the computation of the covariance matrix on the input data consisting of n observation vectors $\mathbf{x} = (x_1, \ldots, x_p)^t$. This produces a covariance matrix $\mathbf{C} \in \mathbb{R}^{p \times p}$. If p, the dimension of the observation vector $\mathbf{x}$, is too big in comparison to n (i.e. $n \ll p$), the computation of matrix $\mathbf{C}$ is intractable. This section describes a technique to compute a smaller covariance matrix $\mathbf{C} \in \mathbb{R}^{nxn}$ which retains the first $n-1$ principal components [23].

Commonly, the covariance matrix is computed by

$$\mathbf{C} = \frac{1}{n} \sum_{i=1}^{n} d\mathbf{x_i} d\mathbf{x_i}^t$$

with $d\mathbf{x_i} = \mathbf{x_i} - \overline{\mathbf{x}}$.

Which is equivalent to

$$\mathbf{C} = \frac{1}{n} \mathbf{D}\mathbf{D}^t. \tag{A.44}$$

with $\mathbf{D} = (d\mathbf{x_1}^t | \ldots | d\mathbf{x_n}^t)$.

Instead of computing $\mathbf{C}$ according to Eq. (A.44), a smaller matrix $\mathbf{T} \in \mathbb{R}^{nxn}$ is computed

$$T = \frac{1}{n} \mathbf{D}^t \mathbf{D} \tag{A.45}$$

Let's be now $(\mathbf{\Psi}, \gamma_\mathbf{i})_{i=1,\ldots,n}$ the pairs eigenvector-eigenvalue of $\mathbf{T}$. Then, it stands that

$$\mathbf{T}\mathbf{\Psi_i} = \gamma_\mathbf{i} \mathbf{\Psi_i} \tag{A.46}$$

and

$$\frac{1}{n} \mathbf{D}^t \mathbf{D} \mathbf{\Psi_i} = \gamma_\mathbf{i} \mathbf{\Psi_i}. \tag{A.47}$$

By multiplying $\mathbf{D}$ in Eq. (A.47), we obtain

$$\frac{1}{n}\mathbf{D}\mathbf{D}^t\mathbf{D}\mathbf{\Psi_i} = \mathbf{D}\gamma_\mathbf{i}\mathbf{\Psi_i} \tag{A.48}$$

$$\mathbf{C}\mathbf{D}\mathbf{\Psi_i} = \gamma_\mathbf{i}\mathbf{D}\mathbf{\Psi_i} \tag{A.49}$$

Therefore, $(\mathbf{D}\Psi_i, \gamma_i), i = 1, \ldots, n$ are the eigenvectors and eigenvalues of $\mathbf{C}$. After normalization, the eigenvectors and eigenvalues $(\mathbf{\Phi_i}, \lambda_i)_{i=1,\ldots,n}$ of $\mathbf{C}$ are

$$\mathbf{\Phi}_i = \frac{1}{\sqrt{\gamma_i n}}\mathbf{D}\Psi_i \tag{A.50}$$

$$\lambda_i = \gamma_i \tag{A.51}$$

Bibliography

[1] S.T. Acton and A. Restrepo. Locally monotonic models for image and video processing. In *Proc. IEEE Int. Conf. on Image Processing*, volume 2, pages 429–433, 1999.

[2] M.N. Ahmed, S.M. Yamany, N. Mohamed, A.A. Farag, and T. Moriarty. A modified fuzzy c-means algorithm for bias field estimation and segmentation of MRI data. *IEEE Transactions on Medical Imaging*, 21(3):193–199, 2002.

[3] S. Alenius. *On Noise Reduction in Iterative Image Reconstruction Algorithms for Emission Tomography: Median Root Prior*. PhD thesis, Tampere University of Technology, 1997.

[4] E. Atalar and L. Onural. A respiratory motion artifact reduction method in magnetic resonance imaging of the chest. *IEEE Transactions on Medical Imaging*, 10(1):11–24, 1991.

[5] S.L. Bacharach and I. Buvat. Attenuation correction in cardiac PET and SPECT. *Journal of Nuclear Cardiology*, 2:246–255, 1995.

[6] D.L. Bailey and A. Kalemis. Externally triggered gating of nuclear medicine acquisitions: a useful method for partitioning data. *Physics in Medicine and Biology*, 50(7):N55–N62, 2005.

[7] S.H. Benedict. Looking into patient positioning and organ motion. In *Annual meeting of the American College of Medical Physics*, 2001.

[8] R.I. Berbeco, H. Mostafavi, G.C. Sharp, and S.B. Jiang. Towards fluoroscopic respiratory gating for lung tumours without radiopaque markers. *Physics in Medicine and Biology*, 50:4481–4490, 2005.

[9] C. Blondel, R. Vaillant, G. Malandain, and N. Ayache. 3-D tomographic reconstruction of coronary arteries using a precomputed 4-D motion field. *Physics in Medicine and Biology*, 49(11):2197–2208, 2004.

[10] S. Bonnet, A. Koenig, S. Roux, P. Hugonnard, R. Guillemaud, and P. Grangeat. Dynamic x-ray computed tomography. *Proceedings of the IEEE*, 91(10):1574–1587, 2003.

[11] L. Boucher, S. Rodrigue, R. Lecompte, and F. Bénard. Respiratory garing for 3-dimensional PET of the thorax: feasibility and initial results. *Journal of Nuclear Medicine*, 45(2):214–219, February 2004.

[12] J.E. Bresenham. Algorithm for computer control of digital plotter. *IBM Systems Journal*, 4(1):25–30, January 1965.

[13] J. Brown and A. De Pierro. A row-action alternative to the EM algorithm for maximizing likelihoods in emission tomography. *IEEE Transactions on Medical Imaging*, 15:687–699, October 1996.

[14] I. Buvat, M. Rodriguez-Villafuerte, A. Todd-Pokropek, H. Benali, and R. Di Paola. Comparative assessment of nine scatter correction methods based on spectral analysis using monte carlo simulations. *Journal of Nuclear Medicine*, 36:1476–1488, 1995.

[15] P. Cachier, E. Bardinet, D. Dormont, X. Pennec, and N. Ayache. Iconic Feature Based Nonrigid Registration: The PASHA Algorithm. *Computer Vision and Image Understanding*, 89(2-3):272–298, Feb.-march 2003.

[16] O. Camara, O. Colliot, and I. Bloch. Computational Modeling of Thoracic and Abdominal Anatomy Using Spatial Relationships for Image Segmentation. *Real Time Imaging*, pages 263–273, 2004.

[17] O. Camara, G. Delso, and I. Bloch. Evaluation of a thoracic elastic registration method using anatomical constraints in oncology. In *2nd. Joint Conference of the IEEE Engineering in Medicine and Biology Society*, 2002.

[18] O. Camara, G. Delso, O. Colliot, I. Bloch, V. Frouin, T. Delzescaux, P. Briandet, J. F. Stévenet, C. Bernard, H. Foehrenbach, X. Marchandise, and P. Rigo. Software-Based Non-Linear Registration and Evaluation of 18F-FDG Whole-Body Emission PET with Thoracic and Abdominal CT. Alternative or Complementary Solution to Combined PET/CT Scanners. In *EANM'04 European Journal of Nuclear Medicine and Molecular Imaging*, volume 32, page S236, Helsinki, Finland, 2004.

[19] L.T. Chang. A method for attenuation correction in radionuclide computed tomography. *IEEE Transactions on Nuclear Science*, 25:638–643, 1978.

[20] P. Charbonnier, L. Blanc-Feraud, G. Aubert, and M. Barlaud. Deterministic edge-preserving regularization in computed imaging. *IEEE Transactions on Image Processing*, 6(2):298–311, February 1997.

[21] I.J. Chetty, M. Rosu, D.L. McShan, B.A. Fraass, J.M. Balter, and R.K. Ten Haken. Accounting for center-of-mass target motion

using convolution methods in monte carlo-based dose calculations of the lung. *Medical physics*, 31(4):925–32, April 2004.

[22] K.J. Coakley. A cross-validation procedure for stopping the EM algorithm and deconvolution of neutron depth profiling spectra. *IEEE Transactions on Nuclear Science*, 38(1):9–15, February 1991.

[23] T. Cootes, C. Taylor, D. Cooper, and J. Graham. Active shape models - their training and application. *Computer Vision and Image Understanding*, 61(1):38–59, January 1995.

[24] C.R. Crawford, K.F. King, C.J. Ritchie, and J.D. Godwin. Respiratory compensation in projection imaging using a magnification and displacement model. *IEEE Transactions on Medical Imaging*, 15(3):327–332, June 1996.

[25] J. Darcourt. *Classification des méthodes de reconstruction tomographique à partir de projections*. PhD thesis, Université de Nice Sophia Antipolis, 1992.

[26] L. Dietrich, T. Tücking, S. Nill, and U. Oelfke. Compensation for respiratory motion by gated radiotherapy: an experimental study. *Physics in Medicine and Biology*, 50(10):2405–2414, 2005.

[27] J.A. Fessler and A.O. Hero. Space-alternating generalized expectation-maximization algorithm. *IEEE Transactions on Signal Processing*, 42(10):2664–77, Oct. 1994.

[28] J.A. Fessler, E.P. Picaro, N.H. Clinthorne, and K. Lange. Grouped-coordinate ascent algorithms for penalized-likelihood transmission image reconstruction. *IEEE Transactions on Medical Imaging*, 16:166–175, April 1997.

[29] I.K. Fodor. A survey of dimension reduction techniques. Technical Repport UCRL-ID-148494, Lawrence Livermore National Laboratory, 2002.

[30] J.O. Fredrickson, H. Wegmuller, R.J. Herfkens, and N.J. Pelc. Simultaneous temporal resolution of cardiac and respiratory motion in MR imaging. *Radiology*, 195(1), 1995.

[31] R.R. Fulton, S.R. Meikle, S. Eberl, J. Pfeiffer, C.J. Constable, and M.J. Fulham. Correction for head movements in positron emission tomography using an optical motion-tracking system. *IEEE Transactions on Nuclear Science*, 49(1):116–123, 2002.

[32] R.R. Fulton, I. Nickel, L. Tellmann, S.R. Meikle, U.K. Pietrzyk, and H. Herzog. Event-by-event motion compensation in 3d pet. In *Conference Records IEEE Nuc. Sci. Symp. Med. Imag. Conf.*, pages 3286–3289, 2003.

[33] A. Geist, A. Beguelin, J.J. Dongarra, W. Jiang, R. Manchek, and V.S. Sunderam. PVM 3 user's guide and reference manual. Technical Report ORNL/TM-12187, Oak Ridge National Laboratory, 1993.

[34] S.J. Glick, B.C. Penney, M.A. King, and C.L. Byrne. Noniterative compensation for the distance-dependent detector response and photon attenuation in SPECT imaging. *IEEE Transactions on Medical Imaging*, 13:363–374, June 1994.

[35] H.C. Glifford, M.A. King, R.G. Wells, W.G. Hawkins, M.V. Narayanan, and P.H. Pretorius. LROC analysis of detector-response compensation in SPECT. *IEEE Transactions on Medical Imaging*, 19(5):463–473, May 2000.

[36] G.W. Goerres, E. Kamel, T.-N.H. Heidelberg, M.R. Schwitter, C. Burger, and G.K. von Schulthess. PET-CT image coregistration in the thorax: Influence of respiration. *European Journal of Nuclear Medicine*, 29:351–360, 2002.

[37] G.W. Goerres, E. Kamel, B. Seifert, C. Burger, A. Buck, T.F. Hany, and G.K. von Schulthess. Accuracy of image coregistra-

tion of pulmonary lesions in patients with non-small cell lung cancer using an integrated PET/CT system. *Journal of Nuclear Medicine*, 43(11):1469–75, 2002.

[38] M. A. González Ballester, M.G. Linguraru, M. Reyes Aguirre, and N. Ayache. On the adequacy of principal factor analysis for the study of shape variability. In J.M. Fitzpatrick and J.M. Reinhardt, editors, *SPIE Medical Imaging '05*, volume 5747, pages 1392–1399. SPIE Publishing, 2005.

[39] P. Grangeat, A. Koenig, T. Rodet, and S. Bonnet. Theoretical framework for a dynamic cone-beam reconstruction algorithm based on a dynamic particle model. *Physics in Medicine and Biology*, 47(15):261–262, 2002.

[40] P.J. Green. Bayesian reconstruction from emission tomogrpahy data using a modified EM algorithm. *IEEE Transactions on Medical Imaging*, 9:84–93, March 1990.

[41] Parallel computing at INRIA sophia-antipolis: a cluster computing approach. http://www-sop.inria.fr/parallel/.

[42] A. Guimond, J. Meunier, and J.-P. Thirion. Average brain models: A convergence study. Technical Report 3731, INRIA, Sophia-Antipolis, France, July 1999.

[43] A. Guimond, J. Meunier, and J.-P. Thirion. Average brain models: A convergence study. *Computer Vision and Image Understanding*, 77(2):192–210, 2000.

[44] R.L. Harrison, S.D. Vannoy, D.R. Haynor, S.B. Gillispie, M.S. Kaplan, and T.K. Lewellen. Preliminary experience with the photon history generator module of a public-domain simulation system for emission tomography. *Conf. Rec. IEEE Nucl. Sci. Symp.*, pages 1154–1158, 1993.

[45] W.G. Hawkins and P.K. Leichner. An instrinsic 3D weiner filter for the deconvolution of spatially varying collimator blur. In *Proc. First IEEE Int. Conf. Image Processing*, volume 2, pages 163–168, 1994.

[46] T. Hebert and R. Leahy. A generalized EM algorithm for 3-D bayesian reconstruction from poisson data using gibbs priors. *IEEE Transactions on Medical Imaging*, 8(2):194–202, June 1989.

[47] G.T. Herman. *Image reconstruction from projections: the fundamentals of computerized tomography.* Academic Press, 1980.

[48] G.T. Herman and B.L. Meyer. Algebraic reconstruction techniques can be made computationally efficient. *IEEE Transactions on Medical Imaging*, 12:600–609, 1993.

[49] G.T. Herman and D. Odhner. Performance evaluation of an iterative image reconstruction algorithm for positron emission tomography. *IEEE Transactions on Medical Imaging*, 10(3):336–346, September 1991.

[50] I.T Hsiao, A. Rangarajan, P. Khurd, and G. Gindi. An accelerated convergent ordered subsets algorithm for emission tomography. *Physics in Medicine and Biology*, 49(7):2145–2156, June 2004.

[51] J. Hu, S.T. Haworth, R.C. Molthen, and C.A. Dawson. Post-acquisition small-animal respiratory gated imaging using micro cone-beam CT. In Amir A. Amini and Armando Manduca, editors, *Medical Imaging 2004: Physiology, Function, and Structure from Medical Images*, volume 5369, pages 350–360. SPIE, 2004.

[52] H.M. Hudson and R.S. Larkin. Accelerated image reconstruction using ordered subsets of projection data. *IEEE Transactions on Medical Imaging*, 13(4):601–609, 1994.

[53] S. Iamratanakul, J. McNames, and B. Goldstein. Estimation respiration from physiologic pressure signals. In *IEEE Proceeding of EMBS 2003 conference*, 2003.

[54] J.R. Jaszczak, L.K. Greer, E.C. Floyd, C.C. Harris, and R.E. Coleman. Improved SPECT quantification using compensation for scattered photons. *Journal of Nuclear Medicine*, 25:893–900, 1984.

[55] A. Jemal, T. Murray, A. Samuels, A. Ghafoor, E. Ward, and M. J. Thun. Cancer statistics, 2003. *CA Cancer J. Clin.*, (53):5–26, 2003.

[56] V.E. Johnson. A note on stopping rules in EM-ML reconstructions of ECT images. *IEEE Transactions on Medical Imaging*, 13(3):569–571, Sept. 1994.

[57] L. Kaufman. Implementing and accelerating the EM algorithm for positron emission tomography. *IEEE Transactions on Medical Imaging*, 6:37–51, March 1987.

[58] P.J. Keall, J.V. Siebers, S. Joshi, and R. Mohan. Monte carlo as a four-dimensional radiotherapy treatment-planning tool to account for respiratory motion. *Physics in Medicine and Biology*, 49(16):3639–3648, 2004. Paper presented at World Congress on Medical Physics and Biomedical Engineering (Sydney)—WC2003.

[59] G.J. Klein, B.W. Reutter, E.H. Botvinick, T.F. Budinger, and R.H. Huesman. Fine-scale motion detection using intrinsic list mode PET information. In *MMBIA01*, pages 71–78, 2001.

[60] G.J. Klein, B.W. Reutter, M.H. Ho, J.H. Reed, and R.H. Huesman. Real-time system for respiratory-cardiac gating in positron tomography. *IEEE Transactions on Nuclear Science*, 45:2139–43, 1998.

[61] H. Knutsson, M. Andersson, M. Borga, and L. Wigström. Respiratory Artifact Reduction in MRI using Dynamic Deformation Modelling. In *Proceedings of the SSAB Symposium on Image Analysis*, March 2002.

[62] V. Kohli, M.A. King, S.J. Glick, and T-S Pan. Comparison of frequency-distance relationship and gaussian-diffusion-based methods of compensation for distance-dependent spatial resolution in SPECT imaging. *Physics in Medicine and Biology*, 43:1025–1037, 1998.

[63] G. Kontaxakis. *Maximum likelihood image reconstruction for positron emission tomography: Convergence characteristics and stopping rules*. PhD thesis, Rutgers University, 1996. 240 p.

[64] G. Kontaxakis and G. Tzanakos. Study of the convergence properties of the EM algorithm - a new stopping rule. *IEEE Nucl. Sci. Symp. and Med. Imag. Conf.*, 2:1163–1165, November 1992. Orlando, FL, USA.

[65] G. Kontaxakis and G. Tzanakos. Practical application of a new stopping criterion for the EM-MLE image reconstruction for PET. *Proceedings of the 18th IEEE-EMBS Annual International Conference*, 2:848–849, November 1996.

[66] P.M. Koulibaly. *Régularisation et corrections physiques en tomographie d'émission*. PhD thesis, Université de Nice Sophia Antipolis, Oct 1996.

[67] F. Lamare, T. Cresson, J. Savean, C. Cheze Le Rest, A. Turzo, A.J. Reader, and D. Visvikis. Affine transformation of list mode data for respiratory motion correction in PET. In *IEEE TNS and MIC conference records*, 2004.

[68] K. Lange, M. Bahn, and R. Little. A theoretical study of some maximum likelihood algorithms for emission and transmission

tomography. *IEEE Transactions on Medical Imaging*, 6(2):106–114, June 1987.

[69] K. Lange and J.A. Fessler. Globally convergent algorithms for maximum a posteriori transmission tomography. *IEEE Transactions on Image Processing*, 4:1430–8, Oct. 1995.

[70] K.M. Langen and D.T. Jones. Organ motion and its management. *International Journal of Radiation Oncology, Biology, Physics*, 50:265–78, 2001.

[71] R. Leahy and C. Byrne. Recent developments in iterative image reconstruction for PET and SPECT. *IEEE Transactions on Medical Imaging*, 19:257–260, April 2000.

[72] E. Levitan and G. Herman. A maximum a posteriori probability expectation maximization algorithm for image reconstruction in emission tomography. *IEEE Transactions on Medical Imaging*, 6(3):185–192, Sept 1987.

[73] R. Levkovitz, D. Falikman, M. Zibulevsky, A. Ben-Tal, and A. Nemirovski. The design and implementation of COSEM, an iterative algorithm for fully 3-D listmode data. *IEEE Transactions on Medical Imaging*, 20(7):633–42, July 2001.

[74] J.M. Links. Quantitative imaging: neuroreceptors, neurotransmitters, and enzymes. In Wagner HN Frost JJ, editor, *Physics and instrumentation of positron emission tomography*, pages 37–50. New York: Raven Press, 1990.

[75] V.J. Lowe, J.W. Fletcher, and L. Gobar et al. Prospective investigation of positron emission tomography in lung nodules. *Journal of Clinical Oncology*, 16:1075–1084, 1998.

[76] W. Lu and T.R. Mackie. Tomographic motion detection and correction directly in sinogram space. *Physics in Medicine and Biology*, 47(8):1267–84, April 2002.

[77] A.E. Lujan, E.W. Larsen, J.M. Balter, and R.K. Ten Haken. A method for incorporating organ motion due to breathing into 3D dose calculations. *Medical physics*, 26(5):715–20, May 1999.

[78] A. Manduca, K.P. McGee, E.B. Welch, J.P. Felmlee, R.C. Grimm, and R.L. Ehman. Autocorrection in MR imaging: adaptive motion correction without navigator echoes. *Radiology*, 215(3):904–9, 2000.

[79] D. Mattes, D.R. Haynor, H. Vesselle, T.K. Lewellen, and W. Eubank. PET-CT image registration in the chest using free-form deformations. *IEEE Transactions on Medical Imaging*, 22(1):120–128, 2003.

[80] B. Movassaghi, V. Rasche, M. Viergever, W. Niessen, and R. Florent. 3D coronary reconstruction from calibrated motion-compensated 2D projections. In Elsevier, editor, *Proceedings of Computer Assisted Radiology and Surgery (CARS) 2003*, volume 1256 of *International Congress Series*, pages 1079–1084, 2003.

[81] E. Mumcuoglu, R. Leahy, S. Cherry, and Z. Zhou. Fast gradient-based methods for bayesian reconstruction of transmission and emission PET images. *IEEE Transactions on Medical Imaging*, 13(4):687–701, December 1994.

[82] P. Munger, G.R. Crelier, T.M. Peters, and G.B. Pike. An inverse approach to the correction of distortion in EPI images. *IEEE Transactions on Medical Imaging*, 19(7):681–689, July 2000.

[83] S.A. Nehmeh, Y.E. Erdi, C.C. Ling, K.E. Rosenzweig, H. Schroder, S.M. Larson, H.A. Macapinlac, O.D. Squire, and J.L. Humm. Effect of respiratory gating on quantifying PET images of lung cancer. *Journal of Nuclear Medicine*, 43(7):876–81, 2002.

[84] S.A. Nehmeh, Y.E. Erdi, K.E. Rosenzweig, H. Schroder, S.M. Larson, O.D. Squire, and J.L. Humm. Reduction of respiratory motion artifacts in PET imaging of lung cancer by respiratory correlated dynamic PET: Methodology and comparison with respiratory gated PET. *Journal of Nuclear Medicine*, 44(10):1644–1648, 2003.

[85] S. Nill, J. Unkelbach, L. Dietrich, and U. Oelfke. Online correction for respiratory motion: evaluation of two different imaging geometries. *Physics in Medicine and Biology*, 50(17):4087–4096, 2005.

[86] J.M. Ollinger. Model-based scatter correction for fully 3D PET. *Physics in Medicine and Biology*, 41:153–176, 1996.

[87] M.M. Osman, C. Cohade, Y. Nakamoto, L.T. Marshall, J.P. Leal, and R.L. Wahl. Clinically significant inaccurate localization of lesions with PET/CT: frequency in 300 patients. *Journal of Nuclear Medicine*, 4(2):240–243, 2003.

[88] M.M. Osman, C. Cohade, Y. Nakamoto, and R.L. Wahl. Respiratory motion artifacts on PET emission images obtained using CT attenuation correction on PET-CT. *Journal of Nuclear Medicine*, 30(4):603–6, 2003.

[89] C. Pellot-Barakat, M. Ivanovic, A. Herment, K. Erlandsson, and D.K. Shelton. Detection of motion in hybrid PET/SPECT imaging based on the correlation of partial sinograms. *IEEE Transactions on Medical Imaging*, 20(10):1072–1083, Oct. 2001.

[90] Y. Picard and C.J. Thompson. Motion correction of PET images using multiple acquisition frames. *IEEE Transactions on Medical Imaging*, 16(2):137–44, April 1997.

[91] A.R. De Pierro. A modified expectation maximization algorithm for penalized likelihood estimation in emission tomography. *IEEE Transactions on Medical Imaging*, 14(1):132–137, March 1995.

[92] P.H. Pretorius, M.A. King, S.J. Glick, T-S Pan, and D-S Luo. Reducing the effect of non-stationary resolution on activity quantitation with the frequency distance relationship in SPECT. *IEEE Transactions on Nuclear Science*, 43:3335–41, 1996.

[93] J. Qi and R.M. Leahy. Resolution ans noise properties of MAP reconstruction for fully 3D PET. In *Proc. of the 1999 Intl. Mtg. on Fully 3D Im. Recon. in Rad. Nuc. Med.*, volume 18, pages 35–9, 1999.

[94] V. Rasche, M. Grass, R. Koppe, A. Bücker, R. Günther, H. Kühl, J. Op de Beek, R. Bertrams, and R. Suurmond. ECG-gated 3D rotational coronary angiography. In Springer-Verlag., editor, *Proceedings of Computer Assisted Radiology and Surgery (CARS) 2002*, pages 826–831, 2002.

[95] A.J. Reader, S. Ally, F. Bakatselos, R. Manavaki, R.J. Walledge, A.P. Jeavons, P.J. Julyan, S. Zhao, D.L. Hastings, and J. Zweit. One-pass list-mode EM algorithm for high resolution 3D PET image reconstruction into large arrays. *IEEE Transactions on Nuclear Science*, 49:693–699, 2002.

[96] D. Rey. *Détection et quantification de processus évolutifs dans des images médicales tridimensionnelles : application à la sclérose en plaques*. Thèse de sciences, Université de Nice Sophia-Antipolis, October 2002.

[97] A. Rhamim and P. Bloomfield. Motion correction in histogram-mode and listmode EM reconstructions. In *IEEE MIC*, 2003.

[98] S. Roux, L. Desbat, A. Koenig, and P. Grangeat. Efficient acquisition protocol for cardiac dynamic CT. In *IEEE Nuclear Science Symposium Conference Record*, volume 3, pages 1612–1616, 2002.

[99] K. Sauer and C. Bouman. Bayesian estimation of transmission tomograms using segmentation based optimization. *IEEE Transactions on Nuclear Science*, 39(4):1144–1152, August 1992.

[100] K. Sauer and C. Bouman. A local update strategy for iterative reconstruction from projections. *IEEE Transactions on Signal Processing*, 41:534–548, February 1993.

[101] W.P. Segars. *Development of a new dynamic NURBS-based cardiac-torso (NCAT) phantom*. PhD thesis, The University of North Carolina, 2001.

[102] Y. Seppenwoolde, H. Shirato, K. Kitamura, S. Shimizu, M. van Herk, J.V. Lebesque, and K. Miyasaka. Precise and real-time measurement of 3D tumor motion in lung due to breathing and heartbeat, measured during radiotherapy. *International Journal of Radiation Oncology, Biology, Physics*, 53(4):822–34, July 2002.

[103] T.T. Shannon, J. McNames, M.S. Ellenby, and B. Goldstein. Modeling respiration from blood pressure waveform signals: An independent component approach. In *Proceedings of the Second Joint EMBS/BMES Conference 2002*, pages 200–201, Houston, TX, October 2002.

[104] L. Shepp and Y. Vardi. Maximum likelihood reconstruction for emission tomography. *IEEE Transactions on Medical Imaging*, 1(2):113–122, 1982.

[105] R.L. Siddon. Fast calculation of the exact radiological path for a three-dimensional CT array. *Medical physics*, 12:252–255, 1985.

[106] A. Sigfridsson, J-P Escobar Kvitting, L. Wigstrom, M. Andersson, and H. Knutsson. Retrospective respiratory motion compensation for cardiac MRI. In *Proceedings of ESMRMB*, Rotterdam, Netherlands, September 2003.

[107] L. Simon, P. Giraud, V. Servois, and J.C. Rosenwald. Lung volume assessment for a cross-comparison of two breathing-adapted techniques in radiotherapy. *International Journal of Radiation Oncology, Biology, Physics*, 2005. To be published.

[108] M. Soret. *Correction de l'effet de volume partiel en tomographie d'émission*. PhD thesis, Université Paris XI Faculté de Médecine Paris-Sud, Oct 2005.

[109] J.W. Stayman and J.A. Fessler. Regularization for uniform spatial resolution properties in penalized-likelihood image reconstruction. *IEEE Transactions on Medical Imaging*, 18:293–305, April 1998.

[110] T.A. Sundaram and J.C. Gee. Towards a model of lung biomechanics: pulmonary kinematics via registration of serial lung images. *Medical Image Analysis*, 9(6):524–37, December 2005.

[111] Y.C. Tai, K.P. Lin, C.K. Ho, S.C.H. Huang, and E.J. Hoffman. Utilization of 3D elastic transformation in the registration of chest X-ray CT and whole-body PET. *IEEE Transactions on Nuclear Science*, 44:1606–1612, 1997.

[112] E. Tanaka and H. Kudo. Subset-dependent relaxation in block-iterative algorithms for image reconstruction in emission tomography. *pmb*, 48(10):1405–1422, 2003.

[113] L. Tellman, R.R. Fulton, K. Bente, I. Stangier, O. Winz, U. Just, H. Herzog, and U.K. Pietryk. Motion correction of head movements in PET: realisation for routine usage. In *Nuclear Science Symposium Conference Record*, volume 5, pages 3105–3107, 2003.

[114] K. Thielemans, S. Mustafovic, and L. Schnorr. Image reconstruction of motion corrected sinograms. In *IEEE Medical Imaging Conf.*, 2003.

[115] C.J. Thompson. The problem of scatter correction in positron volume imaging. *IEEE Transactions on Medical Imaging*, 12(1):124, 132 1993.

[116] A.N. Tikhonov and V.A. Arsenin. *Solutions of Ill-posed Problems*. Winston & Sons, 1976.

[117] Division of Nuclear Medicine University of Washington. SimSET homepage. http://depts.washington.edu/∼ simset/html/simset_main.html.

[118] Mehmet Üzümcü, A.F. Frangi, M. Sonka, J.H.C. Reiber, and B.P.F. Lelieveldt. ICA vs. PCA active appearance models: Application to cardiac MR segmentation. In Randy E. Ellis and Terry M. Peters, editors, *Medical image computing and computer-assisted intervention (MICCAI 2003)*, volume 2878 of *LNCS*, pages 451–458, Montreal, Canada, November 2003. Springer Verlag.

[119] J.J. Bourdin V. Boyer. A faster algorithm for 3D discrete lines. *Eurographics*, 1998.

[120] S.S. Vedam, V.R. Kini, P.J. Keall, V. Ramakrishnan, H. Mostafavi, and R. Mohan. Quantifying the predictability of diaphragm motion during respiration with a noninvasive external marker. *Medical physics*, 30(4):505–13, Apr 2003.

[121] D. Visvikis, O. Barret, T.D. Fryer, F. Lamare, A. Turzo, Y. Bizais, and C. Cheze Le Rest. Evaluation of respiratory motion effects in comparison with other parameters affecting PET image quality. In *IEEE TNS and MIC conference records*, 2004.

[122] D. Visvikis, O. Barret, T.D. Fryer, A. Turzo, F. Lamare, C. C. Cheze-Le Rest, and Y. Bizais. A posteriori respiratory motion gating of dynamic pet images. In *IEEE Medical Imaging Conference proceedings*, 2003.

[123] L. Weruaga, J. Morales, L. Núñez, and R. Verdú. Estimating volumetric motion in human thorax with parametric matching constraints. *IEEE Transactions on Medical Imaging*, 22(6):766–772, June 2003.

[124] J.W.H. Wolthaus, M. van Herk, S.H. Muller, J.S.A. Belderbos, J.V. Lebesque, J.A. de Bois, M.M.G. Rossi, and E.M.F. Damen. Fusion of respiration-correlated PET and CT scans: correlated lung tumour motion in anatomical and functional scans. *Physics in Medicine and Biology*, 50(7):1569–1583, 2005.

[125] H. Wu, G.C. Sharp, B. Salzberg, D. Kaeli, H. Shirato, and S.B. Jiang. A finite state model for respiratory motion analysis in image guided radiation therapy. *Physics in Medicine and Biology*, 49(23):5357–5372, 2004.

[126] J.N. Yu, F.H. Fahey, B.A. Harkness, H.D. Gage, C.G. Eades, and J.W. Keyes Jr. Evaluation of emission-transmission registration in thoracic PET. *Journal of Nuclear Medicine*, 34(11):1777–1780, Nov. 1994.

[127] H. Zaidi. Statistical reconstrucion-based scatter correction: a new method for 3D PET. In *Proc. of the 22nd Annual International Conference of the IEEE*, pages 86–89, 2000.